CONTROLLED SOLIDIFICATION OF DILUTE BINARY IRON-NICKEL ALLOYS

CONTROLLED SOLIDIFICATION OF DILUTE BINARY IRON-NICKEL ALLOYS

BY

Iljoon Jin, B.Sc.

A Thesis

Submitted to the Faculty of Graduate Studies

in Partial Fulfilment of the Requirements

for the Degree

Doctor of Philosophy

McMaster University

November 1972

TO THE MEMORY OF MY FATHER

DOCTOR OF PHILOSOPHY (1972) McMaster University
(Metallurgy and Materials Science) Hamilton, Ontario

TITLE: Controlled Solidification of Dilute Binary Iron-Nickel Alloys

AUTHOR: Iljoon Jin, B.Sc. (Seoul National University)

SUPERVISOR: Professor G. R. Purdy

NUMBER OF PAGES: xii, 123

SCOPE AND CONTENTS:

This thesis is concerned with establishing an improved theoretical and experimental description of the steady state controlled solidification of dilute binary alloys. In the present theory, a mathematical model is developed to describe an experimental situation in which alloy solidification is controlled by solute diffusion in the liquid phase. The theory gives a unique solution of the solute diffusion equation and predicts the variation of the thermodynamic properties at the solid-liquid interface, particularly at the dendrite tip, as a function of material constants and growth parameters. An experimental program was developed to investigate the dependence on the growth parameters of the morphological development of the interface and the concentration variations at the interface of an Fe-8 wt. % Ni alloy. Experimental results for this particular system can be successfully rationalized by the approximate solution of the present theory.

ACKNOWLEDGEMENTS

I am deeply grateful to my supervisor Professor G. R. Purdy for his continuous encouragement and guidance throughout the course of this work. I would also like to thank Professors J. S. Kirkaldy and J. A. Morrison for their extensive assistance through the supervisory committee, and Dr. M. R. Hone for his friendship and assistance during the initial difficult period of this research program. My gratitude extends to many other members of the Department of Metallurgy and Materials Science for their stimulating discussions and assistance.

Financial assistance of the Department of Metallurgy and Materials Science, the Province of Ontario (each in the form of graduate fellowships), and of the American Iron and Steel Institute (in the form of a research grant to Professor G. R. Purdy) is gratefully acknowledged.

TABLE OF CONTENTS

LIST OF TABLES*

* Tables have been placed at the end of the thesis.

LIST OF ILLUSTRATIONS*

*Illustrations have been placed at the end of the thesis.

LIST OF SYMBOLS*

Symbol	Definition
A	area
$(a)_r$	Pochhammer's symbol, $\Gamma(a+r)/\Gamma(a)$
c	solute concentration
c_∞	initial solute concentration of the liquid
c_{tip}, c^s_{tip}	solute concentration at the dendrite tip in liquid and in solid respectively
D, D_s	solute diffusion coefficient in liquid and in solid respectively
d	density
E_n	series coefficient
$E_1(x)$	exponential integral
$\mathrm{erfc}(x)$	complementary error function
G	imposed temperature gradient
G^o_e	equilibrium liquidus temperature gradient at the tip
$I_m\mathrm{erfc}(x)$	integral error function
J_i	flux of component i
$J_n(x)$	Bessel function of order n
K	geometrical factor (usually curvature)
k^o	equilibrium distribution coefficient
L	latent heat of fusion
L_{ik}	phenomenological coefficient
$L_n(x)$	Laguerre polynomial

* This list contains only those symbols which are used repeatedly in the thesis.

Symbol	Definition
M	molar mass
$M(a,b,x)$	confluent hypergeometric function of the first kind.
m	slope of liquidus
P	mass Peclet number
R	gas constant
r,b	cylindrical coordinates
$\mathcal{J}$	an index for the amount of constitutional supercooling
T	temperature
T_o	temperature of the dendrite tip
T_M	equilibrium melting temperature of pure material
ΔT_s, ΔT_c, ΔT_k	undercooling due to solute, curvature and interface attachment kinetics respectively
t	time
$U(a,b,x)$	confluent hypergeometric function of the second kind
u	solute concentration, $c - c_\infty$
V	volume
v	growth velocity
v_{crit}	critical growth velocity for planar-nonplanar interface transition
v_n	growth velocity normal to the interface
X_i	thermodynamic force of component i
x,y,z	moving cartesian coordinates
x_L	boundary limit of a paraboloidal dendrite
α,β,φ	moving parabolic coordinates
$\Gamma(x)$	gamma function

Symbol	Definition
γ	interfacial energy
γ_i^k	activity coefficient of component i in phase k
κ	thermal conductivity
λ	dendrite spacing
μ_o	linear coefficient of the interface attachment kinetics
μ_i^k	chemical potential of component i in phase k
ρ	radius of tip curvature
σ	rate of internal entropy production due to diffusion fields per unit volume
$\psi(x)$	psi function

CHAPTER 1

INTRODUCTION

The solidification of molten metals is one of the most important processes in the production of metals; and one which is often considered to mark the boundary between extractive metallurgy and physical metallurgy. Solidification processes may be classified as single phase solidification and poly-phase solidification according to the number of phases being produced, and as controlled solidification and unconstrained solidification according to the conditions externally imposed.

The present work is mainly concerned with the single phase controlled solidification of dilute binary alloys. This process has been studied for a long period with the objects of improving the structure and properties of castings and of broadening our scientific understanding of nature. Although recent quantitative studies have clarified many problems of the process (e.g. the marginal instability of a planar interface, microsegregation attending dendritic growth, etc.) many important problems remain still unsolved or only partially solved. One of these is the dependence of the dendrite tip properties on growth parameters.

The purpose of the present study is to provide a

more concrete analysis, theoretically and experimentally, of the steady state single phase controlled solidification, with the ultimate view of predicting the cell or dendrite tip concentration and curvature as a function of materials constants and the fixed and controllable growth parameters.

The thesis can be conveniently divided into four parts: In the first part, a number of previous studies of the single phase solidification are reviewed. The second part is the formulation and analysis of the diffusion controlled steady state binary alloy solidification as a boundary value problem. Our treatment falls short of the ultimate achievement by requiring some semi-empirical input, a requirement that is typical of complex free boundary problems which have one or more internal degrees of freedom. An approximate solution to this problem is offered through a shape assumption, the general principles of irreversible thermodynamics and an empirical rule for the dendrite spacing vs. growth velocity. The third part describes the experimental study of some iron base alloys, using the technique of controlled unidirectional solidification. Specific contributions are the observations of the effects of temperature gradient and growth velocity, each as a separate variable, on the growth morphology and micro-segregation, and of the profound effect of crystal structure on the homogenization kinetics of the micro-segregation. In the final part, a quantitative discussion on the present theory and experimental results

is presented. It is found that the present experimental results are in reasonable agreement with the values predicted by the present theory.

It is expected that the results of the present theoretical and experimental investigations will provide a clearer understanding of the fundamental aspects of alloy solidification processes and contribute directly to the casting industry as a necessary starting point for an improved microsegregation theory applicable to directional solidification.

CHAPTER 2

PREVIOUS WORK

In this chapter, some representative previous work on single phase solidification will be briefly reviewed.

2.1 Controlled Solidification

With the term "controlled solidification", we define a solidification process in which a positive temperature gradient and a growth velocity are externally imposed as growth conditions. Under these conditions, the liquid-solid interface of a pure metallic melt is always planar. For a binary alloy melt, the interface may be planar, cellular or cellular dendritic depending on the materials constants and growth conditions.

All the early theoretical work on morphology concerns itself with the margin between a planar and non-planar interface, i.e. with "marginal instability". The first quantitative analysis of this problem was established by Tiller et al[1]. The redistribution of solute ahead of a planar interface during transient and steady state solidification was calculated, and from this, the condition for the onset of constitutional supercooling ahead of a planar interface was obtained as

$$\frac{G}{v} < \frac{-mc_\infty(1-k_o)}{D\,k_o} \qquad (1)$$

where G is the temperature gradient in the liquid, v is the growth velocity, m is the liquidus slope, k_o is the equilibrium distribution coefficient, c_∞ is the initial bulk concentration and D is the diffusion coefficient of solute in the liquid. For a decade, this condition was considered the sole criterion for the instability of a moving planar interface and was shown to be in fairly good agreement with most experiments. It should be noted that some other physical problems associated with the liquid-solid interface, for instance the capillarity effect (associated with non-planar interfaces), the kinetic undercooling at a moving interface, thermal conductivities of both phases, etc., have not been accounted for in the criterion.

Mullins and Sekerka applied linear perturbation theory to this problem in their already classic work on the morphological stability of a spherical interface[2] and a planar interface[3]. Of particular importance of the work is the fact that the capillarity effect has been included and its stabilizing effect quantified. A number of extensions and applications of the theory followed:

Tarshis and Tiller[4] reexamined morphological stability by considering the effect of molecular attachment kinetics. They found a significant stabilizing effect of slow kinetics.

Shewmon[5] has applied stability theory to solid-solid transformations and shown that low interfacial mobility and transformation stresses stabilize the interface, whereas

impurities enhance the instability.

Cahn[6] has investigated the effect of slightly anisotropic surface tension and interface kinetics of a growing particle, and found that the anisotropic surface tension does not result in a stable particle at any size and the interface kinetics stabilizes the particle until it reaches a size which marks the transition from interface kinetics control to diffusion control.

An extension of the stability theory to dilute ternary alloy solidification has been established by Coates and Purdy[7]. It was demonstrated that multicomponent diffusional interaction may enhance stability or instability depending on the shape of liquidus surface and the sign of thermodynamic interaction parameters, whereas in binary alloy the solute gradient always promotes instability.

Sekerka's recent paper "Morphological stability"[8] may be the best review of linear perturbation theory, with a full account of stabilizing and destabilizing factors.

The main fruits of linear theory are the determination of marginal stability and the determination of the range of the wavelength of growing initial perturbations. If the spatial pattern of the growing perturbation is to be predicted, if the effect of large perturbation is to be estimated, or if the time dependent evolution of the shape of a growing initial perturbation is to be estimated, then nonlinear terms must be taken into account. A nonlinear stability analysis has been established by Wollkind and Segel[9]. They determined an instability criterion as a function of wavelength and amplitude of initial perturbations.

for a given experimental condition, while linear theory predicts an instability criterion as a function of wavelength only.

A quantitative study on the non-planar interface morphology and the solute redistribution in the liquid has been attempted by Bolling and Tiller[10]. This work has shown the free boundary character of the system, and from this limitation several approximate models have been developed[11,12] to predict some features of the solute segregation in terms of growth conditions and materials constants. These models are based on rather restrictive assumptions about interface geometry.

Experimental studies of controlled solidification have been conducted by many investigators. Chalmers and his coworkers have initiated the first quantitative experimental and theoretical studies of this problem, separating the growth velocity and the temperature gradient. Most of their work is elegantly summarized in Chalmer's book "Principles of Solidification"[13].

Through a series of experimental studies of ferrous and nonferrous alloys, Flemings and his coworkers[14-17] have attempted to describe the solute redistribution during directional dendritic solidification using a simplified model which is based on local equilibrium at the interface, negligible undercooling of the dendrite tips, mass conservation, complete mixing in the liquid and partial diffusional homogenization in the solid. Although this model does not yield detailed

insight into the physics of a solidification process, it constitutes a good basis for engineering practise.

Various aspects of the unidirectional solidification of ferrous and nonferrous alloys, as well as their mechanical properties have been investigated by Weinberg et al[18,19]. It has been demonstrated that experimentally determined solute distributions across dendrites are in good agreement with calculated profiles based on complete mixing in the liquid or diffusional transport of solute in the liquid, depending on the system chosen.

Sharp and Hellawell[20,21] investigated the solute distributions ahead of non-planar interfaces which are developed under well defined growth velocities and temperature gradients. They found the undercooling associated with interface curvature is very small for the conventional range of steady state solidification experiments of metallic system.

Direct observation of growth morphology during the solidification of molten metals is unfortunately difficult due to the fact that metals are opaque. To avoid this difficulty, many indirect observation techniques have been developed. Of special interest is the decanting technique employed by Chalmers et al[13]. Jackson et al[22,23] have used some transparent organic compounds which have small entropies of melting and solidify like metals.

2.2 Unconstrained Solidification

The solidification which occurs in an initially uniformly supercooled melt is defined in the present work as unconstrained solidification. Under this condition, the temperature gradient at the interface is everywhere negative. Thus the heat sink is the melt itself and the resulting dendrites may grow in any direction.

The first successful mathematical treatment of this system was due to Ivantsov[24]. He solved the heat balance equation at the interface which simultaneously satisfies the thermal diffusion equation in the liquid, leading to the following very important conclusion: The surface of a linearly growing needle-like crystal is not isothermal if it is other than a paraboloid of revolution. Horvay and Cahn[25] extended Ivantsov's analysis to more generalized shapes. The limitation of this theory was the unattainability of a unique solution of the diffusion equation. Thus the separate determination of growth velocity and tip radius was impossible.

Temkin[26] and, independently, Bolling and Tiller[27], have incorporated the nonisothermal character of a moving non-planar interface due to curvature (Gibbs-Thomson effect) and kinetic effects. Introducing this nonisothermal character of the interface and the condition of maximum growth velocity (which had been initially proposed by Zener[28]), the one internal degree of freedom in Ivantsov's solution has been eliminated, i.e. a unique growth velocity and corresponding radius of tip curvature for a given undercooling have been obtained. In his mathematical operation, Temkin

simplified the problem to the Laplace equation in moving parabolic coordinates using the fact that the Peclet number is small compared with unity.

Kotler and Tarshis[29] have refined Temkin's analysis restoring one of the neglected terms in Temkin's analysis. A mathematically complete solution has been recently obtained by Holzmann[30] and Trivedi[31]. The solution obtained is complete from a mathematical point of view. However, the problem was formulated on the basis of the shape remaining paraboloidal, which is no longer true as soon as we take the nonisothermal character into account.

Hillig[32] has reexamined the steady state growth shape using a self-consistent method. His analysis did not usually lead to a unique shape, which may imply the absence of a true steady state solution.

The experimentally observed dendrite shape of pure tin has been shown to be approximately parabolic[33]. The growth velocity as a function of melt undercooling has been experimentally observed for pure tin[34], white phosphorous[35], and others. These results are reported to be in reasonable agreement with theoretical predictions, although there appear some discrepancies in the magnitudes of some physical parameters of the materials used[31].

The solidification of the central equiaxed region of metal castings may be one practical example of unconstrained solidification. Among a number of experiments on this system, the works of Bäckerud and Chalmers[36], and Doherty and Feest[37]

are of special interest. By thermal analysis experiments, they have estimated the temperature of the growing dendrite tips. This temperature is much lower than the equilibrium liquidus temperature of the initial bulk concentration. From this result, they have concluded that there exists a significant solute build-up ahead of the dendrite tips. This conclusion indicates that the microsegregation model[14-19] which assumes the tip concentration to be $k_o C_o$, should be considered as a first approximation only.

CHAPTER 3

THEORY

It is noted in the previous chapter that among a number of works on single phase solidification, few research programs are concerned with the theoretical description of the non-planar interface morphology and associated solute redistribution which occur under most experimental conditions of single phase controlled solidification. In this chapter, a mathematical analysis is given in order to explain more fully the physical and thermodynamic properties of the solidification system with a moving non-planar interface, particularly around the tip.

3.1 Statement of the Problem

Consider a dilute binary alloy rod partially melted in a furnace which has a positive temperature gradient (Fig. 1). The two phases, solid and liquid, are assumed to be separated by a continuous boundary, the interface. When the furnace is moving up with a constant velocity towards the direction of the positive temperature gradient, the interface will move up constantly except for the initial transient period so that the liquid solidifies with a constant rate, that is, a first order phase transformation, liquid-solid is in progress under steady state. The question

is: What happens at the interface and what will be the resulting structure? Although much has been spoken to the question by previous investigators (the marginal stability of a planar interface, solute field ahead of a planar interface, empirical theory of microsegregation, etc.), many important problems, particularly when the interface is non-planar, remain only partially solved. Among these are the curvature and concentration of the tip of a non-planar interface. We shall undertake a theoretical description of this problem.

By the thermodynamic definition of the first order phase transition in a multicomponent system, the molar Gibbs function is continuous but its derivatives with respect to temperature and pressure are discontinuous at the interface[38]. Thus a solidification process involves the rearrangement of atoms, the change of composition, enthalpy and volume at the interface. Furthermore a real solidification process is an irreversible process as long as some external constraints are maintained, because it is impossible to traverse a locus of constant entropy in the thermodynamic configuration space. Therefore, a complete description of a solidification process must involve the kinetics of atomic rearrangement, the transport of mass and heat, mass convection by volume change and other principles which control the irreversible process.

To describe the given experimental situation, we consider a model with the following assumptions:

(i) The temperature gradient at the interface is held

constant by coupling the solidification system to a large thermal reservoir. This assumption can be considered to be reasonable from the fact that $\frac{D}{D_{th}} << 1$, where D is the solute diffusion coefficient in the liquid and D_{th} is the thermal diffusivity in the liquid.

(ii) The convectional mass transport is negligible. This condition can be approximately met through an appropriate geometrical arrangement of the system.

(iii) Diffusion in the solid is negligible. This condition will be reexamined after we obtain the solution.

(iv) Solute concentration in the liquid is small.

(v) The extent of the liquid phase is infinite.

(vi) The effect of interface attachment kinetics is negligible.

Under these assumptions, the system can be considered to be mass diffusion controlled in the liquid. Thus the field equation is the mass diffusion equation and a complete analysis of the system must be determined by the complete solution of the diffusion equation which must also satisfy all the imposed boundary conditions. A difficulty in the present problem arises from our lack of knowledge concerning the shape and location of the boundary itself, which must be found as a part of the solution. We have

thus to deal with what is commonly referred to as a "free boundary problem",[39,40] which simply means a problem whose solution is defined over a domain that is not given in advance. This problem is far too difficult to treat in a satisfactory way, unless the boundary conditions are very simple (for example, one dimensional melting of semi-infinite solid with constant body and surface temperatures—the Stefan problem[40]).

In our boundary value problem, one of the boundary conditions, the mass conservation condition at the interface, is non-linear and this is a very complex boundary condition for an arbitrary interface shape. To make the problem mathematically tractable, we introduce a partially free shape (if the shape is not free at all, the problem becomes trivial), a paraboloid of revolution whose tip curvature, position, and boundary limit (hypothetical spacing) are free. This shape assumption is taken due solely to the mathematical simplicity and the fact that experimentally observed shape is very close to a paraboloid of revolution near the tip.

For the mathematical simplicity, we deal with a single dendrite. This implies that the interaction of mass diffusion fields by an array of true dendrites is ignored. This effect can be quite appreciable far behind the tip; however, it is assumed that the interaction does not affect the tip properties.

It should be noted that our model involves three undetermined parameters, the radius of tip curvature, ρ, the position of the interface or the tip concentration, c_{tip}, and the boundary limit, x_L (Fig. 2). Thus at least three extra conditions are necessary to obtain a unique solution of the field equation. One of the conditions is clearly the extra physical boundary condition at the interface, the mass conservation condition at the interface. The second condition is the postulated thermodynamic variational principle, a stochastic component which is always present in nature. The third condition needed to determine the boundary limit obtains from a self-consistent method based on our empirical knowledge of dendrite spacings.

Based on our model, we now wish to attack the problem with the following algorithm:

(i) describe the mass diffusion equation and boundary conditions in moving parabolic coordinates.

(ii) obtain the solution of the diffusion equation to the free boundary conditions

(iii) apply the mass conservation condition

(iv) apply the postulated thermodynamic variational principle and the empirical rule for the spacing to determine the boundary limit and free parameters, which leads to a unique solution of the diffusion equation.

Two specific contributions are given in the present work:

(i) Ivantsov obtained the solution of the thermal

diffusion equation to the isothermal interface boundary conditions for the paraboloidal shape, and Temkin, Trivedi, and Holzmann presented the solution of the diffusion equation to the non-isothermal interface boundary conditions due to curvature and kinetic effects. We give the solution of the diffusion equation, under the same assumption of shape preservation, to the non-isothermal interface boundary conditions due to curvature and kinetic effects and the imposed temperature gradient.

(ii) In previous work, the internal degree of freedom was eliminated by optimizing a particular thermodynamic or physical parameter on a particular point of the interface. We employ the postulated thermodynamic function and we consider the entire volume of the system.

3.2 Diffusion Equation

From the phase diagram of a dilute binary alloy, the equilibrium distribution coefficient, k_o, is defined as

$$k_o = \frac{c_S}{c_L} , \qquad (2)$$

where c_S and c_L are the equilibrium solute concentrations of solid and liquid at the planar interface, respectively. When $k_o > 1$, solvent rejection is expected for the solidification to proceed, whereas solute rejection is expected when $k_o < 1$.

The present theory deals with the case $k_o < 1$, and utilizes the assumption that k_o is a constant. k_o is not necessarily a constant for a given system, however it is often nearly constant over a wide range of dilute composition.

The redistribution of solute in the liquid phase must obey the diffusion equation in our convectionless experimental system. In the fixed cartesian coordinates (X,Y,Z), the diffusion equation is

$$\frac{\partial c}{\partial t}(X,Y,Z,t) = D\nabla^2 c(X,Y,Z,t), \qquad (3)$$

where c is the solute concentration, t is the time and D is the solute diffusion coefficient in the liquid.

For the uniformly moving cartesian coordinates (x,y,z) with a constant velocity v whose motion is in the positive z direction, Eq.(3) has the time independent form

$$\nabla^2 c(x,y,z) + \frac{v}{D}\frac{\partial c}{\partial z}(x,y,z) = 0 . \qquad (4)$$

In place of c, we introduce a new variable

$$u(x,y,z) = c(x,y,z) - c_\infty . \qquad (5)$$

Then the diffusion equation (4) has the form

$$\nabla^2 u(x,y,z) + \frac{v}{D}\frac{\partial u}{\partial z}(x,y,z) = 0 . \qquad (6)$$

To make the problem more readily soluble for the given boundary constraints, we introduce the uniformly moving parabolic coordinates (α,β,φ) which are related to the moving cartesian coordinates by (Fig. 3)

$$\left.\begin{aligned} x &= \rho\,\alpha\,\beta\cos\varphi \\ y &= \rho\,\alpha\,\beta\sin\varphi \\ z &= \tfrac{1}{2}\rho(\alpha^2-\beta^2) \end{aligned}\right\}, \qquad (7)$$

where ρ is the radius of tip curvature of the paraboloid $\alpha = 1$, α and β are dimensionless parabolic coordinates and φ is the azimuthal angle. By the coordinate transformation to the parabolic coordinates, the diffusion equation (6) has the form (see Appendix I)

$$\frac{1}{\alpha^2+\beta^2}\left[\frac{\partial^2 u}{\partial\alpha^2}(\alpha,\beta,\varphi) + \left(\frac{1}{\alpha}+\frac{v\rho}{D}\alpha\right)\frac{\partial u}{\partial\alpha}(\alpha,\beta,\varphi) + \frac{\partial^2 u}{\partial\beta^2}(\alpha,\beta,\varphi)\right.$$

$$\left.+\left(\frac{1}{\beta}-\frac{v\rho}{D}\beta\right)\frac{\partial u}{\partial\beta}(\alpha,\beta,\varphi)\right] + \frac{1}{\alpha^2\beta^2}\,\frac{\partial^2 u}{\partial\varphi^2}(\alpha,\beta,\varphi) = 0. \qquad (8)$$

With rotational symmetry, we finally obtain

$$\frac{\partial^2 u}{\partial\alpha^2}(\alpha,\beta) + \left(\frac{1}{\alpha}+2p\alpha\right)\frac{\partial u}{\partial\alpha}(\alpha,\beta) + \frac{\partial^2 u}{\partial\beta^2}(\alpha,\beta) + \left(\frac{1}{\beta}-2p\beta\right)\frac{\partial u}{\partial\beta}(\alpha,\beta) = 0, \qquad (9)$$

where p is defined by

$$p = \frac{v\rho}{2D}. \qquad (10)$$

p is a dimensionless parameter and generally called the mass Peclet number.

3.3 Boundary Conditions

(i) Interface Temperature and Concentration

There are three additive effects which contribute to the depression of the actual interface temperature below

the equilibrium melting temperature of a pure solvent[12].

The temperature depression due to solute, ΔT_s, is given by

$$\Delta T_s = -mc(1,\beta), \tag{11}$$

where $c(1,\beta)$ is the solute concentration at the interface of liquid side.

The temperature depression due to the interfacial energy (the Gibbs-Thomson effect), ΔT_c, is

$$\Delta T_c = T_M \frac{\gamma}{L} K, \tag{12}$$

where T_M is the melting temperature of a pure solvent for a planar interface, L is the latent heat of melting, γ is the interfacial energy and K is a geometrical factor defined by

$$K = \frac{dA}{dV} \tag{13}$$

where A is the interfacial area and V is the volume enclosed by A. For a monotonically curved interface, K is equivalent to the mean curvature of the interface.

It is further known that interface attachment kinetics give an additional temperature depression as solidification is in progress. The relationship between the kinetic undercooling, ΔT_k, and the growth velocity normal to the interface, v_n, follows the particular kinetic law that is pertinent. Three distinct types are known[13]: For an atomically rough interface,

$$v_n = \Delta T_k. \tag{14}$$

For the growth on a screw dislocation,

$$v_n \propto (\Delta T_k)^2. \tag{15}$$

For the growth by the two dimensional nucleation mechanism

$$v_n \propto e^{-\frac{a}{\Delta T_k}}, \tag{16}$$

where a is a constant.

Metals with small entropies of melting usually have a rough interface and may follow the linear relation. Linear growth kinetics can be represented by

$$\Delta T_k = \frac{v_n}{\mu_o}, \tag{17}$$

where μ_o is the linear kinetic coefficient.

Putting all our information together, the interface temperature $T(1,\beta)$ can be expressed as

$$T(1,\beta) = T_M - (\Delta T_s + \Delta T_c + \Delta T_k)$$

$$= T_M + mc(1,\beta) - \frac{T_M \gamma}{L} K - \frac{v_n}{\mu_o}. \tag{18}$$

From Eq. (18)

$$c(1,\beta) = \frac{1}{m}\left[T(1,\beta) - T_M + \frac{T_M \gamma}{L} K + \frac{v_n}{\mu_o}\right]. \tag{19}$$

From the imposed constant temperature gradient

$$T(1,\beta) = T_o - \tfrac{1}{2} G\rho\beta^2, \tag{20}$$

where $T_o = T(1,0)$, the undetermined tip temperature. The normal velocity and mean curvature for the surface of a paraboloid of revolution are given respectively by[41]

$$v_n = \frac{v}{(1+\beta^2)^{\frac{1}{2}}} \tag{21}$$

and

$$K = \frac{1}{\rho} \frac{(2+\beta^2)}{(1+\beta^2)^{3/2}} \quad (22)$$

From Eqs. (5), (18), (19), (20), (21) and (22), it follows that

$$u(1,\beta) = (c_{tip} - \frac{2T_M\gamma}{m\rho L} - \frac{v}{m\mu_o} - c_\infty) - \frac{GD}{mv} p\beta^2 + \frac{T_M\gamma}{m\rho L} p^{3/2}(p + p\beta^2)^{-3/2} + \frac{1}{m}(\frac{T_M\gamma}{\rho L} + \frac{v}{\mu_c}) p^{1/2}(p + p\beta^2)^{-1/2}, \quad (23)$$

where $c_{tip} = c(1,0)$, the undetermined solute concentration at the tip. The formal boundary condition, Eq. (23), becomes inappropriate when $c(1,\beta) \geq 1$. It is considered, however, that the system remains dilute to a sufficiently large value of β that the physical boundary condition around the dendrite tip is adequately represented.

(ii) Boundary Condition at Infinity

When $\alpha \to \infty$, $u(\alpha,\beta) \to 0$ (24)

This boundary condition ignores the interaction between neighbouring dendrites and this is the reason that this model does not predict any aspects of the problem of cooperative phenomena. However, as stated in the previous section, we assume that it can yield a reasonable description of the dendrite tip properties.

(iii) Mass Balance at the Tip

The condition of mass conservation at the tip gives

$$-D \left.\frac{\partial c}{\partial z}\right|_{\substack{x=y=0 \\ z=\frac{1}{2}\rho}} = c_{tip}(1-k_o)v \quad (25)$$

or expressing this in the parabolic coordinates (see Appendix I)

$$D \left.\frac{\partial c}{\partial \alpha}\right|_{\substack{\alpha=1 \\ \beta=0}} = c_{tip}(k_o-1)v\rho. \tag{26}$$

3.4 Solution of the Diffusion Equation

By the method of separation of variables, we obtain the general solution of Eq.(9) (see Appendix II)

$$u(\alpha,\beta) = \sum_{n=o}^{\infty} E_n \frac{e^{-p\alpha^2} U(n+1,1,p\alpha^2)}{e^{-P}\, U(n+1,1,p)} L_n(p\beta^2), \tag{27}$$

where E_n are the arbitrary coefficients, $L_n(x)$ are the Laguerre polynomials[42,46] defined by

$$L_n(x) = \frac{(-1)^n}{n!}\left[x^n - \frac{n^2}{1!}x^{n-1} + \frac{n^2(n-1)^2}{2!}x^{n-2} \cdots\cdots (-1)^n n!\right] \tag{28}$$

(integral n)

and $U(a,b,z)$ is the confluent hypergeometric function of the second kind[43]. For $b = 1$, it has the logarithmic solution of the form

$$U(a,1,z) = \frac{-1}{\Gamma(a)}\left[M(a,1,z)\ln z + \sum_{r=0}^{\infty} \frac{(a)_r z^r}{(r!)^2}\{\psi(a+r) - 2\psi(1+r)\}\right], \tag{29}$$

where $\Gamma(x)$ is the Gamma function[44], $M(a,1,z)$ is the confluent hypergeometric function of the first kind[43] which has the general form

$$M(a,b,z) = 1 + \frac{a}{b}z + \frac{(a)_2}{(b)_2 2!}z^2 + \cdots + \frac{(a)_n}{(b)_n n!}z^n + \cdots, \tag{30}$$

where $(a)_0 = 1$

$$(a)_n = a(a+1)(a+2)\cdots(a+n-1) \tag{31}$$

and $\psi(x)$ is the psi function[44,46] defined by

$$\psi(x) = \frac{\Gamma'(x)}{\Gamma(x)}. \tag{32}$$

In the expression, Eq.(27), we have taken account of the boundary condition at $\alpha = \infty$.

3.5 Calculation of the Series Coefficients E_n

The arbitrary coefficients of the series, E_n, have to be evaluated such that they satisfy the interface boundary condition.

Putting $\alpha = 1$ in Eq. (27),

$$u(1,\beta) = \sum_{n=0}^{\infty} E_n L_n(p\beta^2). \tag{33}$$

Eq.(33) has the form of the eigenfunction expansion of a real function. If we assume the series converges, then the coefficients can be evaluated from the orthogonality of the Laguerre polynomials with an appropriate weight function[45]. Multiplying $e^{-p\beta^2} L_n(p\beta^2)$ in both sides of Eq.(33) and integrating term by term over the infinite interval (o,∞), we obtain

$$E_n = \int_o^{\infty} e^{-p\beta^2} u(1,\beta) L_n(p\beta^2) d(p\beta^2). \tag{34}$$

From Eqs.(23) and (34), it follows that

$$E_n = (c_{tip} - \frac{2T_M\gamma}{m\rho L} - \frac{v}{m\mu_o} - c_\infty) \int_o^{\infty} e^{-\xi} L_n(\xi) d\xi$$

$$- \frac{GD}{mv} \int_0^\infty \xi\, e^{-\xi} L_n(\xi)\, d\xi$$

$$+ \frac{T_M \gamma}{m\rho L}\, p^{3/2} \int_0^\infty (p+\xi)^{-3/2} e^{-\xi} L_n(\xi)\, d\xi$$

$$+ \frac{1}{m}\left(\frac{T_M \gamma}{\rho L} + \frac{v}{\mu_o}\right) p^{1/2} \int_0^\infty (p+\xi)^{-1/2} e^{-\xi} L_n(\xi)\, d\xi \qquad (35)$$

where $\xi = p\beta^2$. Evaluating all four integrals (see Appendix III), we obtain

$$E_n = \left(c_{tip} - \frac{2T_M \gamma}{m\rho L} - \frac{v}{m\mu_o} - c_\infty\right) \frac{(-1)^n}{\Gamma(n+1)\,\Gamma(-n+1)} - \frac{GD}{mv} \frac{(-1)^n}{\Gamma(n+1)\,\Gamma(-n+2)}$$

$$+ \frac{2T_M \gamma}{m\rho L}\, p e^p\, I_{2n+1}\mathrm{erfc}(\sqrt{p})$$

$$+ \frac{1}{m}\left(\frac{T_M \gamma}{\rho L} + \frac{v}{\mu_o}\right) p^{1/2} e^p\, \frac{\Gamma(n+1/2)}{\Gamma(n+1)}\, I_{2n}\mathrm{erfc}(\sqrt{p}), \qquad (36)$$

where $I_m\mathrm{erfc}(x)$ is the normalized integral error function[46,47] defined by

$$I_m\mathrm{erfc}(x) = 2^m \Gamma\left(1+\frac{m}{2}\right) \frac{2}{\sqrt{\pi}} \int_x^\infty \frac{(t-x)^m}{m!}\, e^{-t^2}\, dt \qquad (37)$$

Eq.(27) with the coefficients given by Eq.(36) describes the complete diffusion field for solute in the liquid. However this expression explicitly involves two undetermined parameters, c_{tip} and ρ, which have been introduced in the steady state shape and the corresponding boundary conditions. To determine these free parameters, some extra conditions must be introduced. In the present analysis, we shall consider all of the elemental physical and thermo-

dynamic constraints believed to control the given solidification process. One of them is clearly the mass conservation condition (physical constraint). For the other one, the maximum interface temperature condition has been used in a number of prior treatments[10,12,27] without critical justification. This latter will be more closely examined in the later section.

Special Cases

Before going into further analysis of the problem, we examine our solution for some special cases.

(i) Isothermal Interface

Under this condition, the temperature gradient and the Gibbs-Thomson and kinetic effects are zero. Putting $G = 0$, $\gamma = 0$ and $\mu_o = \infty$ in Eq.(36), and using the recurrence relations of the confluent hypergeometric function of the second kind[43], we obtain the solute diffusion field in the liquid as

$$u(\alpha) = (c_{tip} - c_\infty) \frac{E_1(p\alpha^2)}{E_1(p)} , \qquad (38)$$

where $E_1(x)$ is the exponential integral[46]. This special form is the same as that found by Ivantsov[24].

(ii) Non-isothermal Interface due to the Gibbs-Thomson and Kinetic Effects

Putting $G = 0$ in Eq.(36), we obtain

$$u(\alpha,\beta) = (c_{tip} - \frac{2T_M\gamma}{mpL} - \frac{v}{m\mu_o} - c_\infty) \frac{E_1(p\alpha^2)}{E_1(p)}$$

$$+ \sum_{n=o}^{\infty} \left[\frac{2T_M\gamma}{m\rho L} pe^p I_{2n+1}\text{erfc}(\sqrt{p}) + \frac{1}{m}\left(\frac{T_M\gamma}{\rho L} + \frac{v}{\mu_o}\right) p^{\frac{1}{2}} \right.$$

$$\left. e^p \frac{\Gamma(n+\frac{1}{2})}{\Gamma(n+1)} I_{2n}\text{erfc}(\sqrt{p}) \right] \frac{e^{-p\alpha^2} U(n+1,1,p\alpha^2)}{e^{-p} U(n+1,1,p)} L_n(p\beta^2). \quad (39)$$

This is identical to the Trivedi's solution[31] with the replacement of concentration parameters in place of temperature parameters.

(iii) Planar Interface

This condition implies that $p \to \infty$ for all finite growth velocities. When $p \to \infty$, the ratio of the confluent hypergeometric functions becomes unity via the asymptotic expansions of $U(a,1,x)$[43]. For large x,

$$\frac{U(a,1,p\alpha^2)}{U(a,1,p)} \simeq \frac{(p\alpha^2)^{-a}}{p^{-a}} = \alpha^{-2a} \simeq 1 \quad (40)$$

and the ratio of the exponential functions is

$$\frac{e^{-p\alpha^2}}{e^{-p}} = e^{p(1-\alpha^2)} \simeq e^{-\frac{v}{D}z'}, \quad (41)$$

where z' is the new coordinate which has origin at the interface

$$z' = z - \tfrac{1}{2}\rho. \quad (42)$$

Substituting Eqs.(40) and (41) into Eq.(27) and putting $\gamma = 0$ and $\mu_o = \infty$ in Eq.(36), we obtain

$$u(z') = (c_{tip} - c_\infty) e^{-\frac{v}{D}z'}. \quad (43)$$

This special form is the same as the solution of the steady state diffusion equation for a planar interface[1].

3.6 Physical Constraint; Mass Conservation at the Tip

From the mass balance boundary condition at the tip, Eq.(26), and the solution of the diffusion equation Eq.(27), we now seek the explicit form for the tip concentration.

From the identity[43]

$$\frac{d^n}{dx^n}\left[e^{-x}U(a,b,x)\right] = (-1)^n e^{-x}U(a,b-n,x), \qquad (44)$$

the partial derivative of u with respect to α is obtained as

$$\frac{\partial u}{\partial \alpha} = \sum_{n=0}^{\infty} (E_n)\ (-2p\alpha)\ \frac{e^{-p\alpha^2}U(n+1,2,p\alpha^2)}{e^{-p}U(n+1,1,p)}\ L_n(p\beta^2). \qquad (45)$$

At the tip, it has the form

$$\left.\frac{\partial u}{\partial \alpha}\right|_{\substack{\alpha=1\\ \beta=0}} = (c_{tip} - \frac{2T_M\gamma}{m\rho L} - \frac{v}{m\mu_o} - c_\infty)\ \frac{U(1,2,p)}{U(1,1,p)} - \frac{GD}{mv}\left[\frac{U(1,2,p)}{U(1,1,p)} - \frac{U(2,2,p)}{U(2,1,p)}\right]$$

$$+ \sum_{n=0}^{\infty} (E_n')\ \frac{U(n+1,2,p)}{U(n+1,1,p)}, \qquad (46)$$

where

$$E_n' = \frac{2T_M\gamma}{m\rho L}\ pe^p\ I_{2n+1}\ \mathrm{erfc}(\sqrt{p})$$

$$+ \frac{1}{m}\left(\frac{T_M\gamma}{\rho L} + \frac{v}{\mu_o}\right)p^{\frac{1}{2}}\ e^p\ \frac{\Gamma(n+\frac{1}{2})}{\Gamma(n+1)}\ I_{2n}\mathrm{erfc}(\sqrt{p}). \qquad (47)$$

From Eq.(26) and (46), we obtain the explicit form for the tip concentration

$$c_{tip} = \left[(c_\infty + \frac{2T_M\gamma}{m\rho L} + \frac{v}{m\mu_o})\ \frac{U(1,2,p)}{U(1,1,p)} + \frac{GD}{mv}\left\{\frac{U(1,2,p)}{U(1,1,p)} - \frac{U(2,2,p)}{U(2,1,p)}\right\}\right.$$

$$- \sum_{n=o}^{\infty} (E_n') \frac{U(n+1,2,p)}{U(n+1,1,p)} \Bigg] \Bigg/ \left[(k_o - 1) + \frac{U(1,2,p)}{U(1,1,p)} \right] . \qquad (48)$$

Using the recurrence relations of the confluent hypergeometric functions of the second kind[43,46], Eq.(48) can be expressed in the following form

$$c_{tip} = \left[(c_\infty + \frac{2T_M\gamma}{m\rho L} + \frac{v}{m\mu_o}) \frac{1}{pe^{p}E_1(p)} + \frac{GD}{mv} \left\{ \frac{1}{pe^{p}E_1(p)} - \frac{p^{-1} - e^{p}E_1(p)}{e^{p}E_1(p)(1+p) - 1} \right\} \right.$$

$$\left. - \sum_{n\neq 0}^{\infty} (E_n') \frac{U(n+1,2,p)}{U(n+1,1,p)} \right] \Bigg/ \left[(k_o - 1) + \frac{1}{pe^{p}E_1(p)} \right] . \qquad (49)$$

The corresponding tip temperature is

$$T_o = T_M + mc_{tip} - \frac{2T_M\gamma}{\rho L} - \frac{v}{\mu_o} . \qquad (50)$$

The equilibrium liquidus temperature gradient in front of the tip, G_e^o, may be expressed as

$$G_e^o = m\left(\frac{\partial c}{\partial z}\right)_{\substack{x=y=0 \\ z=\frac{1}{2}\rho}} = m \frac{1}{\rho} \left(\frac{\partial u}{\partial \alpha}\right)_{\substack{\alpha=1 \\ \beta=0}} \qquad (51)$$

From Eqs.(46) and (51),

$$G_e^o = - \frac{mv}{D} \left[(c_{tip} - \frac{2T_M\gamma}{m\rho L} - \frac{v}{m\mu_o} - c_\infty) \frac{U(1,2,p)}{U(1,1,p)} \right.$$

$$\left. - \frac{GD}{mv} \left\{ \frac{U(1,2,p)}{U(1,1,p)} - \frac{U(2,2,p)}{U(2,1,p)} \right\} + \sum_{n=0}^{\infty} (E_n') \frac{U(n+1,2,p)}{U(n+1,1,p)} \right] , \qquad (52)$$

or

$$G_e^o = - \frac{mv}{D} \left[(c_{tip} - \frac{2T_M\gamma}{m\rho L} - \frac{v}{m\mu_o} - c_\infty) \frac{1}{pe^{p}E_1(p)} - \frac{GD}{mv} \left\{ \frac{1}{pe^{p}E_1(p)} \right. \right.$$

$$\left. \left. - \frac{p^{-1} - e^{p}E_1(p)}{e^{p}E_1(p)(1+p) - 1} \right\} + \sum_{n=0}^{\infty} (E_n') \frac{U(n+1,2,p)}{U(n+1,1,p)} \right] . \qquad (53)$$

Neglecting the Gibbs-Thomson and kinetic effects, we have the simpler form

$$c_{tip} = \frac{c_\infty \dfrac{1}{pe^{pE_1(p)}} + \dfrac{GD}{mv}\left(\dfrac{1}{pe^{pE_1(p)}} - \dfrac{p^{-1}-e^{pE_1(p)}}{e^{pE_1(p)}(1+p)-1}\right)}{k_o - 1 + \dfrac{1}{pe^{pE_1(p)}}}, \tag{54}$$

$$G_e^o = -\frac{mv}{D}\left[c_\infty \frac{1}{pe^{pE_1(p)}} - \frac{GD}{mv}\left(\frac{1}{pe^{pE_1(p)}} - \frac{p^{-1}-e^{pE_1(p)}}{e^{pE_1(p)}(1+p)-1}\right)\right] \tag{55}$$

and

$$T_o = T_M + m\, c_{tip}. \tag{56}$$

Special Cases

(i) The Case $p \to \infty$ (planar interface)

Using the asymptotic expansions in x ($x \to \infty$) for $U(a,b,x)$[43] and $I_m\mathrm{erfc}(x)$[46], we directly obtain

$$c_{tip} \to \frac{c_\infty}{k_o} \tag{57}$$

and

$$G_e^o \to \frac{-c_\infty mv(1-k_o)}{k_o D}. \tag{58}$$

The special solutions, Eqs. (57) and (58), are the same as those obtained by planar interface analysis[1].

(ii) The Case $p \to 0$ (infinitely sharp dendrite)

Neglecting the Gibbs-Thomson and kinetic effect and using the asymptotic expansions in $x (x \to 0)$ for $U(a,b,x)$,

$$c_{tip} \to c_\infty \tag{59}$$

and

$$G_e^o \rightarrow \frac{-c_\infty mv(1-k_o)}{D} . \qquad (60)$$

Eqs.(59) and (60) show the tip concentration and the equilibrium liquidus temperature gradient at the tip of an infinitely sharp dendrite under the condition that the Gibbs-Thomson and kinetic effects are zero. It is interesting to note that the equilibrium liquidus temperature gradient ahead of an infinitely sharp tip is only k_o times the equilibrium liquidus temperature gradient ahead of a planar interface.

3.7 Thermodynamic Constraint; Minimum Rate of Internal Entropy Production

Turning to Eq.(49), we note that the expression for the tip concentration contains one degree of freedom, c_{tip} is a function of p which is the dimensionless radius of curvature of the paraboloidal dendrite tip for a fixed growth velocity. We must ask the question: which p does nature choose in the controlled solidification process? We seek an answer in the thermodynamics of irreversible processes.

In the mathematical sense, any extra condition will remove the degree of freedom. For some time past, the maximum interface temperature condition (or the minimum tip undercooling condition) has been used by certain workers[10,12]. The question of the correctness of the condition has not been answered. The existence of a maximum in the interface temperature is due solely to the contribution of the Gibbs-

Thomson and kinetic effects. To obtain the maximum tip temperature, the radius of the tip must be as small as possible to minimize the solute build-up while the curvature contribution remains small. In metallic systems, the kinetic coefficient is usually large and the radius of curvature for a significant Gibbs-Thomson effect is of the order of 1 μm (typical magnitudes for Fe-Ni systems are shown in later section). Thus the experimentally observed tip radius should be of the same order of magnitude for any growth velocity, which does not agree with observation.

Sharp and Hellawell[20,21] have suggested the condition of zero constitutional supercooling at the dendrite tip as a governing criterion based on their experimental observations of the controlled solidification of some non-ferrous binary alloys. From Eqs.(58) and (60), it is clear that this condition is unattainable with a large radius of tip curvature except in the very low velocity regime because the maximum possible reduction of the equilibrium temperature gradient at the tip without the Gibbs-Thomson effect is only by the factor k_o.

The crucial point here is that both the maximum interface temperature condition and the zero constitutional supercooling condition are concerned with a particular thermodynamic variable of a particular point on the interface, the dendrite tip. These conditions ignore all other thermodynamic conditions and the entire region behind the tip. Clearly, the correct principle, if it exists, must be a global or an integral principle. While previous concepts

may contain some elements of the truth, because they may be proportional to integrals in their specific applications, they have no general foundation in physics.

As reviewed at the beginning of this chapter, the controlled solidification system is a nonequilibrium system with some external constraints. An equilibrium system can be completely defined in terms of free energy. Similarly, if kinetic stability exists, and empirically we know that for certain growth conditions this is the case, then there must also exist a thermodynamic potential function which completely describes the thermodynamics of the nonequilibrium situation. For certain simple systems, this has been identified as the rate of internal entropy production[48,49]. As stated by Prigogine[48] and de Groot[49], a single phase dissipative system with linear phenomenological equations approaches the steady state characterized by the minimum rate of internal entropy production. This theorem has been suggested to be applicable in approximation to the steady state binary alloy solidification problem by Kirkaldy[50-52]. We propose to apply this postulated principle to remove the degree of freedom which we have identified, since the evolution of our model is clearly associated with pure relaxation process.

In our volume diffusion controlled model, the rate of internal entropy production due to diffusion fields per unit volume, σ, can be expressed after de Groot[49] as

$$\sigma = \frac{1}{T} \left(J_q X_q + \sum_{k=1}^{n} J_k X_k \right), \qquad (61)$$

where J is the flux, q and k refer to the thermal and mass variables respectively and X is the thermodynamic force. The thermodynamic forces in Eq.(61) are[49]

$$X_q = - \frac{\nabla T}{T} \tag{62}$$

and

$$X_k = -T \nabla \left(\frac{\mu_k}{T}\right), \tag{63}$$

where μ is the chemical potential. If the thermal and mass diffusion are taken as independent,

$$J_q = - \kappa \nabla T \tag{64}$$

and

$$J_k = \sum_{i=1}^{n} L_{ki} X_i, \tag{65}$$

where κ is the thermal conductivity and L_{ki} are the phenomenological coefficients. Eq.(65) is given with the assumption that the fluxes are linearly related to the thermodynamic forces. For binary alloys,

$$J_1 = -J_2, \tag{66}$$

where subscript 1 and 2 refer to solute and solvent respectively. Hence,

$$\sum_{k=1}^{2} J_k X_k = J_1 (X_1 - X_2). \tag{67}$$

Neglecting the temperature dependence of the chemical potentials,

$$X_1 - X_2 = -V\mu_1 + V\mu_2 = -RT \frac{\nabla c_1}{c_1(1-c_1)}, \tag{68}$$

where R is the gas constant and c_1 is the solute concentration.

Using Fick's relation for mass flow,

$$J_1 = -D\nabla c_1. \tag{69}$$

Substituting Eqs.(68) and (69) into Eq.(67), Eqs.(62), (64), and (67) into Eq.(61), and adjusting the units of all parameters, we obtain

$$\sigma = \kappa \frac{(\nabla T)^2}{T^2} + DR \frac{d}{M} \frac{(\nabla c)^2}{c(1-c)}, \tag{70}$$

where c refers to the solute concentration (subscript 1 is now omitted), d is the density of solvent and M is the mass per mole of solvent (The dilute solution approximation is used).

The total of the rate of internal entropy production, $\frac{d_i S}{dt}$, is the volume integral of σ

$$\frac{d_i S}{dt} = \int_V \sigma \, dV. \tag{71}$$

In our single dendrite model, it is more convenient to define a new thermodynamic function, $\overline{\frac{d_i S}{dt}}$, the average rate of internal entropy production per unit cross sectional area

$$\overline{\frac{d_i S}{dt}} = \frac{1}{\pi x_L^2} \left(\frac{d_i S}{dt}\right), \tag{72}$$

where πx_L^2 is the cross sectional area of a single dendrite. For given growth conditions and given materials constants, $\overline{\frac{d_i S}{dt}}$ is a function of the mass Peclet number p only. Thus the minimum condition gives

$$\frac{\partial}{\partial p}\left(\frac{d_i S}{dt}\right)\Bigg|_{p=p_{opt}} = 0 . \tag{73}$$

All variables for the calculation of Eq.(73), in the parabolic coordinates, can be directly obtained from the experimental conditions and the solution of the diffusion equation.

The temperature gradient in the liquid can be expressed as a function of the tip temperature T_o and the distance in the growth direction, z, from the constancy of the imposed temperature gradient, i.e.,

$$T = T_o + G(z - \frac{\rho}{2}) . \tag{74}$$

The solute concentration is given by

$$c(\alpha,\beta) = c_\infty + \sum_{n=0}^{\infty} (E_n) \frac{e^{p\alpha^2} U(n+1,1,p\alpha^2)}{e^{-p} U(n+1,1,p)} L_n(p\beta^2) . \tag{75}$$

The solute gradient function in the liquid with rotational symmetry is given by

$$(\nabla c)^2 = \frac{1}{\rho^2(\alpha^2+\beta^2)}\left[\left(\frac{\partial u}{\partial \alpha}\right)^2 + \left(\frac{\partial u}{\partial \beta}\right)^2\right], \tag{76}$$

where $\frac{\partial u}{\partial \alpha}$ is given by Eq.(45) and

$$\frac{\partial u}{\partial \beta} = \sum_{n=1}^{\infty} (E_n)(2p\beta) \frac{e^{-p\alpha^2} U(n+1,1,p\alpha^2)}{e^{-p} U(n+1,1,p)} \frac{nL_n(p\beta^2) - nL_{n-1}(p\beta^2)}{p\beta^2} . \tag{77}$$

Eq.(77) is obtained from the identity[46]

$$\frac{d}{dx} L_n^{(\alpha)}(x) = -L_{n-1}^{(\alpha+1)}(x)$$

$$= \frac{nL_n^{(\alpha)}(x) - (n+\alpha) L_{n-1}^{(\alpha)}(x)}{x} . \tag{78}$$

It would appear that a unique p could be determined by optimizing the thermodynamic function with respect to p. However, it should be noted that the boundary limit x_L in Eq.(72) is not predetermined. The problem of determining x_L is considered in the following section.

Special Case

At this juncture, we examine the rate of internal entropy production on a particular point of the interface, the dendrite tip. At this point, Eq.(71) has the simple form

$$\frac{d_i S}{dt} = \frac{\kappa (\nabla T)^2}{T_o^2} + D\,R\,\frac{d}{M}\,\frac{(\nabla c)^2_{\substack{\alpha=1\\ \beta=0}}}{c_{tip}(1-c_{tip})} . \qquad (79)$$

When the first term >> the second term, the minimum condition will be satisfied with the maximum T_o. Thus, the condition of the minimum rate of internal entropy production at the tip is the same as the condition of the maximum tip temperature when the growth velocity is very low, the temperature gradient is high and all the problems behind the tip are ignored.

3.8 Boundary Limit

In the last section, it is shown that the optimization of the thermodynamic function is possible only if the volume integration is possible. The integration limit in the growth direction is clearly from the interface to infinity or to the point where the solute gradient vanishes.

However, the limit in the lateral direction, x_L, is not determined. To determine this, we assume that x_L is proportional to the true spacing λ. The λ vs. v relation is given in most previous studies[8,13,63] by

$$\lambda = kv^{-\frac{1}{2}}, \tag{80}$$

where k is a constant for a given temperature gradient and materials constants. Hence, the relation between x_L and v can be represented by

$$x_L = k'v^{-\frac{1}{2}}. \tag{81}$$

Solving Eq.(73) with the help of Eq.(81), we obtain p_{opt} as a function of k' and v. Thus the corresponding c_{tip} is

$$c_{tip} = f\ (k',v). \tag{82}$$

To determine k', we apply the steady state planar-nonplanar interface transition condition

$$\left.\begin{aligned} c_{tip} &= \frac{c_\infty}{k_o}, \quad v \leq v_{crit} \\ c_{tip} &< \frac{c_\infty}{k_o}, \quad v > v_{crit} \end{aligned}\right\}, \tag{83}$$

where v_{crit} is the critical velocity for the planar-nonplanar interface transition. From Eqs.(82) and (83), we determine k' and finally obtain our goal, c_{tip}, ρ and T_o as a function of growth velocity alone. Substituting these values into Eqs.(36) and (27), we obtain a unique solution of our boundary value problem.

3.9 Computational Problems

The present theory has been completed to predict the tip concentration c_{tip} and the tip radius ρ as a function of growth velocity. However, as shown in the previous sections the integration of the thermodynamic function and its optimization do not simply give an explicit form. Thus, to obtain numerical values for a given set of experimental conditions, we use the following numerical computation scheme:

(i) compute c_{tip} and T_o as a function of p and v.

(ii) compute the rate of internal entropy production due to diffusion fields, σ, in (α,β) space.

(iii) integrate σ numerically with an arbitrary coefficient, k'.

(iv) repeat (iii) applying a general method for finding a root until k' satisfies Eq.(83).

For desired accuracy of the computational results, the scheme requires a large computer memory and a very long computing time. To avoid these difficulties, we seek some simplifications in the light of physical details rather than by reformulation of the computing formulas.

The order of magnitude of the tip radius for a significant curvature effect is less than one micron for most metallic systems. The observed tip radii in our controlled solidification experiments are quite blunt (Fig.28). Furthermore, it is well known that the kinetic undercooling

is minimal in most metallic systems[53]. Under these experimental foundations, the Gibbs-Thomson and kinetic effects can be neglected without any significant error.

Now we consider a further approximation for the integration of the rate of internal entropy production. For a given experimental condition, Eq.(72) has the form in parabolic coordinates

$$\frac{\overline{d_i S}}{dt} = \frac{1}{\pi x_L^2} \quad 2\pi \int_1^{\alpha_1} \int_0^{\beta_1} \rho^3(\alpha^2+\beta^2)\alpha\beta \ \sigma(\alpha,\beta,p)d\beta d\alpha, \quad (84)$$

where $\beta_1 = \frac{x_L}{\rho}$ and α_1 is the point where the solute gradient vanishes. To a first approximation, we assume that the concentration profile in the liquid can be represented by a straight line in the diffusional penetration distance ℓ. Then,

$$\frac{\overline{d_i S}}{dt} = \frac{1}{\pi x_L^2} \quad 2\pi \int_0^{\beta_1} \rho^2(1+\beta^2)^{\frac{1}{2}}\beta\ell \ \sigma(1,\beta,p)d\beta, \quad (85)$$

where $\ell = \ell(\beta,p)$. Putting ℓ = unit length, we can define another thermodynamic function, $\left(\frac{\overline{d_i S}}{dt}\right)_A$, the average rate of internal entropy production on the interface per unit cross sectional area

$$\left(\frac{\overline{d_i S}}{dt}\right)_A = \frac{1}{\pi x_L^2} \quad 2\pi \int_0^{\beta_1} \rho^2(1+\beta^2)^{\frac{1}{2}}\beta \ (\text{unit length}) \ \sigma \ (1,\beta,p)d\beta \quad (86)$$

We define a variable $\bar{\Gamma}$, the average penetration distance of the diffusion profile as

$$\bar{\ell}(p) = \frac{\int_0^{\beta_1} 2\pi\rho^2(1+\beta^2)^{\frac{1}{2}}\beta\ell(\beta,p)\,d\beta}{\int_0^{\beta_1} 2\pi\rho^2(1+\beta^2)^{\frac{1}{2}}\beta\,d\beta} \quad . \tag{87}$$

When v is small and p is large (blunt tip), $\ell \simeq \bar{\ell}$, near the tip. Upon substituting this estimate into Eq.(85), we obtain

$$\frac{\overline{d_i S}}{dt} \simeq \bar{\ell}\left(\frac{\overline{d_i S}}{dt}\right)_A , \tag{88}$$

and hence, the minimum condition gives

$$\frac{\partial}{\partial p}\left(\frac{\overline{d_i S}}{dt}\right) \simeq \frac{\partial \bar{\ell}}{\partial p}\left(\frac{\overline{d_i S}}{dt}\right)_A + \bar{\ell}\,\frac{\partial}{\partial p}\left(\frac{\overline{d_i S}}{dt}\right)_A = 0 , \tag{89}$$

or

$$\frac{\partial}{\partial p}\left(\frac{\overline{d_i S}}{dt}\right)_A = -\frac{\left(\frac{\overline{d_i S}}{dt}\right)_A \frac{\partial \bar{\ell}}{\partial p}}{\bar{\ell}} . \tag{90}$$

$\left(\frac{\overline{d_i S}}{dt}\right)_A$ and $\bar{\ell}$ are positive definite, and hence the sign of $\frac{\partial}{\partial p}\left(\frac{\overline{d_i S}}{dt}\right)_A$ is entirely dependent on the p dependence of $\bar{\ell}$. Note that ℓ decreases at the tip and increases behind the tip as p decreases. Thus we may qualitatively assume that $\bar{\ell}$ is independent of p, and $\frac{\overline{d_i S}}{dt}$ and $\left(\frac{\overline{d_i S}}{dt}\right)_A$ have the minimum at the same p. From this, we shall optimize $\left(\frac{\overline{d_i S}}{dt}\right)_A$ in our computation. It should be borne in mind that the above approximation is reasonable for small v and large p, however it becomes defective for small p.

The necessary variables for the computation are:

$$\sigma(1,\beta) = \frac{\kappa(\nabla T)^2}{T(1,\beta)^2} + DR\,\frac{d}{M}\,\frac{(\nabla c)^2_{\alpha=1}}{c(1,\beta)\{1-c(1,\beta)\}}\,, \qquad (91)$$

$$T(1,\beta) = T_o - \tfrac{1}{2}G\rho\beta^2, \qquad (92)$$

$$c(1,\beta) = c_{tip} - \tfrac{1}{2}\,\frac{G}{m}\beta^2\,,$$

$$(\nabla c)^2_{\alpha=1} = \frac{1}{\rho^2(1+\beta^2)}\left[\left(\frac{\partial u}{\partial \alpha}\right)^2_{\alpha=1} + \left(\frac{\partial u}{\partial \beta}\right)^2_{\alpha=1}\right], \qquad (93)$$

$$\left(\frac{\partial u}{\partial \alpha}\right)_{\alpha=1} = (-2p)\left[(c_{tip}-c_\infty)\frac{1}{pe^{pE_1(p)}} - \frac{DG}{mv}\left\{\frac{1}{pe^{pE_1(p)}} - \frac{p^{-1}-e^{pE_1(p)}}{e^{pE_1(p)}(1+p)-1}\,(1-p\beta^2)\right\}\right] \qquad (94)$$

and

$$\left(\frac{\partial u}{\partial \beta}\right)_{\alpha=1} = (-2p\beta)\,\frac{DG}{mv}\,. \qquad (95)$$

3.10 Application to the Fe-8 wt.% Ni System

In this section, we apply the present theory to a particular system, the Fe-8 wt.% Ni system. This system has been chosen from the fact that its thermodynamic data are already well established[54-56] and the diffusion coefficient in the solid is small. Also the tendency of Ni to oxidize preferentially is small, and the liquidus and solidus slopes (absolute value) are small, allowing good correlations to be made between concentration in the solid and temperature.

The relevant part of the Fe-Ni phase diagram is reproduced from Hansen's work[54] in Fig. 4. The equilibrium distribution coefficient for 8 wt.% Ni, k_o, is obtained as 0.68 from Fig. 4. This value can be checked by thermodynamic calculation as follows: In a system of solid (γ-phase) and liquid mixture of an Fe-8 wt.% Ni alloy, the condition of equilibrium gives

$$\mu_{Ni}^{S} = \mu_{Ni}^{L} , \tag{96}$$

where μ_{Ni}^{i} is the chemical potential of Ni in phase i.

Expressing chemical potentials as

$$\mu_{Ni}^{i} = \mu_{Ni}^{io} + RT \ln \gamma_{Ni}^{'i} c_{Ni}^{'} , \tag{97}$$

where μ_{Ni}^{io} is the free energy of nickel at the standard state in phase i, $\gamma_{Ni}^{'i}$ is the activity coefficient of nickel in phase i and $c_{Ni}^{'i}$ is the atomic concentration of nickel in phase i, Eq. (96) has the form

$$\mu_{Ni}^{So} + RT \ln \gamma_{Ni}^{'S} c_{Ni}^{'S} = \mu_{Ni}^{Lo} + RT \ln \gamma_{Ni}^{'L} c_{Ni}^{'L} . \tag{98}$$

From Eq. (98), the equilibrium distribution coefficient for the atomic concentration, $k_o^{'}$, can be represented as

$$k_o^{'} = \frac{c_{Ni}^{'S}}{c_{Ni}^{'L}} = \frac{\gamma_{Ni}^{'L}}{\gamma_{Ni}^{'S}} \exp\left(\frac{\Delta\mu_{Ni}^{o}}{RT}\right) , \tag{99}$$

where $\Delta\mu_{Ni}^{o} = \mu_{Ni}^{Lo} - \mu_{Ni}^{So}$.

Expressing $k_o^{'}$ in terms of weight concentration, c_{Ni}^{1},

$$k_o' = \left[\frac{1}{1 + \frac{100 - c_{Ni}^S}{c_{Ni}^S} \frac{M_{Ni}}{M_{Fe}}} \right] \Bigg/ \left[\frac{1}{1 + \frac{100 - c_{Ni}^L}{c_{Ni}^L} \frac{M_{Ni}}{M_{Fe}}} \right]$$

$$= k_o \frac{100 \frac{M_{Ni}}{M_{Fe}} + c_{Ni}^L \left(1 - \frac{M_{Ni}}{Fe}\right)}{100 \frac{M_{Ni}}{M_{Fe}} + c_{Ni}^S \left(1 - \frac{M_{Ni}}{M_{Fe}}\right)} . \qquad (100)$$

For 8 wt.% Ni alloy,

$$k_o' = 0.9988\, k_o = k_o \qquad (101)$$

Substituting values of various thermodynamic variables into Eq.(99), we obtain

$$k_o' = 0.662 \qquad (102)$$

In this estimate, we have used $\gamma_{Ni}^{'L} = 0.67$,[55] $\gamma_{Ni}^{'S} = 0.97$[56] $\Delta\mu_{Ni}^{o} = -128.2188$ cal/mole (calcualted from Ref. 57) and $T = 1781.16^{o}K$. The value in Eq. (102) is in good agreement with that obtained from Hansen's phase diagram.

Some other values of necessary parameters for the present calculation are obtained from various sources as follows:

T_M : $1802.5^{o}K (1529.5^{o}C)$, the melting temperature of γ iron obtained by extrapolation of γ iron-liquid transition in Hansen's phase diagram. This value is in good agreement with the thermodynamically calculated value of Hone[58].

m : $-2.65^{o}K$/wt.% Ni, the liquidus slope obtained from Hansen's phase diagram.

γ : 220 erg/cm^2 (=5.3 x 10^{-6}cal/cm^2), solid-liquid interfacial energy of pure iron[59].

μ_o: 200 cm/sec ^{o}K, the linear kinetic coefficient, by assumption.

L : 3873 cal/mole (=485.5 cal/cm^3), the latent heat of fusion of pure γ iron[60].

D : 5 x 10^{-5} cm^2/sec, the diffusion coefficient of Ni in dilute Fe-Ni melts at $1600^{o}C$[61].

d : 7 g/cm^3, the density of pure iron at $1564^{o}C$[78].

κ : 0.1 cal/sec cm ^{o}K, the thermal conductivity of pure liquid iron at $1600^{o}C$[62].

Experimental conditions were adjusted to give

c_∞: 8 wt.% Ni, the bulk concentration of the liquid.

G : $31^{o}C$/cm, the imposed temperature gradient.

The variations of the tip concentration as a function of solute Peclet number have been evaluated for various growth velocities from Eqs.(54) and (49). Results are shown in Fig. 5 and 6. The tip concentration of the solid phase, c^S_{tip}, is defined by

$$c^S_{tip} = k_o c_{tip}. \qquad (103).$$

The c^S_{tip} in Fig. 5 is the one which simultaneously satisfies the solute diffusion equation, local equilibrium boundary condition and mass balance at the tip, whereas, the c^S_{tip} in Fig. 6 is the one which satisfies all the above conditions

plus the Gibbs-Thomson and kinetic effects. It should be noted that the Gibbs-Thomson and kinetic effects are significant when $\rho < 1\mu m$ for most growth velocities.

From Eqs.(50) and (104), the tip undercooling, $\Delta T(1,0)$, has been evaluated for some growth velocities and shown in Fig. 7, where $\Delta T(1,0)$ is defined by

$$\Delta T(1,0) = T_M - T_o = \Delta T_s(1,0) + \Delta T_c(1,0) + \Delta T_k(1,0). \quad (104)$$

It is noted in this illustration that the corresponding radius of tip curvature, ρ, to the maximum T_o (or minimum $\Delta T(1,0)$) is of the order of 1 μm or less for most growth velocities and is an increasing function of the growth velocity in the low velocity regime.

We define an index of the amount of constitutional supercooling at the tip, $\mathcal{J}(1,0)$, by

$$\mathcal{J}(1,0) = G_e^o - G. \quad (105)$$

The variations of $\mathcal{J}(1,0)$ as a function of p are evaluated from Eqs.(105) and (53) for some growth velocities and shown in Fig. 8. It is shown that the p dependence is not strong in the regime where the Gibbs-Thomson and kinetic effects are minimal, compared with the velocity dependence.

We now examine the thermodynamic properties behind the tip. The rate of internal entropy production at the interface has been evaluated from Eq.(91) ignoring the Gibbs-Thomson and kinetic effects. Computed results for two different growth velocities are plotted in Fig. 9 and Fig. 10. These figures show that the calculated rate of internal

entropy production decreases at the tip, but increases behind the tip, with decreasing radius of tip curvature. Physically, the smaller tip radius provides a more relaxed tip but simultaneously creates a less favorable situation behind the tip. From this, we can qualitatively understand why a growing dendrite does not adopt a very sharp tip. In Figs. 9 and 10, it is also observed that the variation of $c(1,s)$ is not monotonic in the higher velocity regime. We suspect that it might indicate the tendency of side branching in the higher velocity regime; however the critical analysis of this problem is beyond the scope of the present work.

Finally, from Eq.(86), we compute the average rate of internal entropy production on the interface, $\left(\frac{\overline{d_i S}}{dt}\right)_A$, as a function of p and v. Computed results for some growth velocities are shown in Fig. 11. The minimum condition gives a unique p and we obtain corresponding optimum c^S_{tip} from Fig. 5. Thus c^S_{tip} and p can be plotted as a function of v alone for a fixed G. These are shown in Fig. 12 and 13 respectively. It is noted that both c^S_{tip} and p are rapidly decreasing functions with increasing v for low v (cellular regime) and slowly decreasing functions for higher v (dendritic regime). Also noted is the significant amount of solute build-up ahead of the dendrite tip.

CHAPTER 4

EXPERIMENT

4.1 Experimental Program

Since the first success of the quantitative description of the solidification process by Chalmers et al.[1], the technique of controlled unidirectional solidification has established a firm place in solidification literature. Although this technique has been applied by a number of workers[13,18,20] to ferrous and nonferrous alloy systems and organic compounds, few studies have been conducted systematically to correlate the morphological development and the variation of the solute segregation in terms of the imposed temperature gradient and growth velocity. Thus it was decided, in the present experimental study, to separate the growth parameters by using a controlled gradient moving furnace to investigate the following problems:

(i) The growth velocity dependence - The first objective of the present experiment was to observe the evolution of the interface morphology and the variation of the microsegregation, as a function of growth velocity in the range of 5-400 mm/hr for a fixed temperature gradient.

(ii) The temperature gradient dependence - The above variations were examined by varying the temperature

gradient and fixing the growth velocity approximately constant.

(iii) The homogenization kinetics of the microsegregation in solid - The microsegregation homogenizes after solidification by diffusive processes. This problem in the Fe-8wt.%Ni, Fe-18wt.%Cr-8wt.%Ni and Fe-18wt%Cr-8wt.%Ni-0.35wt.%C systems was examined by quantitative determination of the segregation profiles.

In the present controlled solidification experiments, the Fe-8wt.%Ni system has been chosen from the reasons mentioned in the preceding chapter and with the additional object of increasing our knowledge of the steady high temperature solidification process.

4.2 Specimen Preparation

Fe-8wt.%Ni alloy specimens were prepared from U.S. Steel Ferrovac-E iron (99.94wt.%Fe) and Falconbridge electrolytic nickel (99.97wt.%Ni). Electrolytic chromium (99.8wt.%Cr) and Union Carbide graphite (99.98wt.%C) were used for Fe-18wt.%Cr-8wt.%Ni alloy specimens and Fe-18wt.%Cr-8wt.%Ni-0.35wt.%C alloy specimens. The chemical analyses of pure iron and nickel are given in Table 1.

Weighed materials (about 40g) were melted in an argon arc melting unit and quenched in a water cooled copper mold of the same unit to give a high degree of long range chemical homogenity. By this melting technique, the long range homogenity of the quenched ingots was proved to be satisfactory by wet analysis of both ends of the ingots, and the change of the concentration

of nickel and chromium during the process was minimal. The carbon concentration was determined by the combustion analysis technique after the ingot making process. The quenched ingots were swaged into 4.5 mm dia. rod to fit the alumina tube used as a sample container in the solidification experiments.

4.3 Controlled Solidification

A molybdenum wound vertically travelling furnace was used, which was built originally by Hone [58]. It was rebuilt with slight modifications in the furnace winding and power supply to give a wider range of power inputs. The overall assembly consists of a furnace drum, an evacuation unit, a furnace travelling unit, power supply, gas supply and water cooling system. The sectional view of the furnace is shown in Fig. 14. The allowable vertical travel rates were from 5 to 500 mm/hr. The three internal molybdenum windings were controlled so as to produce different thermal gradients. The positive temperature gradient with vertical furnace design was chosen so as to give the growth condition itself and to minimize the natural convection of the melt due to gravitational field.

The characteristics of the furnace are:

(i) Close control over the growth parameters, G and v, is permitted.

(ii) The temperature stability at any given point is better than 2°C during the time required for typical solidification experiments.

(iii) Convective stirring is negligible, this was proved by a semiinfinite liquid diffusion couple, Fe/Fe-8wt.%Ni

(5 mm in diameter), held in the furnace for two hours at 1550°C. The diffusion coefficient obtained from this analysis was precisely that determined by Purdy and Subramanian[61] in capillary diffusion experiments, indicating that mixing in the furnace under these conditions was by diffusion only.

The solidification experiment involved melting the specimen in a high purity alumina tube (sometimes containing thermocouples inside the specimen) under argon atmosphere and moving up the furnace at a desired velocity. After the furnace travelled the desired distance, usually about 50 mm, the specimen was quenched by dropping it into water. The temperature profiles of the furnace and specimen were measured using a Pt/Pt-13wt%Rh thermocouple. The overall temperature profile of a specimen was slightly different from the temperature profile of the furnace, and the difference was dependent on the geometrical arrangement of the specimen. It was found that, with the geometrical arrangement of about 8 cm melt in a total 30 cm length specimen, the temperature gradient of the specimen at the liquidus temperature was nearly the same as that of the furnace. After this, all the solidification experiments were carried out with the same geometrical arrangement.

A series of Fe-8wt.%Ni alloy solidification experiments were carried out for various temperature gradients and growth velocities. Some of them are summarized in Fig. 15 to show the velocity dependence of the solidification structure for a constant

temperature gradient (31 ^{o}C/cm). Three specimens which solidified with different temperature gradients and nearly the same growth velocities are shown in Fig. 16. In both figures, the top and bottom rows show the transverse and longitudinal sections, respectively. The morphological development may be inferred from the observed segregation pattern. The cellular solidification at low velocity is evident. Increasing the growth velocity, the stronger development of cells, the transition to the cellular dendritic morphology with secondary arms and the cellular dendritic structure with tertiary arms appear in sequence. The velocity dependence of the observed spacing of cells and cellular dendrites is in reasonable agreement with the prediction of previous work[18,13,63] for dendritic growth, but strongly deviates in the low velocity regime. The effect of temperature gradient on the morphological development is shown in Fig. 16. It is observed that the spacing decreases with increasing temperature gradient and side branching is evident with low gradient for this particular growth velocity.

Figs. 17 and 18 show the longitudinal sections of Fe-8wt.%Ni, Fe-18wt.%Cr-8wt.%Ni and Fe-18wt.%Cr-8wt.%Ni-0.35wt.%C specimens which solidified under approximately same growth conditions. These results indicate that Fe-18wt.%Cr-8wt.%Ni alloy solidified initially as δ-phase and subsequently transformed to γ-phase, and nearly complete homogenization occurred under the given experimental condition, as expected from the large diffusion coefficients of substitutional solutes in δ-phase. On the other

hand, negligible homogenization is qualitatively observed in the specimens of Fe-8wt.%Ni and Fe-18wt.%Cr-8wt.%Ni-0.35wt.%C alloys which solidified directly as γ-phase from the melt.

4.4 Metallography

To investigate the solidification structure, solidifed specimens were cut into parallel (longitudinal) and vertical (transverse) section to the growth direction and prepared by conventional metallographic procedures, mounting, grinding, polishing and etching. Metallographic etching techniques commonly found in the literature[64-66] were applied to show the solute segregations. The results were not quite satisfactory particularly with Fe-18wt.%Cr-8wt.%Ni alloy specimens and weakly segregated iron-nickel alloy specimens solidified in the low velocity regime. A high contrast etching condition may be developed in principle by optimizing the formation of local electric cells for a given inhomogenity of oxidation potentials due to solute segregation of a specimen. The condition depends on the kind, concentration and mobility of anions and cations which are contained in the etching reagent. It is not a simple problem to find the condition by a quantitative theory. With a qualitative knowledge, a series of experiments were carried out and an improved condition has been obtained for iron-nickel alloys by an adjustment of the composition of the Oberhoffer's reagent [67]. In addition, an etching reagent for 18-8 steels has also been developed based on the sulfide film contrast technique [68,69]. Details are included in Table 2, and improved results using these new reagents are

shown in Fig. 19 for Fe-8wt.%Ni alloy specimens and in Fig. 20 for an Fe-18wt.%Cr-8wt.%Ni alloy specimen.

4.5 Electron Probe Microanalysis

Electron probe microanalysis was employed for the quantitative determination of the segregation profile. Following metallographic examination of the specimens, regions were selected for microanalysis and marked with a microhardness indentor. After indentation, the specimens were photographed and slightly repolished to remove the surface film and roughness which resulted from the etching process.

The concentration profile of nickel of the selected region was determined on an Acton-Cameca microanalyser. The operating condition for the optimum X-ray output of Ni K_α was found to be 15 kv of accelerating voltage and 150 na of specimen current. Measurements were carried out by point counting for 20 seconds at an increment of 5.4 μm.

The measured counting rates were corrected by Haworth's correction procedure[70] which utilizes the atomic number correction of Duncumb and Reed [71], absorption correction of Philibert[72], and fluorescence correction by the modified Castaing's procedure[73]. The measured counting rate of a point was converted into the measured intensity ratio, and the concentration of nickel was obtained by interpolating the measured intensity ratio to the calculated intensity ratio vs. concentration relation which was obtained via atomic number correction and absorption correction (fluorescence correction is not necessary for nickel determination in iron-nickel binary alloys and iron-

nickel-chromium ternary alloys).

The micrographs of the selected regions and the variations of the solute segregation profiles as a function of growth velocity under a fixed temperature gradient are shown in Fig. 21. The analysed transverse sections in this experiment are about 8 mm below the final solid-liquid interface. From Fig. 21, the variation of the minimum (at the tips) and the maximum solute concentrations (at the interdendritic regions) as a function of growth velocity is summarized in Fig. 22. The probable error in the experimentally determined concentration is typically ±0.13wt.%Ni, and the error in the estimation of $k_o C_\infty$, which arises from the uncertainty of the phase diagram, is ±0.25wt.%Ni. It is noted in Fig. 22 that the minimum nickel concentration at the tip decreases rapidly with increasing growth velocity in the cellular regime; however, there is little variation in the dendritic regime. It is also noted that, under our experimental conditions, the experimentally determined minimum concentration at the tip is much higher than $k_o C_\infty$ even if homogenization after solidification is taken into account (the effect of homogenization is considered in the next section). Thus, we have experimental evidence that there exists a significant amount of solute build-up in front of the tip even in the dendritic growth regime (like Backerud[36] and Doherty's[37] experimental observation but unlike the assumption of most microsegregation models)[14,19].

Some of the probe results are summarized in Fig. 23 to show the temperature gradient dependence of the microsegregation.

Clearly observed is the decreased segregation intensity with higher gradient.

4.6 Homogenization Kinetics in the Solid

To avoid the uncertainty of the exact final steady state interface position of the solidified specimens, electron probe microanalysis was carried out on sections approximately 8 mm below the approximated final interface. Therefore, the observed concentration profile has been influenced by solid state diffusion after solidification. The nature of homogenization due to diffusive processes in the solid phase has been studied by many workers. Purdy and Kirkaldy's recent review paper[74] is a good summary of the related work.

The segregation pattern arising from a unidirectional solidification process may be approximated as cylindrical, provided the imposed temperature gradient is relatively high or the growth velocity is relatively low. This is the case for most of our experimental operations. The time dependent diffusion equation in cylindrical coordinates (r,θ) with rotational symmetry has the form

$$\frac{\partial c}{\partial t} = D_s\left(\frac{\partial^2 c}{\partial r^2} + \frac{1}{r}\frac{\partial c}{\partial r}\right), \qquad (106)$$

where D_s is the solute diffusion coefficient in solid phase. D_s is assumed as a constant from the fact that the temperature and concentration variations are small in our consideration. The impermeable wall boundary condition gives

$$\frac{\partial c}{\partial r} = 0, \quad \text{at } r=0 \text{ and } r=r_1, \; t > 0, \qquad (107)$$

where r_1 is the radius of the cylindrical segregation profile. Any arbitrary initial solute distribution gives the initial condition

$$c(r,0) = f(r), \quad t = 0 \tag{108}$$

The solution of Eq. (106) for the initial and boundary conditions given has been obtained by Crank[75] as

$$c(r,t) = \frac{2}{r_1^2}\left[\int_0^{r_1} r' f(r')dr' + \sum_{n=1}^{\infty} e^{-D_s\alpha_n^2 t} \frac{J_o(r\alpha_n)}{J_o^2(r_1\alpha_n)} \int_0^{r_1} r' f(r') J_o(\alpha_n r')dr'\right], \tag{109}$$

where α_n are the roots of

$$J_1(r_1\alpha_n) = 0 \tag{110}$$

and $J_n(x)$ is the Bessel function of order n [42,45,46].

A typical example of the decay of an initial profile of an Fe-8wt.%Ni specimen solidified with G = 31°C/cm and v = 370 mm/hr is shown in Fig. 24. In this calculation, we have used T = 1753.16°K and $D_s = 3.41 \times 10^{-9}$ cm^2/sec [76]. In Fig. 24, we clearly see that there is no significant change of the profile in the central regions where the gradient is small, whereas the interdendritic region (where the concentration gradient is high) shows relatively fast decay. Calculations for various velocities show that the same is true for any growth velocity. This is due to the fact that the homogenization time and the cell spacing

increase and the average solute gradient of the profile decreases as the growth velocity decreases. This analysis indicates that in austenitic iron-nickel alloy the diffusional homogenization is minimal and specifically that no significant change of the solute concentration occurs in the central region of dendrites during cooling down. Fig. 25 shows micrographs and typical concentration profiles resolved by electron probe microanalysis of two transverse sections of unidirectionally grown Fe-8wt.%Ni alloy specimens. Fig. 25a is 0.3 mm below the tip of a specimen grown with G = 31°C/cm and v = 51 mm/hr (where the interdendritic region is still liquid) and Fig. 25b is 8 mm below the tip of a specimen grown with G = 31°C/cm and v = 58 mm/hr. The tip concentrations in the solid are nearly the same.

Turning to the liquid to δ iron solidification, we have qualitatively observed nearly complete homogenization with an Fe-18wt.%cr-8wt.%Ni alloy specimen. This is due to the much greater diffusion coefficient of a substitutional solute in the δ phase. The strong dependence of the diffusion coefficient on the homogenization kinetics is evident by its exponential relation in Eq. (109).

A technique for the approximate determination of the diffusion coefficient in a high temperature phase can be developed by a combination of the steady state unidirectional solidification and the homogenization kinetics of cylindrical solute distribution. A solidification condition gives the values for r_1 and t in Eq. (109). If we experimentally measure the initial and final concentration profile for a given time, D_s is the only

parameter which should satisfy Eq. (109). This technique may be particularly useful for the determination of the diffusion coefficient in the high temperature phase of a multicomponent system where the diffusion couple experiment is technically difficult. A good example is the δ phase of an Fe-18wt.%Cr-8wt.%Ni alloy which exists in a narrow temperature range (about 50°C) right below its solidification temperature. An application of this technique to the alloy is illustrated in Fig. 26 and gives 1.3×10^{-7} cm^2/sec for the diffusion coefficient of Ni at 1480°C (δ-phase). It is interesting to note that this value is close to the diffusion coefficient of Ni extrapolated to that temperature in the expression for the diffusion coefficient of Ni in α-iron (1.045×10^{-7} cm^2/sec) (76).

The main object of this section has been to demonstrate that the minimum concentrations measured correspond closely to those which existed at the dendrite tips (in Fe-8wt.%Ni) during growth. However, the importance of the $\delta \rightleftarrows \gamma$ transition in influencing diffusional homogenization of steels is well established by these observations.

CHAPTER 5

DISCUSSION

5.1 Tip Concentration and Curvature as a Function of Growth Velocity

In the physical sciences, the interplay of theory and experiment is sufficiently important that advances on the one front should ideally be complemented by developments on the other, in order that both may be kept honest. In the present work, the tip concentration and curvature have been theoretically and experimentally obtained as a function of growth velocity alone under a fixed temperature gradient. In this section, we shall compare our theoretically predicted values with our experimental results.

The Tip Concentration

We first consider the tip concentration. The theoretically predicted and experimentally determined tip concentrations are compared in Fig. 27. Also shown in the same figure are the predicted values of the tip concentration by the minimum undercooling and the zero constitutional supercooling conditions. It is clearly shown that these latter values do not agree with experimental results in any sense.

In spite of many approximations in the present theoretical development and computation, the growth velocity dependence of the tip concentration has the same character; very rapidly decreasing with increasing v in the low v regime (cellular) and minimal v dependence in the high v regime (dendritic). Good agreement between the theory and experiment is also seen in the significant amount of solute build-up ahead of the dendrite tip. However, in their magnitudes, the theory and experiment do not agree particularly well. The theoretically predicted tip concentration is about 1 wt.% Ni lower than the experimentally determined tip concentration. This deviation could be due to the following factors:

(i) Interface shape - To avoid mathematical difficulty, we have described our boundary value problem with the shape of a paraboloid of revolution which is exact only if the interface is isothermal and the growing dendrite is completely isolated in an infinite field. In actual growth processes during the controlled solidification experiments, the interface is nonisothermal due mainly to the imposed temperature gradient, and the growth front includes an array of dendrites. Furthermore, in the high growth velocity regime, side branching occurs behind the tip. Clearly the effect of positive temperature gradient gives higher rates of internal entropy production behind the tip and the effect of the array of dendrites and side branches gives lower rates of internal entropy production behind the tip, resulting a net deviation, Δ, from the average rate of internal entropy

production on the interface, $\left(\overline{\frac{d_i S}{dt}}\right)_A$, estimated in the present theory. Thus the true value of the average rate of internal entropy production, $\left(\overline{\frac{d_i S}{dt}}\right)_A^T$, can be represented as

$$\left(\overline{\frac{d_i S}{dt}}\right)_A^T = \left(\overline{\frac{d_i S}{dt}}\right)_A + \Delta \ . \tag{111}$$

At the minimum of the $\left(\overline{\frac{d_i S}{dt}}\right)_A^T$ vs. p curve,

$$\frac{\partial}{\partial p}\left(\overline{\frac{d_i S}{dt}}\right)_A^T \Bigg|_{p=p_{opt}^T} = \frac{\partial}{\partial p}\left(\overline{\frac{d_i S}{dt}}\right)_A + \frac{\partial \Delta}{\partial p} = 0, \tag{112}$$

or

$$\frac{\partial}{\partial p}\left(\overline{\frac{d_i S}{dt}}\right)_A = -\frac{\partial}{\partial p}\Delta \ . \tag{113}$$

a. When $\frac{\partial}{\partial p}\Delta < 0$, the slope of the calculated curve based on our theory is positive at the true minimum, and hence $p_{opt}^T > p_{opt}$. A higher tip concentration is expected.

b. When $\frac{\partial}{\partial p}\Delta = 0$, $p_{opt}^T = p_{opt}$. The calculated tip concentration is the true tip concentration.

c. When $\frac{\partial}{\partial p}\Delta > 0$, $p_{opt}^T < p_{opt}$. The true tip concentration will be lower than the calculated value.

A rigorous analysis of the properties of Δ is a very complex problem and beyond the scope of the present work. Qualitatively we assume that the temperature gradient effect is stronger than the other effects. Then the case falls into the criterion a.

(ii) Inconstancy of k_o - In the present theoretical analysis, the distribution coefficient k_o was assumed to be

a constant. The actual Fe-Ni phase diagram shows that k_o increases with increasing solute concentration, reaching about 0.76 at 10 wt.% Ni and unity at 65 wt.% Ni. Clearly this will give a positive deviation of the tip concentration from the calculated value.

The Tip Curvature

Experimental measurement of the tip radius presents a rather difficult problem because the decanting and direct observation techniques are essentially inapplicable for iron base alloys, and the quenching operation during solidification usually does not allow one to retain the exact shape of the growth front. Only approximate shape observation is possible, and we employed the quenching technique for this purpose. Fig. 28 shows the longitudinal section of an Fe-8 wt.% Ni specimen quenched during steady state growth with G = 31°C/cm and v = 51mm/hr. A comparison of the experimental result with the various predicted tip curvatures is shown in Fig.29. Here, the order of magnitude agreement between our theory and experiment is clearly observed. In our theory, it is demonstrated that the Gibbs-Thomson effect is significant when $\rho < 1\mu m$. If the dendrite tip adjusts itself in such a way that it maximizes the tip temperature, it should become sharper and sharper to reduce the undercooling due to solute build-up ahead of the tip until the Gibbs-Thomson effect starts to play a significant role, which is at most 1μm. This is clearly not the case in Fig. 28. The curvature apparent in Fig. 28 also supports the

hypothesis that the Gibbs-Thomson effect can be neglected without any significant error in the velocity regime under consideration.

5.2 Solute Field in the Liquid

Having determined c_{tip} and ρ as a function of growth velocity, it now is possible to evaluate the solute concentration profile in the liquid as a function of growth velocity alone. Typically we shall examine the concentration profile in the axis of $x = 0$ and $y = 0$, ignoring the Gibbs-Thomson and kinetic effects. The equation of this profile can be obtained simply by putting $\beta=0$, $\gamma=0$ and $\varepsilon_o=\infty$ in Eqs. (27) and (36).

$$c(\lambda,o)=c_\infty+(c_{tip}-c_\infty)\frac{E_1(p\alpha^2)}{E_1(p)}-\frac{GD}{mv}\left[\frac{E_1(p\alpha^2)}{E_1(p)}-\frac{E_1(p\alpha^2)(1+p\alpha^2)-e^{-p\alpha^2}}{E_1(p)(1+p)-e^{-p}}\right]. \tag{114}$$

Computed results for some growth velocities are plotted in Fig. 30. Particularly to be noted is the simultaneous representation of the increased solute gradient and decreased diffusional penetration in the liquid and the decreased tip concentration as growth velocity increases.

5.3 Constitutional Supercooling

The physical details around a growing dendrite tip are clarified in the present investigation. We shall now examine the variation of the amount of constitutional supercooling, $\Delta(1,0)$, as a function of growth velocity. This computation has been carried out from Eqs. (105) and (55), ignoring the Gibbs-Thomson and kinetic effects. The

result is shown in Fig. 31. The amount of the constitutional supercooling for the virtual limiting cases, planar interface and infinitely sharp tip, are also shown in the same figure. It is noted that, as discussed by Tiller[77], there remains a significant amount of constitutional supercooling ahead of a growing tip except for the very low velocity regime.

The reduction of $\mathcal{J}(1,0)$ by introducing two extreme interface curvatures can be estimated by considering the equilibrium temperature gradient. From Eqs.(58) and (60) we see that the equilibrium temperature gradient in front of an infinitely sharp tip is reduced from that at a planar interface simply by the factor k_o, i.e. ,

$$(G_e^o)_{\rho=0} = k_o (G_e^o)_{\rho=\infty} . \tag{115}$$

Hence, the ratio of the amount of constitutional supercooling is

$$\frac{\mathcal{J}(1,0)\big|_{\rho=0}}{\mathcal{J}(1,0)\big|_{\rho=\infty}} = \frac{k_o (G_e^o)_{\rho=\infty} - G}{(G_e^o)_{\rho=\infty} - G} . \tag{116}$$

When $G_e^o >> G$ (all cases except for the very low v regime),

$$\frac{\mathcal{J}(1,0)\big|_{\rho=0}}{\mathcal{J}(1,0)\big|_{\rho=\infty}} = k_o . \tag{117}$$

Further reduction is due to the contribution of the Gibbs-Thomson effect; the magnitude of the constitutional supercooling with the infinitely sharp tip approaches $-\infty$. Thus zero constitutional supercooling at the tip is possible for any growth velocity but it requires a very sharp tip except

for the very low velocity regime. For the growth geometry in which local equilibrium is closely held, the constitutional supercooling in front of a growing tip cannot be eliminated.

5.4 Cell and Dendrite Spacings

In the present theory, the boundary limit of a single dendrite, x_L, has been determined by a self-consistent method using an empirical rule for the spacing vs. growth velocity relation. The physical significance of x_L can be interpreted as the half spacing of the hypothetical paraboloidal dendrite array. In an array of real dendrites, as in our experiments, there exist the interaction of the solute field behind the tip and the effect of the temperature gradient. Thus, the spacing of the real dendrites, λ, must be smaller than $2x_L$. In Fig. 32, λ and $2x_L$ are shown as a function of growth velocity for a fixed temperature gradient ($31^{\circ}C/cm$). Two important features are noted in the figure:

(i) As expected, λ and $2x_L$ are in the same order of magnitude, and clearly $\lambda < 2x_L$.

(ii) Experimentally observed spacings roughly obey the inverse square root dependence of λ on v in the high velocity regime; however, strong deviation is observed in the low velocity regime.

The strong deviation in the low velocity regime may be rationalized in terms of the rate of internal entropy production. Close examination of Fig. 11 shows that for low growth velocities the variation of $\left(\overline{\frac{di_S}{dt}}\right)_\lambda$ near the minimum is very small in a wide range of p, whereas that for high

velocities is quite strong. Thus small deviation of $\left(\frac{\overline{d_i S}}{dt}\right)_A$ from its minimum may permit a wide range of p values, giving rise to a wide scattering of cell shapes in the low velocity regime. In fact, the experimentally observed morphology (Fig. 15) shows fairly uniform dendrites in the high velocity regime and nonuniform cell sizes in the low velocity regime.

5.5 The Effect of Temperature Gradient

Up to this point, we have mainly investigated the growth velocity dependence of the tip properties for a fixed temperature gradient. Let us finally examine the effect of temperature gradient on the tip properties and the cell or dendrite spacing. This investigation can be made in a straightforward way simply by computing all the formulas with various G. Computed results with G = 42°C/cm are shown in Figs. 12, 16 and 32. It is noted in the figures that, when G is increased, the tip concentration and radius of tip curvature increase in the low velocity regime and the spacing decreases in the entire velocity regime. Comparing the theoretically predicted variations with the experimentally observed gradient dependence of the tip concentration (Fig. 23) and spacing (Fig. 16), we find that these predicted effects of varying temperature gradient are indeed borne out by experiment.

CHAPTER 6

SUMMARY REMARKS

(1) A mathematical model has been developed to describe the controlled solidification of dilute binary alloys using a paraboloidal shape assumption. This operation is essentially an approximate transformation of a complex free boundary problem to a similar one with the consequent introduction of free parameters.

(2) A unique solution of the solute diffusion equation has been obtained by applying all the physical boundary conditions and one additional optimal statement. Here the minimum rate of internal entropy production has been invoked.

The generalized phase transformation, as a free boundary problem, is a variational problem in which the optimization condition is indispensable. The rate of internal entropy production is the only thermodynamic potential function which completely describes the non-equilibrium situation and is a minimum at the steady state of a pure relaxation process.

(3) The variations of the theoretically calculated tip concentration and the tip radius as a function of growth

velocity, for a fixed temperature gradient, are in reasonable agreement with experimental results.

(4) The theoretically predicted and experimentally observed temperature gradient effects on the tip properties and the cell (or dendrite) spacing are in good agreement; with increasing temperature gradient, for a fixed growth velocity, the spacing decreases for any growth velocity and the tip concentration and radius increase in the low velocity regime.

(5) The maximum tip temperature condition (or the minimum tip undercooling condition) is one of the special cases of the condition of the minimum rate of internal entropy production (i.e., when it is applied at a particular point, the dendrite tip).

(6) There exists a significant amount of constitutional supercooling in front of the dendrite tips. In usual experimental conditions, both the minimum tip undercooling condition and the zero constitutional supercooling condition require tip radii less than 1 μm, which is not observed.

(7) The amount of undercooling at the dendrite tip in columnar growth is a necessary starting point for any rigorous theory of microsegregation in directional growth. There is evidence that the controlled solidification experiments [illegible] simulate

These results, therefore, indicate that the departure of the dendrite tip concentration from $k_o c_\infty$ has practical as well as theoretical implications, which must be accounted for in subsequent advances in the theory of microsegregation.

(8) In the Fe-8 wt.% Ni system, diffusional homogenization is minimal while nearly complete homogenization occurs in the Fe-18 wt.% Cr-8 wt.% Ni system for the conditions of the present investigation. This result therefore emphasizes the importance of the $\delta \rightleftarrows \gamma$ transition in the post-solidification homogenization of steels.

APPENDIX I

DIFFERENTIAL VECTOR OPERATIONS IN PARABOLIC COORDINATES (α,β,φ)

In generalized orthogonal curvilinear coordinates (q_1,q_2,q_3),

$$\text{Grad}(\vec{\nabla}) = \sum_i \frac{1}{h_i} \vec{a}_i \frac{\partial}{\partial q_i} , \qquad \text{(A1-1)}$$

where $\vec{a}_i$ is the unit vector and the coefficient, h_i, has the relation with cartesian coordinates (x,y,z)

$$h_i = \left(\frac{\partial x}{\partial q_i}\right)^2 + \left(\frac{\partial y}{\partial q_i}\right)^2 + \left(\frac{\partial z}{\partial q_i}\right)^2 . \qquad \text{(A1-2)}$$

For dimensionless parabolic coordinates (α,β,φ), the transformation relations are

$$x = \rho\alpha\beta \cos\varphi, \qquad \text{(A1-3)}$$

$$y = \rho\alpha\beta \sin\varphi , \qquad \text{(A1-4)}$$

and

$$z = \tfrac{1}{2}\rho(\alpha^2 - \beta^2), \qquad \text{(A1-5)}$$

and h_is have the form

$$h_\alpha = \rho(\alpha^2 + \beta^2)^{\frac{1}{2}} \qquad \text{(A1-6)}$$

$$h_\beta = \rho(\alpha^2 + \beta^2)^{\frac{1}{2}} \qquad \text{(A1-7)}$$

and

$$h_\varphi = \rho\alpha\beta, \qquad \text{(A1-8)}$$

where ρ is the radius of tip curvature.

Thus

$$\vec{\nabla} = \frac{1}{\rho(\alpha^2+\beta^2)^{\frac{1}{2}}}\vec{\alpha}_o\frac{\partial}{\partial\alpha} + \frac{1}{\rho(\alpha^2+\beta^2)^{\frac{1}{2}}}\vec{\beta}_o\frac{\partial}{\partial\beta} + \frac{1}{\rho\alpha\beta}\vec{\varphi}_o\frac{\partial}{\partial\varphi} \qquad \text{(A1-9)}$$

where $\vec{\alpha}_o$, $\vec{\beta}_o$ and $\vec{\varphi}_o$ are unit vectors in parabolic coordinates.

Resolving $\vec{\alpha}_o$, $\vec{\beta}_o$ and $\vec{\varphi}_o$ in cartesian components,

$$\vec{\alpha}_o = \frac{1}{(\alpha^2+\beta^2)^{\frac{1}{2}}}(\vec{i}\beta\cos\varphi + \vec{j}\beta\sin\varphi + \vec{k}\alpha), \qquad \text{(A1-10)}$$

$$\vec{\beta}_o = \frac{1}{(\alpha^2+\beta^2)^{\frac{1}{2}}}(\vec{i}\alpha\cos\varphi + \vec{j}\alpha\sin\varphi - \vec{k}\beta), \qquad \text{(A1-11)}$$

and

$$\vec{\varphi}_o = -\vec{i}\sin\varphi + \vec{j}\cos\varphi, \qquad \text{(A1-12)}$$

where $\vec{i}$, $\vec{j}$ and $\vec{k}$ are cartesian unit vectors.

Substituting Eqs.(A1-10) - (A1-12) into Eq.(A1-9) and equating gradient expressions in cartesian and parabolic coordinates, we obtain

$$\frac{\partial}{\partial x} = \frac{1}{\rho}\left[\frac{1}{\alpha^2+\beta^2}\beta\cos\varphi\frac{\partial}{\partial\alpha} + \frac{1}{\alpha^2+\beta^2}\alpha\cos\varphi\frac{\partial}{\partial\beta} - \frac{1}{\alpha\beta}\sin\varphi\frac{\partial}{\partial\varphi}\right], \qquad \text{(A1-13)}$$

$$\frac{\partial}{\partial y} = \frac{1}{\rho}\left[\frac{1}{\alpha^2+\beta^2}\beta\sin\varphi\frac{\partial}{\partial\alpha} + \frac{1}{\alpha^2+\beta^2}\alpha\sin\varphi\frac{\partial}{\partial\beta} + \frac{1}{\alpha\beta}\cos\varphi\frac{\partial}{\partial\varphi}\right], \qquad \text{(A1-14)}$$

and

$$\frac{\partial}{\partial z} = \frac{1}{\rho}\frac{1}{\alpha^2+\beta^2}\left[\alpha\frac{\partial}{\partial\alpha} - \beta\frac{\partial}{\partial\beta}\right]. \qquad \text{(A1-15)}$$

The Laplacian in general coordinates has the form

$$\nabla^2 = \frac{1}{h_1 h_2 h_3}\left[\frac{\partial}{\partial q_1}\left(\frac{h_2 h_3}{h_1}\frac{\partial}{\partial q_1}\right) + \frac{\partial}{\partial q_2}\left(\frac{h_3 h_1}{h_2}\frac{\partial}{\partial q_2}\right) + \frac{\partial}{\partial q_3}\left(\frac{h_1 h_2}{h_3}\frac{\partial}{\partial q_3}\right)\right]. \quad \text{(A1-16)}$$

In parabolic coordinates, (A1-16) leads to

$$\nabla^2 = \frac{1}{\rho^2}\frac{1}{\alpha^2+\beta^2}\left[\frac{\partial^2}{\partial\alpha^2} + \frac{1}{\alpha}\frac{\partial}{\partial\alpha} + \frac{\partial^2}{\partial\beta^2} + \frac{1}{\beta}\frac{\partial}{\partial\beta}\right] + \frac{1}{\rho^2}\frac{1}{\alpha^2\beta^2}\frac{\partial^2}{\partial\varphi^2}. \quad \text{(A1-17)}$$

APPENDIX II

GENERAL SOLUTION OF THE DIFFUSION EQUATION

A mathematically rigorous general solution of the diffusion equation expressed in parabolic coordinates was obtained by Trivedi[31] and Holzmann[30]. An independent approach to the solution is presented in this appendix to provide a convenience for readers of this thesis and to strengthen confidence in the previous work.

The steady state diffusion equation in parabolic coordinates with rotational symmetry was represented in chapter 3 as

$$\frac{\partial^2}{\partial\alpha^2}+\left(\frac{1}{\alpha}+2p\alpha\right)\frac{\partial u}{\partial\alpha}+\frac{\partial^2 u}{\partial\beta^2}+\left(\frac{1}{\beta}-2p\beta\right)\frac{\partial u}{\partial\beta}=0. \qquad \text{(A2-1)}$$

Introducing new variables α_1 and β_1 related to α and β by

$$\left.\begin{aligned}\alpha_1 &= -p\alpha^2\\ \beta_1 &= p\beta^2\end{aligned}\right\}, \qquad \text{(A2-2)}$$

Eq.(A2-1) takes the form

$$\alpha_1\frac{\partial^2 u}{\partial\alpha_1^2}+(1-\alpha_1)\frac{\partial u}{\partial\alpha_1}-\beta_1\frac{\partial^2 u}{\partial\beta_1^2}-(1-\beta_1)\frac{\partial u}{\partial\beta_1}=0. \qquad \text{(A2-3)}$$

If we assume that u can be written in the form

$$u = A(\alpha_1)\cdot B(\beta_1), \qquad \text{(A2-4)}$$

then, Eq. (A2-3) has the form

$$\frac{1}{A}\left[\alpha_1\frac{d^2A}{d\alpha_1^2} + (1-\alpha_1)\frac{dA}{d\alpha_1}\right] - \frac{1}{B}\left[\beta_1\frac{d^2B}{d\beta_1^2} + (1-\beta_1)\frac{dB}{d\beta_1}\right] = 0. \quad \text{(A2-5)}$$

To have the solution at all, each term on the left of Eq. (A2-5) must be equal to a constant, say λ. Then we obtain two ordinary differential equations.

$$\alpha_1\frac{d^2A}{d\alpha_1^2} + (1-\alpha_1)\frac{dA}{d\alpha_1} - \lambda A = 0, \quad \text{(A2-6)}$$

and

$$\beta_1\frac{d^2B}{d\beta_1^2} + (1-\beta_1)\frac{dB}{d\beta_1} - \lambda B = 0. \quad \text{(A2-7)}$$

Eqs. (A2-6) and (A2-7) are of special form of the confluent hypergeometric equation. The general form of the confluent hypergeometric equation is

$$x\frac{d^2y}{dx^2} + (b-x)\frac{dy}{dx} - ay = 0. \quad \text{(A2-8)}$$

Using the method of Frobenius, we obtain two independent solutions

$$y_1 = M(a,b,x) = \sum_{n=0}^{\infty}\frac{(a)_n x^n}{(b)_n\, n!}, \quad \text{(A2-9)}$$

$$(b \neq 0, -1, -2, \ldots.),$$

and

$$y_2 = x^{1-b}\,M(1+a-b,2-b,x), \quad \text{(A2-10)}$$

$$(b \neq 0, \pm 1, \pm 2, \ldots).$$

Further solutions are obtained by variable transformation of the differential equation

$$y_3 = e^x M(b-a,\ b,\ -x), \tag{A2-11}$$

and $$y_4 = x^{1-b}e^x M(1-a,\ 2-b,\ -x). \tag{A2-12}$$

Second forms of solutions may be deduced by linear combinations

$$y_5 = U(a,b,x) = \frac{\Gamma(1-b)}{\Gamma(1+a-b)}\, y_1 + \frac{\Gamma(b-1)}{\Gamma(a)}\, y_2, \tag{A2-13}$$

$$y_6 = x^{1-b}U(1+a-b,\ 2-b,\ x), \tag{A2-14}$$

$$y_7 = e^x U(b-a,\ b,\ -x) \tag{A2-15}$$

and $$y_8 = e^x x^{1-b} U(1-a,\ 2-b,\ -x). \tag{A2-16}$$

When b=1, the Frobenius method gives only one solution. Another linearly independent solution for this case is the logarithmic solution

$$(y_2)_{b=1} = y_1 \ln x + \frac{ax}{(1!)^2}\left(\frac{1}{a} - \frac{2}{1}\right) + \cdots$$

$$+ \frac{(a)_r x^r}{(r!)^2}\left(\frac{1}{a} + \frac{1}{a+1} + \cdots + \frac{1}{a+r-1} - \frac{2}{1} - \cdots - \frac{2}{r}\right) + \cdots, \tag{A2-17}$$

$$(a \neq 0,\ -1,\ -2,\ \ldots).$$

The corresponding solutions for y_5 and y_7 follow directly from the definition of these functions

$$(y_5)_{b=1} = U(a,\ 1,\ x)$$

$$= \frac{1}{\Gamma(a)}\left[M(a,1,x)\ln x + \sum_{r=0}^{\infty} \frac{(a)_r x^r}{(r!)^2}\left\{\psi(a+r) - 2\psi(1+r)\right\}\right], \tag{A2-18}$$

where $\psi(x)$ is the Psi function defined by

$$\psi(x) = \frac{\Gamma'(x)}{\Gamma(x)} , \tag{A2-19}$$

and $$(y_7)_{b=1} = e^x\, U(1-a,\ 1,\ -x). \tag{A2-20}$$

The general solution of Eq. (A2-8) may be any linear combination of the solutions under the condition that their Wronskian does not vanish, in general

$$y = C_1\, M(a,b,x) + C_2 U(a,b,x). \tag{A2-21}$$

We shall consider now our differential equations (A2-6) and (A2-7). The parameter b=1 and the other parameter a can be defined imposing the boundary condition at infinity to Eq. (A2-7). Our boundary condition at infinity implies that B is finite when $\beta_1 \to \infty$ ($\beta \to \infty$) for any value of α except for $\alpha=1$. The asymptotic expansion of M(a,1,x) for large x is

$$M(a,1,x) = \frac{1}{\Gamma(a)}\, e^x\, x^{a-1} \left\{ 1 + O|x|^{-1} \right\}. \tag{A2-22}$$

The condition for a finite M(a,1,x) with $x \to \infty$ is

$$a = 0,\ -1,\ -2,\ \ldots\ . \tag{A2-23}$$

Examining the Wronskians of y_i and y_j under the conditions of b=1 and a=-n (integral n), we find that y_1 and y_7 are independent solutions. Thus the general solution of Eq. (A2-7) is

$$B = C_1 M(-n,1,\beta_1) + C_2 e^{\beta_1} U(1+n,1,-\beta_1). \tag{A2-24}$$

When $\beta_1 \to \infty$, the second term becomes infinity, therefore C_2 must be zero.

Using the identity

$$M(-n,1,x) = L_n(x), \tag{A2-25}$$

the general solution of Eq. (A2-7) is

$$B_n = C_{1n}L_n(p\beta^2). \tag{A2-26}$$

Similarly, the general solution of Eq. (A2-6) may be given by

$$A = C_3M(-n,1,\alpha_1) + C_4e^{\alpha_1}\,U(1+n,1,-\alpha_1). \tag{A2-27}$$

When $\alpha\to\infty$ ($\alpha_1\to-\infty$), $M(-n,1,\alpha_1)$ becomes infinity. To satisfy the boundary condition u=0 when $\alpha\to\infty$, C_3 must be zero. Thus

$$A_n = C_{4n}e^{-p\alpha^2}\,U(1+n,\ 1,\ p\alpha^2). \tag{A2-28}$$

Without loss of generality, we choose the coefficient C_{4n} such that $A_n = 1$ with $\alpha=1$. Then

$$A_n = \frac{e^{-p\alpha^2}U(n+1,1,p\alpha^2)}{e^{-p}U(n+1,1,p)} \tag{A2-29}$$

From Eqs. (A2-4), (A2-26) and (A2-29), we finally obtain

$$\psi(\alpha,\beta) = \sum_{n=0}^{\infty} E_n \frac{e^{-p\alpha^2}U(n+1,1,p\alpha^2)}{e^{-p}U(n+1,1,p)}\,L_n(p\beta^2). \tag{A2-30}$$

APPENDIX III

SOME INTEGRALS

In this appendix, some integrals encountered in chapter 3 are evaluated.

(1) Evaluate the integral

$$I_1 = \int_0^\infty e^{-x}\, x^\nu L_n(x)\, dx. \tag{A3-1}$$

By definition, Laguerre polynomials have the form

$$L_n^{(\alpha)}(x) = e^x \frac{x^{-\alpha}}{n!} \frac{d^n}{dx^n} (e^{-x}\, x^{n+\alpha}),\ n=0,1,2,\cdots. \tag{A3-2}$$

Substituting Eq. (A3-2) into Eq. (A3-1)

$$I_1 = \frac{1}{n!} \int_0^\infty x^\nu \frac{d^n}{dx^n} (e^{-x}\, x^n)\, dx.$$

Integrating by parts n times

$$I_1 = \frac{1}{n!} (-1)^n \nu(\nu-1)(\nu-2)\cdots(\nu-n+1) \int_0^\infty e^{-x}\, x^\nu dx. \tag{A3-4}$$

Using the identity

$$\Gamma(x) = \int_0^\infty e^{-t}\, t^{x-1}\, dt, \tag{A3-5}$$

we finally obtain

$$I_1 = (-1)^n \frac{[\Gamma(\nu+1)]^2}{\Gamma(n+1)\Gamma(\nu-n+1)}. \tag{A3-6}$$

(2) Evaluate the integral

$$I_2 = \int_0^\infty (p+\xi)^{-\frac{1}{2}} e^{-\xi} L_n(\xi)\, d\xi. \qquad \text{(A3-7)}$$

The integral representation of Laguerre polynomials has the form

$$L_n(\xi) = \frac{e^{\xi}}{n!} \int_0^\infty t^n J_0(2\sqrt{\xi t})\, e^{-t}\, dt. \qquad \text{(A3-8)}$$

Substituting Eq.(A3-8) into Eq.(A3-7) and putting $\xi = x^2$

$$I_2 = \frac{1}{n!} \int_0^\infty t^n e^{-t} dt \int_0^\infty \frac{2x}{\{(\sqrt{p})^2+x^2\}^{\frac{1}{2}}} J_0(2\sqrt{t}\, x)\, dx. \qquad \text{(A3-9)}$$

Using the identity

$$\int_0^\infty e^{-pt}\, t^{z-1}\, dt = \frac{\Gamma(z)}{p^z} \qquad \text{(A3-10)}$$

we find the relation

$$\frac{1}{\{(\sqrt{p})^2+x^2\}^{\frac{1}{2}}} = \frac{1}{\Gamma(\frac{1}{2})} \int_0^\infty e^{-\{(\sqrt{p})^2+x^2\}s}\, s^{-\frac{1}{2}}\, ds. \qquad \text{(A3-11)}$$

Hence

$$I_2 = \frac{2}{n!}\, \frac{1}{\sqrt{\pi}} \int_0^\infty t^n e^{-t}\, dt \int_0^\infty e^{-(\sqrt{p})^2 s}\, s^{-\frac{1}{2}}\, ds \int_0^\infty e^{-sx^2}\, x\, J_0(2\sqrt{t}\, x)\, dx. \qquad \text{(A3-12)}$$

The last integral is a special form of the Weber's integral whose general form is

$$\int_0^\infty e^{-a^2x^2}\, J_\nu(bx) x^{\nu+1}\, dx = \frac{b^\nu}{(2a^2)^{\nu+1}}\, e^{-\frac{b^2}{4a^2}}. \qquad \text{(A3-13)}$$

Thus

$$\int_0^\infty e^{-sx^2} \; x \; J_0(2\sqrt{t}\; x)\; dx = \frac{1}{2s}\, e^{-\frac{t}{s}} \; . \qquad \text{(A3-14)}$$

Substituting Eq.(A3-14) into Eq.(A3-12)

$$I_2 = \frac{1}{n!}\,\frac{2}{\sqrt{\pi}} \int_0^\infty t^n\, e^{-t}\, dt\, \tfrac{1}{2} \int_0^\infty e^{-(\sqrt{p})^2 s - \frac{t}{s}}\, s^{-\frac{3}{2}}\, ds \; . \qquad \text{(A3-15)}$$

Putting $ps = u$,

$$I_2 = \frac{2}{n!}\,\frac{\sqrt{p}}{\sqrt{\pi}} \int_0^\infty t^n\, e^{-t}\, dt\, \tfrac{1}{2} \int_0^\infty e^{-u-\frac{pt}{u}}\, u^{-\frac{3}{2}}\, du \qquad \text{(A3-16)}$$

Representing the last integral by the modified Bessel function of the third kind (Macdonald's function) whose integral representation is given by

$$K_\nu(z) = \tfrac{1}{2}\left(\frac{z}{2}\right)^\nu \int_0^\infty e^{-t-\frac{z^2}{4t}}\, t^{-\nu-1}\, dt \; , \qquad \text{(A3-17)}$$

I_2 has the form

$$I_2 = \frac{2}{n!} \int_0^\infty t^n\, e^{-t}\, \frac{(\sqrt{p})^{\frac{1}{2}}}{\sqrt{\pi}}\, (\sqrt{t})^{-\frac{1}{2}}\, K_{\frac{1}{2}}(2\sqrt{pt})\, dt. \qquad \text{(A3-18)}$$

The table of cylinder functions of half integral order gives

$$K_{\frac{1}{2}}(x) = \left(\frac{\pi}{2x}\right)^{\frac{1}{2}} e^{-x} \; . \qquad \text{(A3-19)}$$

From Eqs.(A3-18) and (A3-19),

$$I_2 = \frac{1}{n!} \int_0^\infty t^{n-\frac{1}{2}}\, e^{-t-2\sqrt{pt}}\, dt \; . \qquad \text{(A3-20)}$$

Putting $t = (q-\sqrt{p})^2$,

$$I_2 = \frac{(2n)!}{n!}\ \frac{2}{(2n)!}\ e^p \int_{\sqrt{p}}^{\infty} (q-\sqrt{p})^{2n}\ e^{-q2}\ dq. \qquad \text{(A3-21)}$$

This integral has the form of the repeated integrals of the error function defined by

$$\{1\}^n\ \mathrm{erfc}(x) = \frac{1}{\sqrt{\pi}}\ \frac{2}{n!} \int_x^{\infty} (t-x)^n\ e^{-t^2}\ dt. \qquad \text{(A3-22)}$$

Thus,

$$I_2 = \frac{(2n)!}{n!}\ e^p \sqrt{\pi}\ \{1\}^{2n}\ \mathrm{erfc}(\sqrt{p}). \qquad \text{(A3-23)}$$

Using the definition of the normalized integral error function

$$I_m \mathrm{erfc}\ x = 2^m \Gamma(1+\tfrac{m}{2}) \{1\}^m\ \mathrm{erfc}(x), \qquad \text{(A3-24)}$$

we finally obtain

$$I_2 = e^p\ \frac{\Gamma(n+\frac{1}{2})}{\Gamma(n+1)}\ I_{2n}\ \mathrm{erfc}(\sqrt{p}). \qquad \text{(A3-25)}$$

(3) Evaluate the integral

$$I_3 = \int_0^{\infty} e^{-\xi}\ (p+\xi)^{-\frac{3}{2}}\ L_n(\xi)\ d\xi. \qquad \text{(A3-26)}$$

This integral can be straightforwardly evaluated by differentiating I_2 with respect to p.

$$\frac{\partial}{\partial p}\left[\int_0^{\infty} e^{-\xi}(p+\xi)^{-\frac{1}{2}}\ L_n(\xi)\,d\xi\right] = -\tfrac{1}{2}\int_0^{\infty} e^{-\xi}(p+\xi)^{-\frac{3}{2}}\ L_n(\xi)\ d\xi. \qquad \text{(A3-27)}$$

Hence,

$$I_3 = -2\,\frac{\partial}{\partial p}\,(I_2). \qquad \text{(A3-28)}$$

It follows from the definition of the function $I_n\text{erfc}(x)$ that

$$\frac{d}{dx} I_n\text{erfc}(x) = (-1) \frac{A_n}{A_{n-1}} I_{n-1}\text{erfc}(x), \qquad \text{(A3-29)}$$

where $A_n = 2^n \Gamma(1 + \frac{n}{2})$. (A3-30)

Then

$$\frac{\partial}{\partial p}\left[e^p \frac{\Gamma(n+\frac{1}{2})}{\Gamma(n+1)} I_{2n} \text{erfc}(\sqrt{p}) \right]$$

$$= \frac{\Gamma(n+\frac{1}{2})}{\Gamma(n+1)} \left[e^p I_{2n} \text{erfc}(\sqrt{p}) - e^p \frac{1}{\sqrt{p}} \frac{\Gamma(n+1)}{\Gamma(n+\frac{1}{2})} I_{2n-1} \text{erfc}(\sqrt{p}) \right]. \qquad \text{(A3-31)}$$

From Eqs. (A3-28) and (A3-31), it follows

$$I_3 = 2e^p \left[\frac{1}{\sqrt{p}} I_{2n-1} \text{erfc}(\sqrt{p}) - \frac{\Gamma(n+\frac{1}{2})}{\Gamma(n+1)} I_{2n} \text{erfc}(\sqrt{p}) \right]. \qquad \text{(A3-32)}$$

Using the recurrence relation of the normalized integral error function, we obtain

$$\sqrt{p}\, I_3 = 2e^p I_{2n+1} \text{erfc}(\sqrt{p}). \qquad \text{(A3-33)}$$

REFERENCES

1. W. A. Tiller, K. A. Jackson, J. W. Rutter and B. Chalmers, Acta Met. 1, 428 (1953)
2. W. W. Mullins and R. F. Sekerka, J. Appl. Phys., 34, 323 (1963)
3. W. W. Mullins and R. F. Sekerka, J. Appl. Phys., 35, 444 (1964)
4. L. A. Tarshis and W. A. Tiller, in Crystal Growth, Proceedings of an International Conference on Crystal Growth, Boston, 20-24 June 1966, Pergamon Press, N.Y. (1967)
5. P. G. Shewmon, Trans. Met. Soc. AIME, 233, 736 (1965)
6. J. W. Cahn, in Crystal Growth, Proceedings of an International Conference on Crystal Growth, Boston, 20-24 June 1966, Pergamon Press, N.Y. (1967)
7. D. E. Coates, S. V. Subramanian and G. R. Purdy, Trans. Met. Soc. AIME, 242, 800 (1968)
8. R. F. Sekerka, J. Crystal Growth, 3, 4, 71 (1968)
9. D. J. Wollkind and L. A. Segel, Phil. Trans. Roy. Soc. London, 268A, 33 (1970)
10. G. F. Bolling and W. A. Tiller, J. Appl. Phys., 31, 2040 (1960)
11. J. J. Krammer, G. F. Bolling and W. A. Tiller, Trans. Met. Soc. AIME, 227, 374 (1963)

12. L. F. Donaghey and W. A. Tiller, in The Solidification of Metals, Proceedings of the Conference on the Solidification of Metals, Brighton, 4-7 December 1967, The Iron and Steel Institute, London (1968)

13. B. Chalmers, Principles of Solidification, John Wiley & Sons Inc., New York (1964)

14. T. Z. Kattamis and M. C. Flemings, Trans. Met. Soc. AIME, 233, 992 (1965)

15. H. D. Brody and M. C. Flemings, Trans. Met. Soc. AIME, 236, 615 (1966)

16. T. F. Bower, H. D. Brody, and M. C. Flemings, Trans. Met. Soc. AIME, 236, 624 (1966)

17. M. C. Flemings, D. R. Poirier, R. V. Barone and H. D. Brody, JISI, 208, 371 (1970)

18. F. Weinberg and R. K. Buhr, in The Solidification of Metals, Brighton, 4-7 December 1967, The Iron and Steel Institute, London (1968)

19. F. Weinberg and E. Teghtsoonian, Met. Trans. AIME, 3, 93 (1972)

20. R. M. Sharp and A. Hellawell, J. Crystal Growth, 6, 253 (1970)

21. R. M. Sharp and A. Hellawell, J. Crystal Growth, 6, 334 (1970)

22. K. A. Jackson and J. D. Hunt, Acta Met., 13, 1212 (1965)

23. K. A. Jackson, J. D. Hunt, D. R. Uhlmann and T. P. Seward III, Trans. Met. Soc. AIME, 236, 149 (1966)

24. G. P. Ivantsov, Dokl. Akad. Nauk SSSR, 58, 567 (1947)

25. G. Horvay and J. W. Cahn, Acta Met., 9, 695 (1961)

26. D. E. Temkin, Dokl. Akad. Nauk. SSSR, 132, 1307 (1960)

27. G. F. Bolling and W. A. Tiller, J. Appl. Phys. 32, 2587 (1961)

28. C. Zener, Trans. AIME, 167, 550 (1946)

29. G. R. Kotler and L. A. Tarshis, J. Crystal Growth, 5, 90 (1969)

30. E. G. Holzmann, J. Appl. Phys., 41, 1460 (1970)

31. R. Trivedi, Acta Met., 18, 287 (1970)

32. W. B. Hillig, J. Crystal Growth, 3,4, 611 (1968)

33. M. E. Glicksman and R. J. Schaefer, Acta Met., 14, 1126 (1966)

34. A. Rosenberg and W. C. Winegard, Acta Met., 2, 342 (1954)

35. M. E. Glicksman and R. J. Schaefer, J. Crystal Growth, 1, 297 (1967)

36. L. Bäckerud and B. Chalmers, Trans. Met. Soc. AIME, 245, 309 (1969)

37. R. D. Doherty and A. Feest, in The Solidification of Metals, Proceedings of the Conference on the Solidification of Metals, Brighton, 4-7 December 1967, The Iron and Steel Institute, London, (1968)

38. H. B. Callen, Thermodynamics, John Wiley & Sons Inc., New York (1960)

39. P. R. Garabedian, Partial Differential Equations, John Wiley & Sons, Inc., New York (1964)

40. I. Stakgold, Boundary Value Problems of Mathematical Physics, Vol. II, The Macmillan Co., New York (1968)

41. G. R. Kotler and W. A. Tiller, J. Crystal Growth, 2, 287, (1968)

42. N. N. Lebedev, Special Functions and Their Applications, Prentice-Hall Inc., Englewood Cliffs, N.J. (1965)

43. L. J. Slater, Confluent Hypergeometric Functions, Cambridge University Press, London (1960)

44. P. J. Davis, Gamma Function and Related Functions, in Handbook of Mathematical Functions, edited by M. Abramowitz and I. A. Stegun, Dover Publications Inc.,

45. G. Arfken, Mathematical Methods for Physicists, Second Edition, Academic Press, Inc., New York (1970)

46. W. Magnus, F. Oberhettinger and R. F. Soni, Formulas and Theorems for the Special Functions of Mathematical Physics, Springer-Verlag Inc., New York (1966)

47. O. S. Berlyand, R. I. Garvrilova and A. P. Prudnikov, Tables of Integral Error Functions and Hermite Polynomials, Pergamon Press Ltd., Oxford (1962)

48. I. Prigogine, Introduction to Thermodynamics of Irreversible Processes, Charles C. Thomas, Publisher, Springfield, Illinois (1955)

49. S. R. DeGroot, Thermodynamics of Irreversible Processes, North Holland Publishing Co., Amsterdam (1952)

50. J. S. Kirkaldy, Can. J. Phys. 37, 739 (1959)

51. J. S. Kirkaldy, Can. J. Phys. 38, 1343 (1960)

52. J. S. Kirkaldy, Energetics in Metallurgical Phenomena, Vol. IV, Gordon and Breach Science Publishers, New York (1968)

53. R. J. Schaefer and M. E. Glicksman, Acta Met., 16, 1009 (1968)

54. M. Hansen, Constitution of Binary Alloys, McGraw-Hill, New York, (1958)

55. G. R. Zellars, S. L. Payne, J. P. Morris and R. L. Kipp, Trans. Met. Soc. AIME, 215, 181 (1959)

56. R. A.Oriani, Acta Met., 1, 448 (1953)

57. United States Steel, The Making, Shaping and Treating of Steel, Eighth Edition (1964)

58. M. R. Hone, Ph.D. Thesis, McMaster University (1970)

59. G. A. Chadwick, in Interfaces, Proceedings of the International Conference, Melbourne, August 1969, Butterworths (1969)

60. L. S. Darken, R. W. Gurry, Physical Chemistry of Metals, McGraw-Hill Book Company Inc., New York (1953)

61. G. R. Purdy and S. V. Subramanian, Unpublished work.

62. Y. S. Touloukian, R. W. Powell, C. Y. Ho and P. G. Klemens, Thermophysical Properties of Matter, Vol. I, Thermal Conductivity, Metallic Elements and Alloys, IFI/Plenum Data Corporation, New York (1970)

63. R. E. Jesse and H.F.J.I. Giller, J. Crystal Growth, 7, 384 (1970)

64. G. L. Kehl, The Principles of Metallographic Laboratory Practice, 3rd Ed., McGraw-Hill, New York (1949)

65. H. Schumann, Metallographie, 4th Ed., VEB Deutscher Verlag für Grundstoffindustrie, Leipzig (1962)

66. L. Habraken and J. L. DeBrouwer, De Ferri Metallographia Vol. 1, Presses Académiques Européenes, Bruxelles (1966)

67. P. Oberhoffer, Stahl und Eisen, 36, 798 (1916)

68. H. Klemm, Neue Hütte, 2, 44 (1957)

69. S. V. Subramanian, C. W. Haworth and D. H. Kirkwood, JISI, 206, 1027 (1968)

70. C. W. Haworth, Summer School in Electron Microscopy and Microprobe Analysis, McMaster University (1968)

71. P. Duncumb and S.J.B. Reed, Nat. Bur. Stand. (U.S.) Spec. Publ. No. 298, p.133 (1968)

72. J. Philibert, X-Ray Optics and X-Ray Microanalysis, Proc. Third Int. Symp. Stanford (1962)

73. M. Green and V. E. Cosslett, Proc. Phys. Soc. (London), 78, 1206 (1961)

74. G. R. Purdy and J. S. Kirkaldy, Met. Trans. AIME, 2, 371 (1971)

75. J. Crank, The Mathematics of Diffusion, Oxford University Press, London (1956)

76. K. Hirano, M. Cohen and B. L. Averbach, Acta Met., 9, 440 (1961)

77. W. A. Tiller, Can. J. Phys. 37, 1204 (1959)

78. ASM Handbook Committee, Metals Handbook, Vol. 1, Eighth Ed., American Society for Metals, Metals Park (1961)

TABLE 1

Chemical Analysis of Pure Fe and Ni

Fe (Ferrovac E)		Ni (Electrolytic Ni)	
Impurities	wt.%	Impurities	wt.%
C	0.003	C	0.0056
Si	<0.006	Si	<0.0006
Mn	0.001	Fe	0.0002
P	0.003	Co	0.0012
S	0.005	Cu	0.0002
Cu	<0.001	Cd	<0.0005
Ni	<0.014	Al	<0.0003
Cr	<0.01	Bi	<0.0005
V	<0.004	B	<0.0005
Mo	<0.001	Pb	<0.0004
W	0.01	Ta	<0.005
Co	0.01	W	<0.005
O_2	0.00046	Zr	<0.0017
H_2	0.00005	H_2	0.00028
N_2	0.0002	N_2	0.0004
		O_2	0.00213

TABLE 2

New improved etching Reagents

(1) Etching Reagent for Fe-Ni alloys (1~15 wt.% Ni)

Composition	Remarks
Ferric chlpride ($FeCl_3 \cdot 6H_2O$):30g Cupric chloride($CuCl_2 \cdot 2H_2O$):8g Stannous chloride ($SnCl_2 \cdot 2H_2O$):4g Hychochloric acid (s.g.1.19):36cc Distilled water:500 cc Ethanol:500cc	Iron rich areas become darker color. Etching time is about 5-10 seconds

(2) Etching reagent for Fe-18% Cr - 8% Ni alloy

Composition	Remarks
Stock Solution: Sodium thiosulfate ($Na_2S_2O_3 \cdot 5H_2O$):150g Distilled water:500cc	7cc of HCl is added to 50cc of stock solution before use. Etching time is 3-8 seconds. This reagent remains active only for about 20 seconds.
Hydrochloric acid(s.g.1.19).	

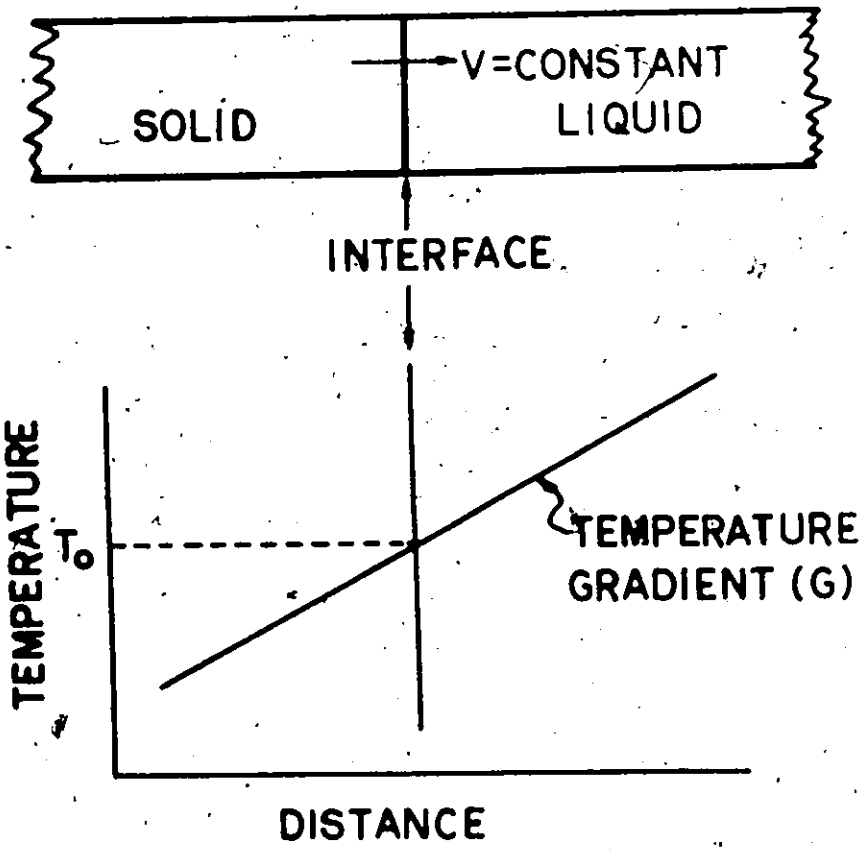

Fig. 1

Unidirectional solidification with a constant velocity and a constant temperature gradient.

REAL GROWTH FRONT
(Array of Dendrites)

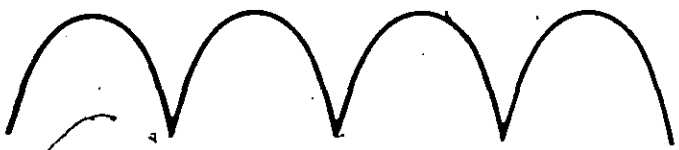

Shape: Unknown

Position: Unknown

PRESENT MODEL
(Single Dendrite)

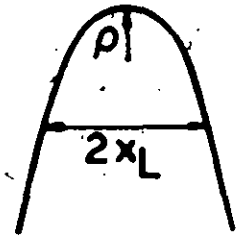

Shape: Partially Constrained
(Paraboloid of Revolution
ρ: Unknown
x_L: Unknown)

Position: Unknown

Fig. 2

Formulation of the present model.

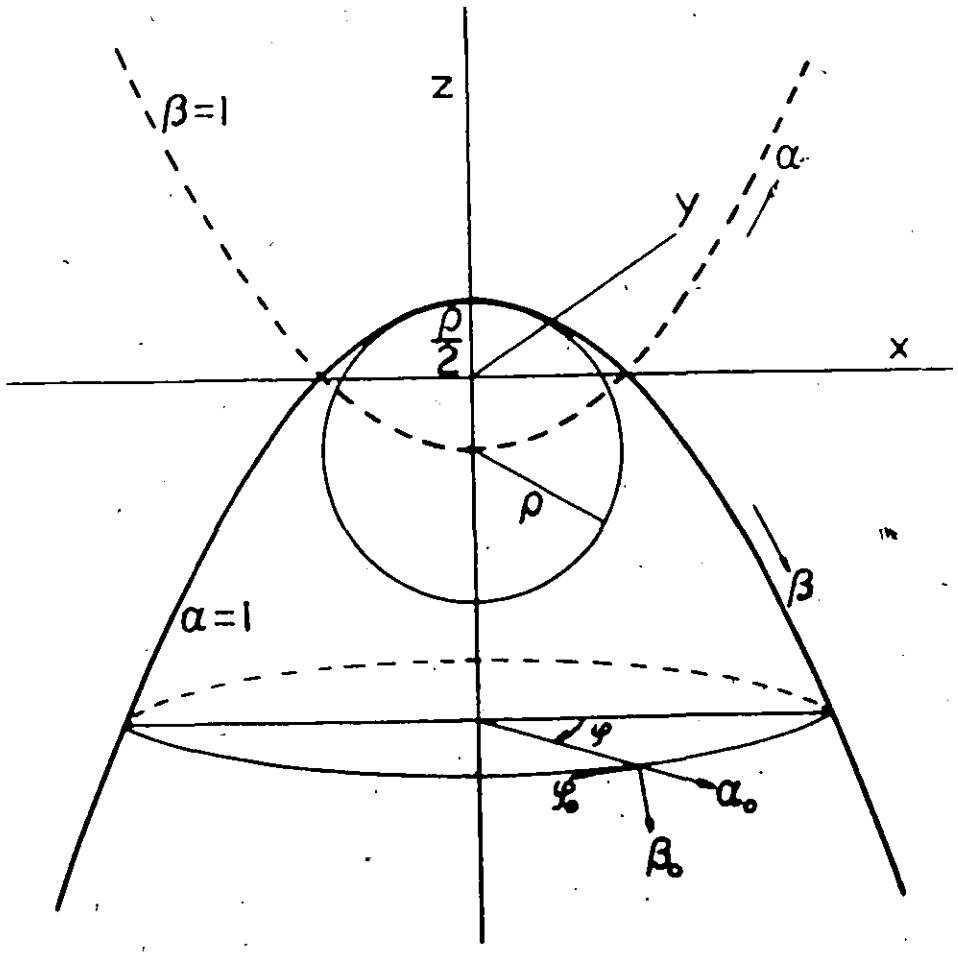

Fig. 3

Relation between parabolic (α,β,φ) and cartesian (x,y,z) coordinates.

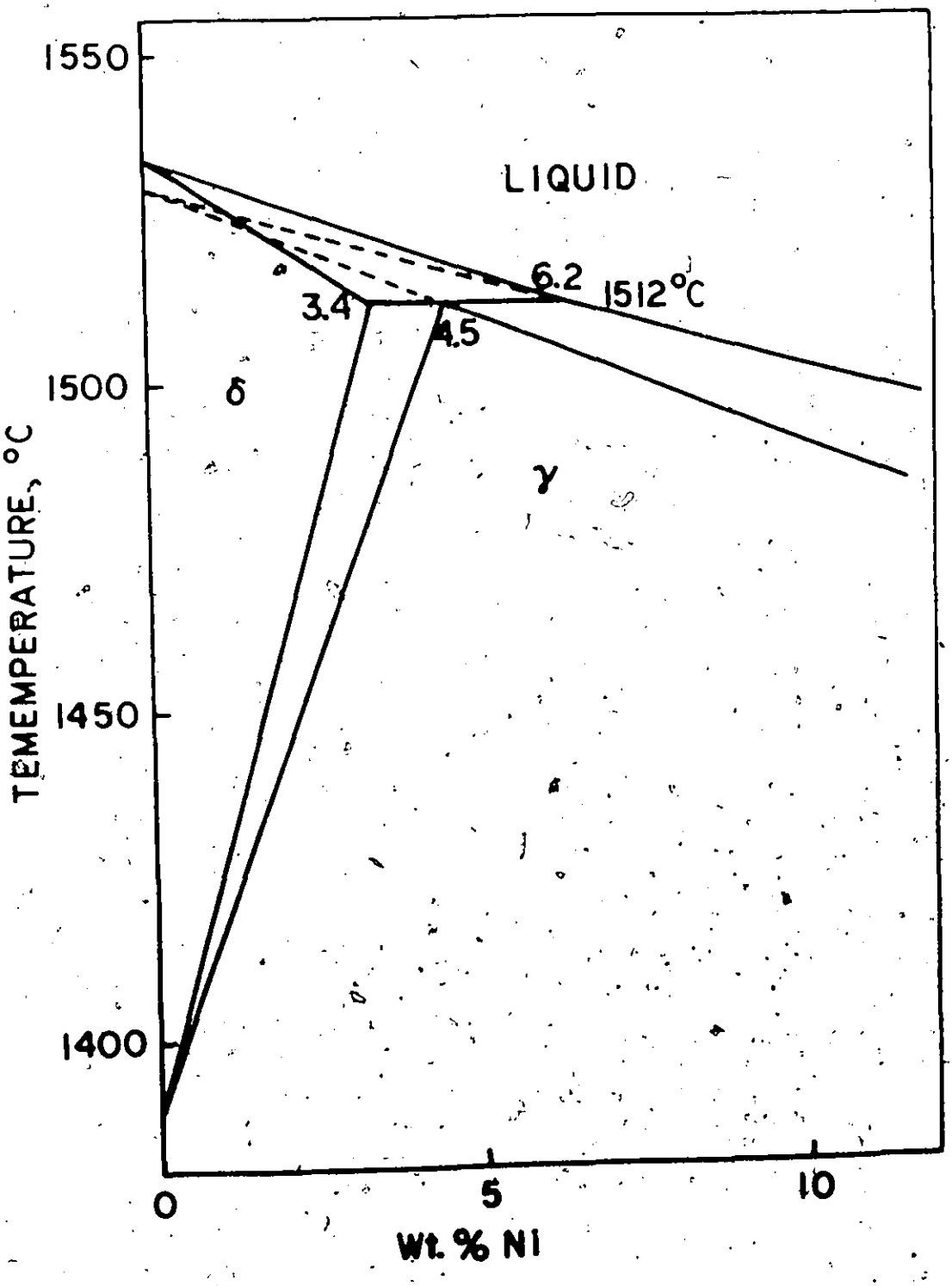

Fig. 4 Iron-Nickel phase diagram (after Hansen).

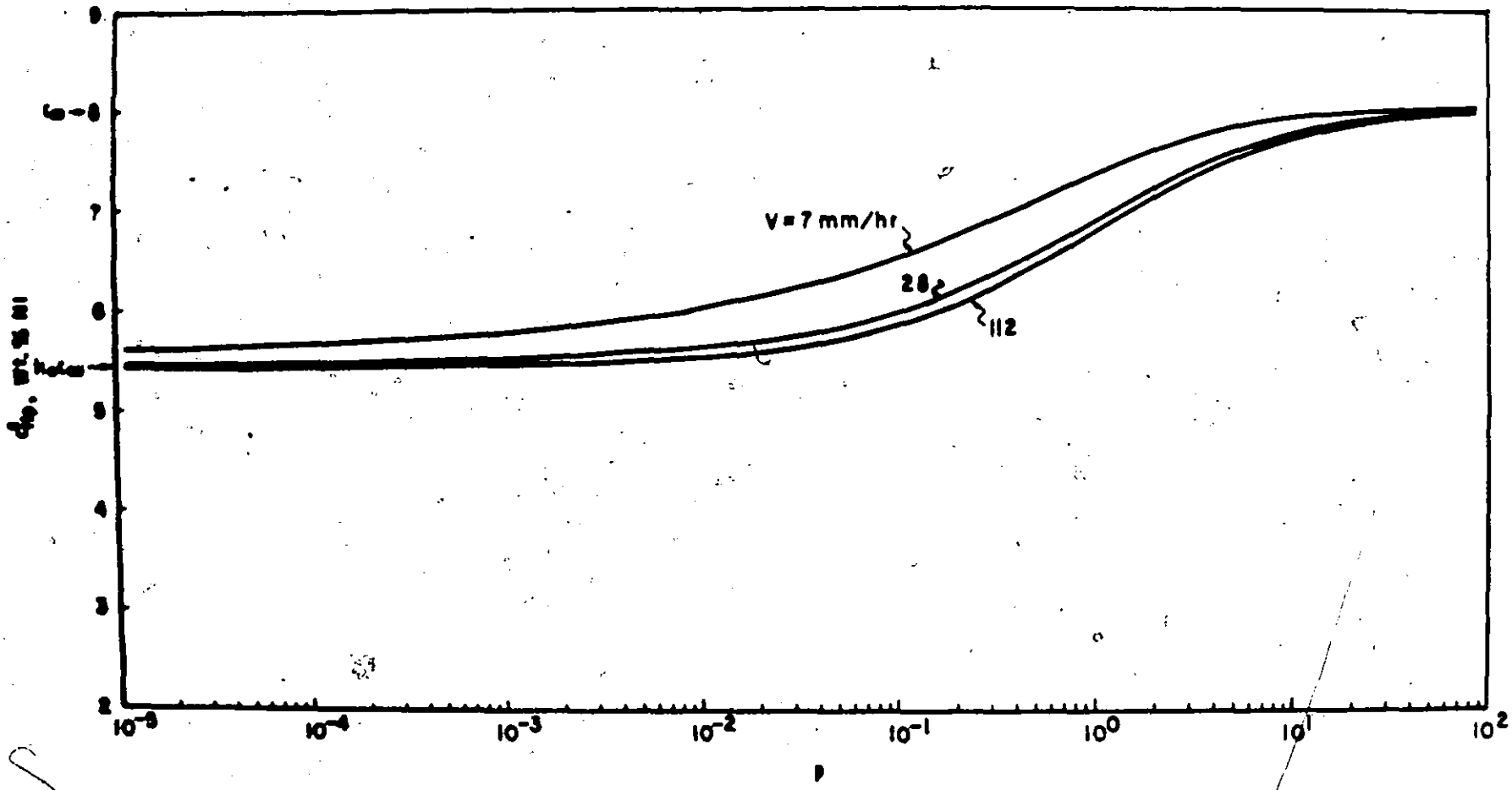

Fig. 5 Tip concentration as a function of p and v (Fe-8 wt.% Ni, G = 31°C/cm, Gibbs-Thomson and kinetic effects are neglected).

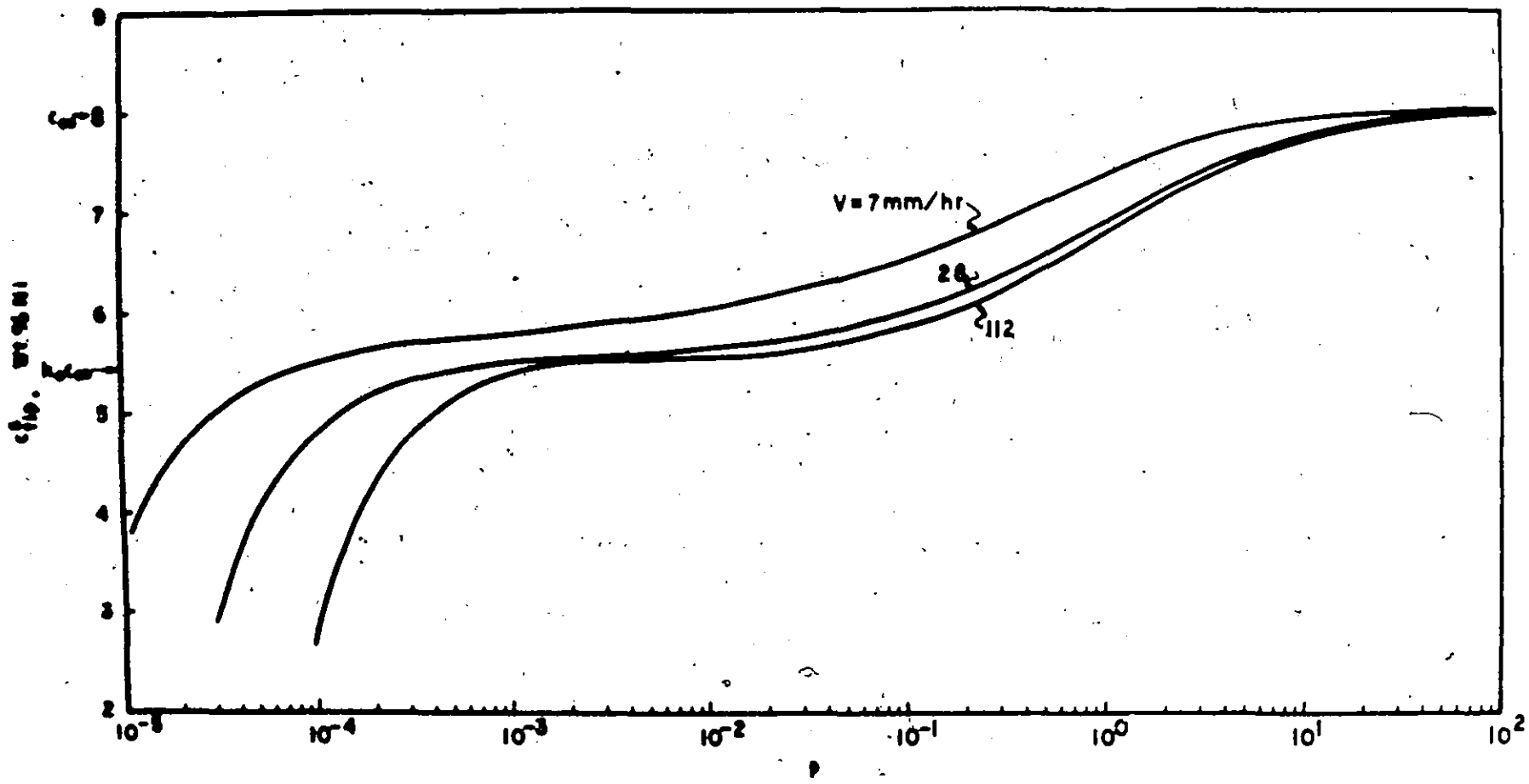

Fig. 6 Tip concentration as a function of p and v (Fe-8 wt.% Ni, G = 31°C/cm, Gibbs-Thomson and kinetic effects are considered).

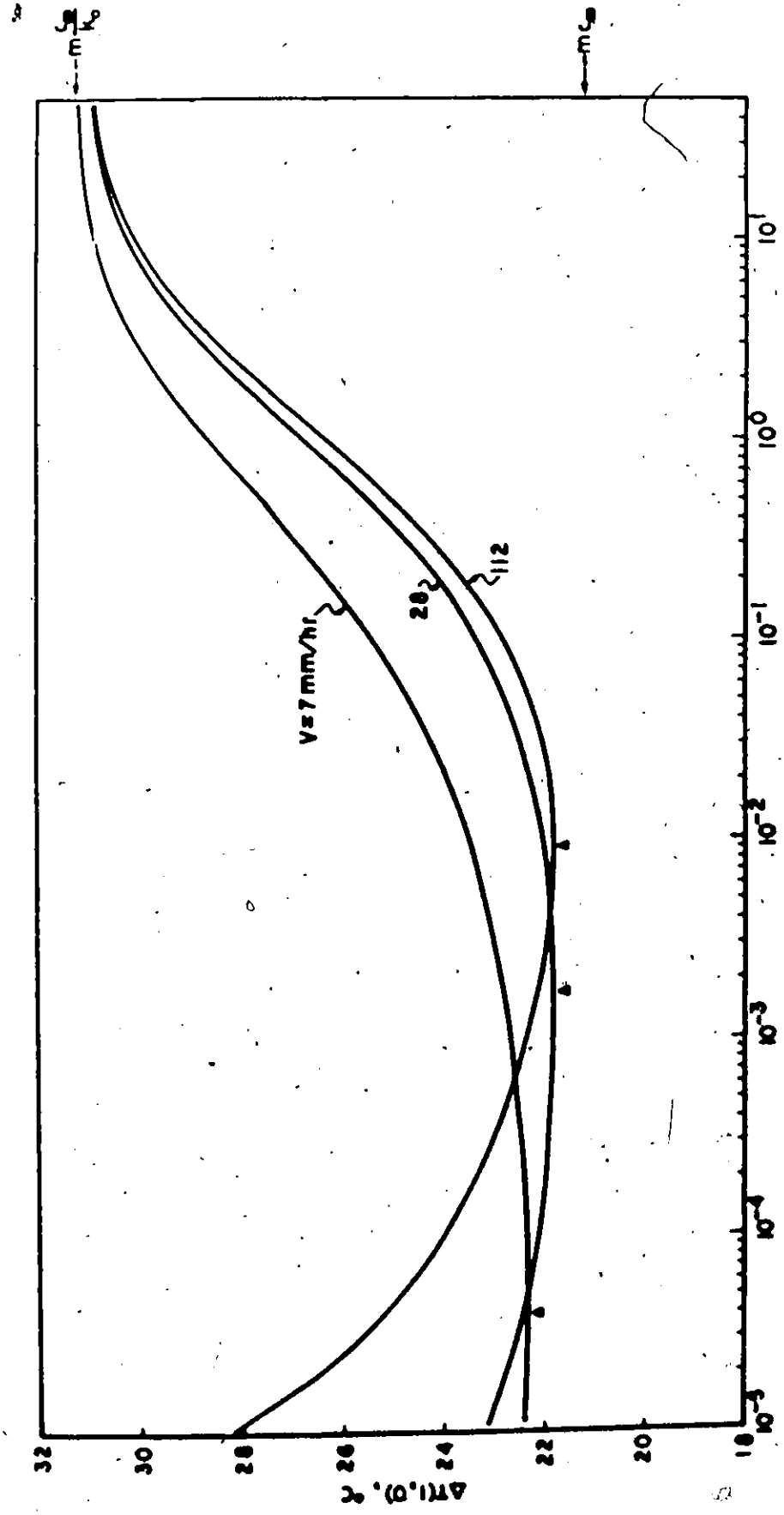

Fig. 7 Tip undercooling, ΔT, as a function of p and v (Fe-8 wt.% Ni, G = 31°C/cm).

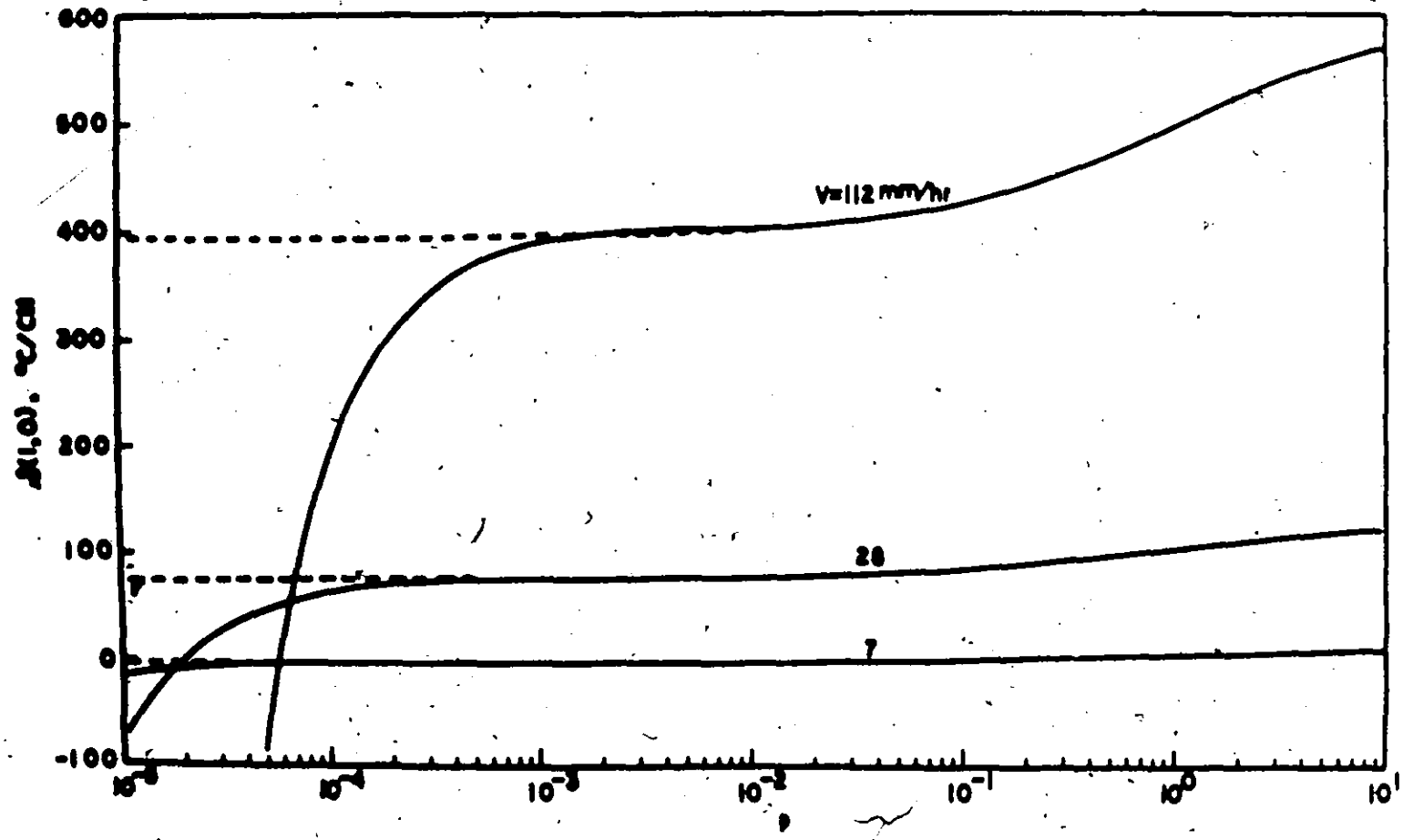

Fig. 8 Constitutional supercooling in front of the tip, $\Delta T(1,0)$, as a function of p and v (Fe-8 wt.% Ni, $G = 31^{\circ}C/cm$). Dashed curves represent $\Delta T(1,0)$ calculated by neglecting Gibbs-Thomson and kinetic effects.

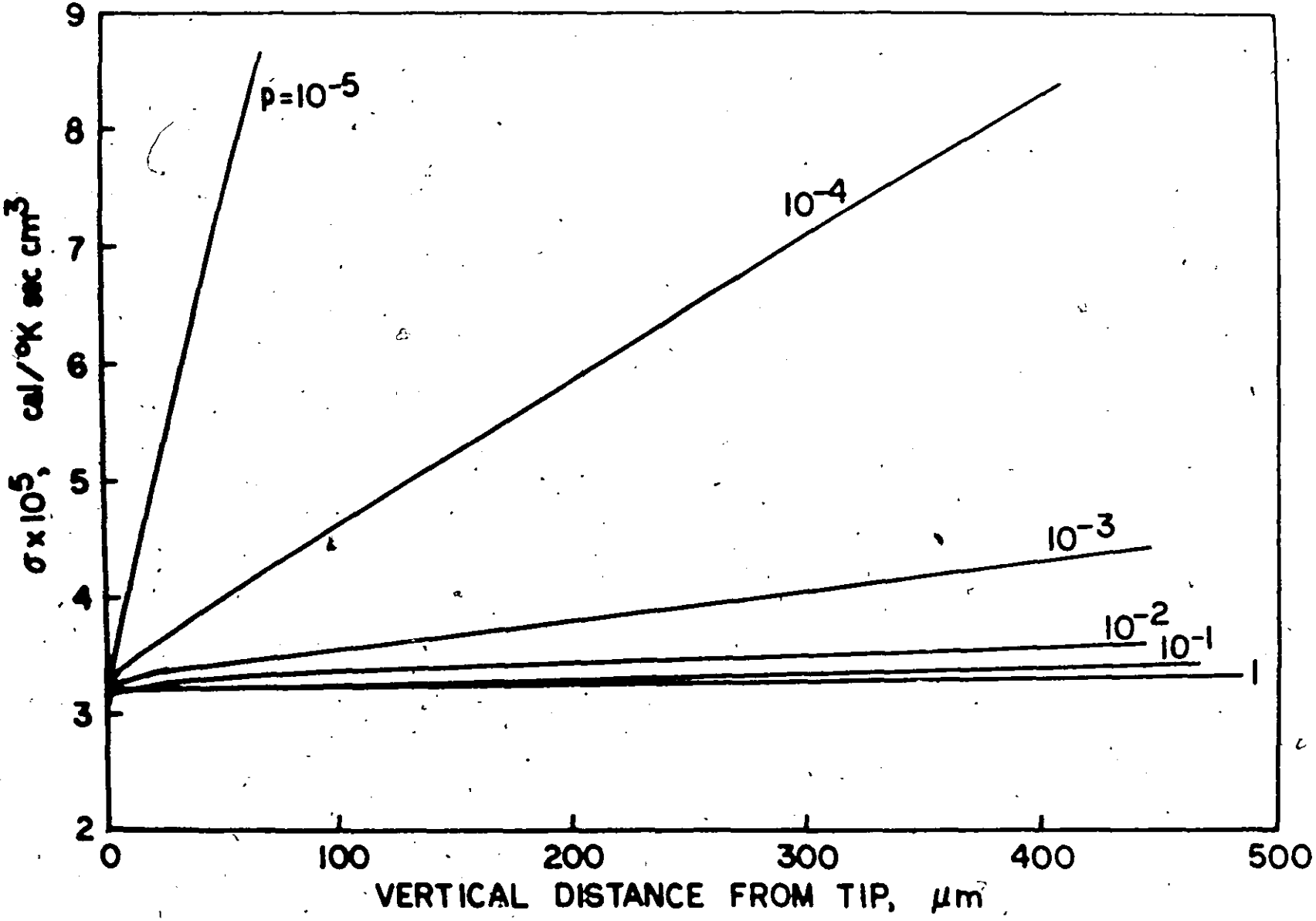

Fig. 9 The rate of internal entropy production, σ, at and behind the tip (low velocity), (Fe-8 wt.% Ni, v = 5:58 mm/hr, G = 31°C/cm).

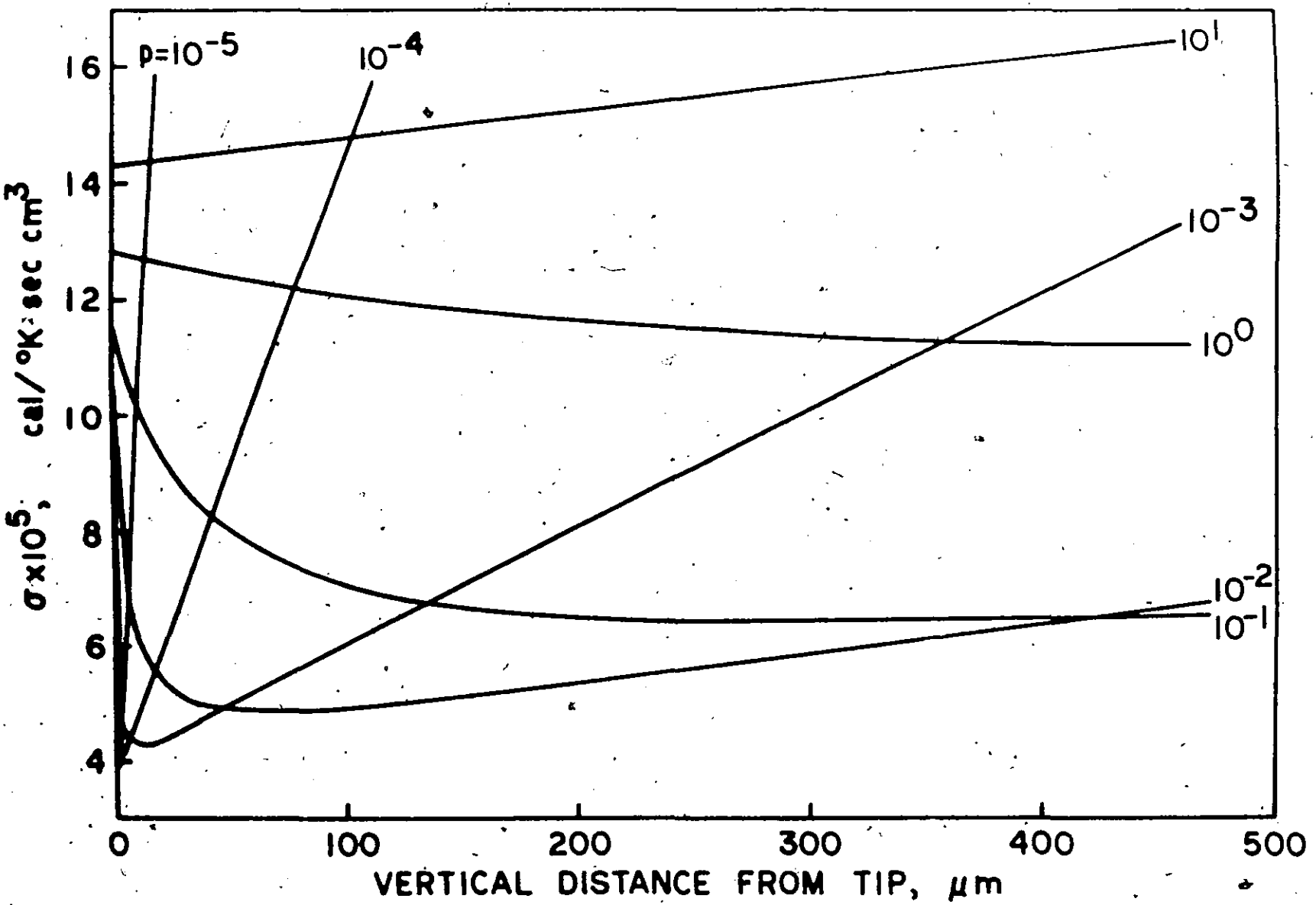

Fig. 10 The rate of internal entropy production, σ, at and behind the tip (higher velocity), (Fe-8 wt.% Ni, v = 44.64 mm/hr, G = 31°C/cm).

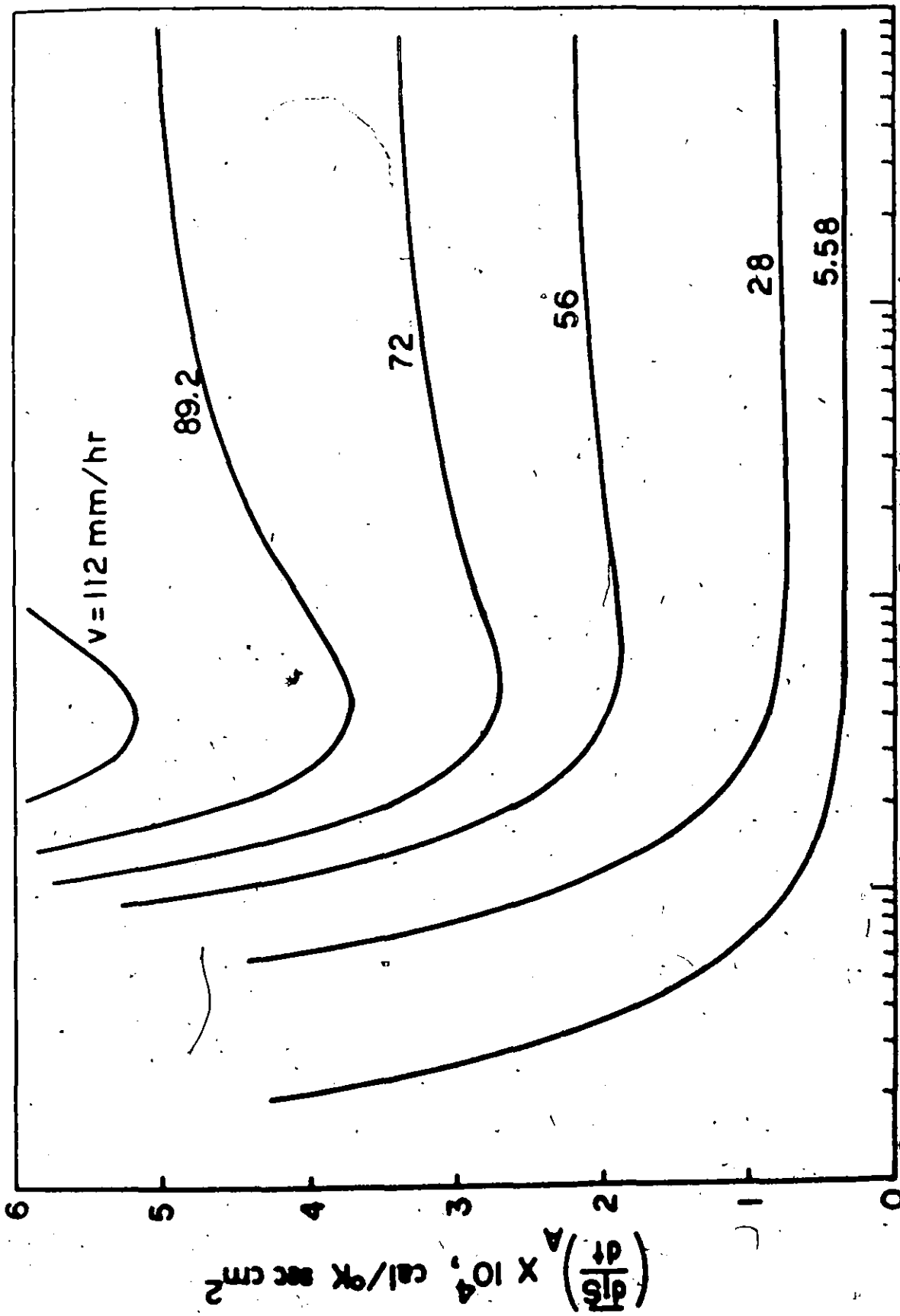

Fig. 11 The variation of $\left(\frac{d_i\bar{S}}{dt}\right)_A$ as a function of p and v (Fe-8 wt.% Ni, G = 31°C/cm).

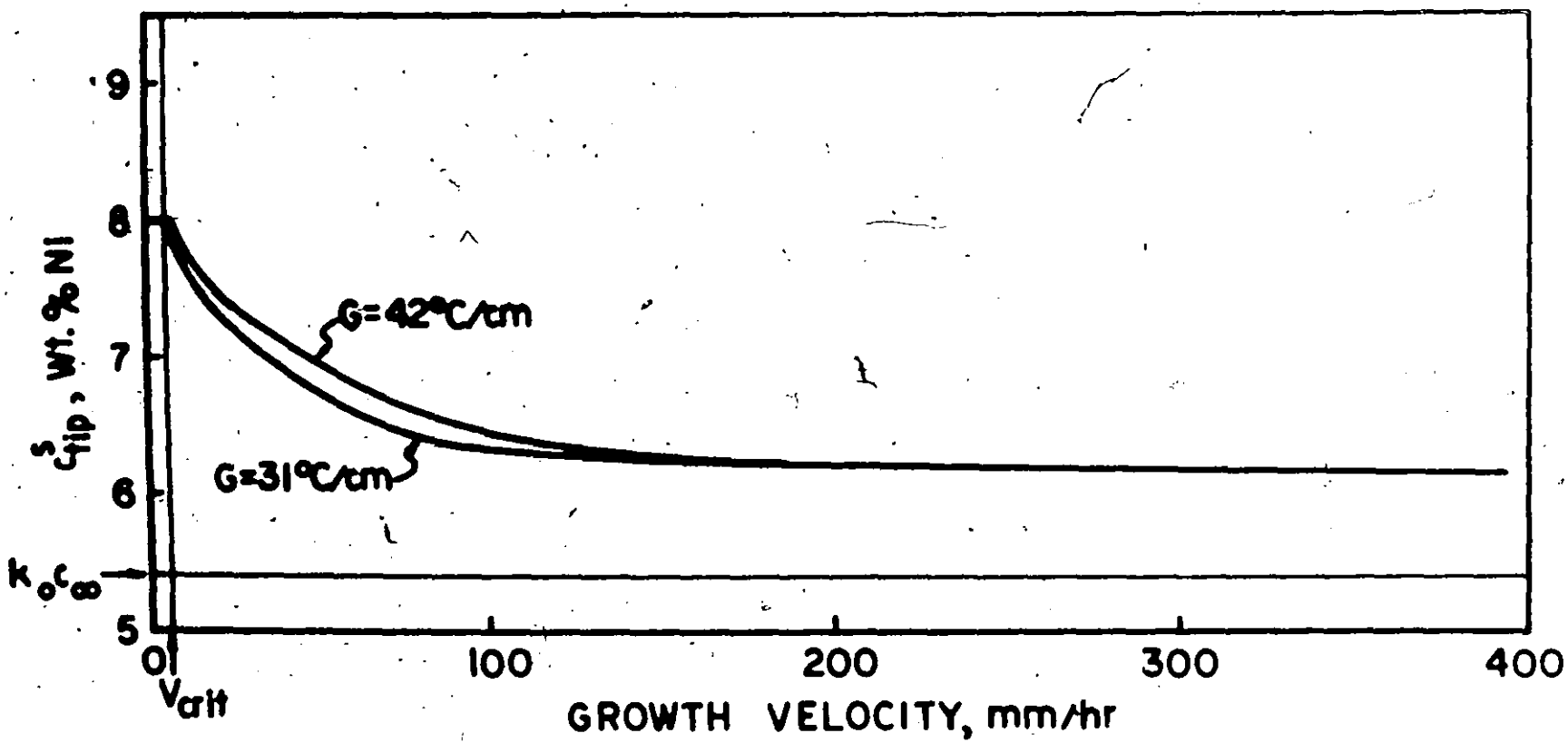

Fig. 12 Calculated tip concentration, c^s_{tip}, as a function of v and G (Fe-8 wt.% Ni).

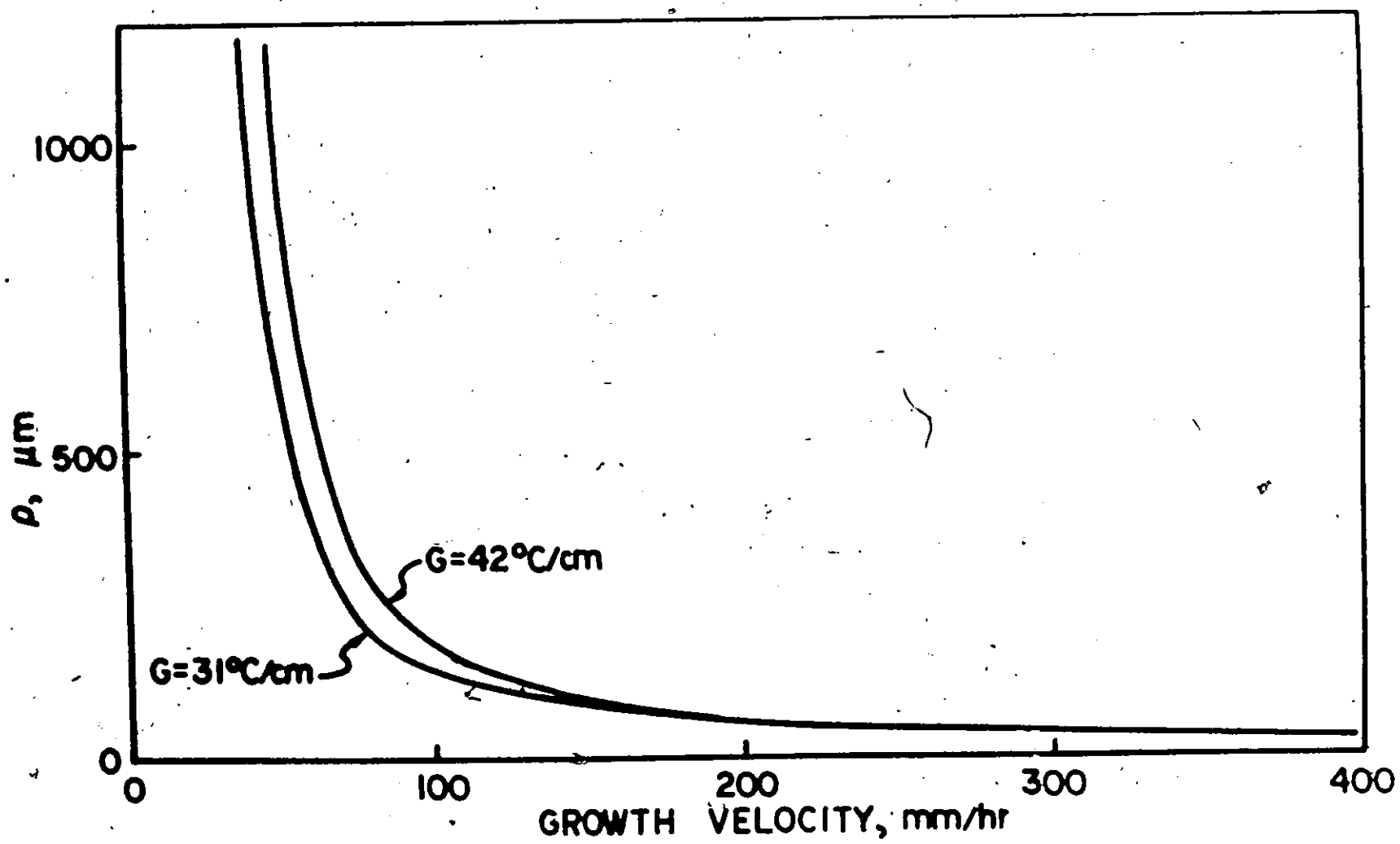

Fig. 13 Calculated radius of tip curvature, ρ, as a function of v and G (Fe-8 wt.% Ni).

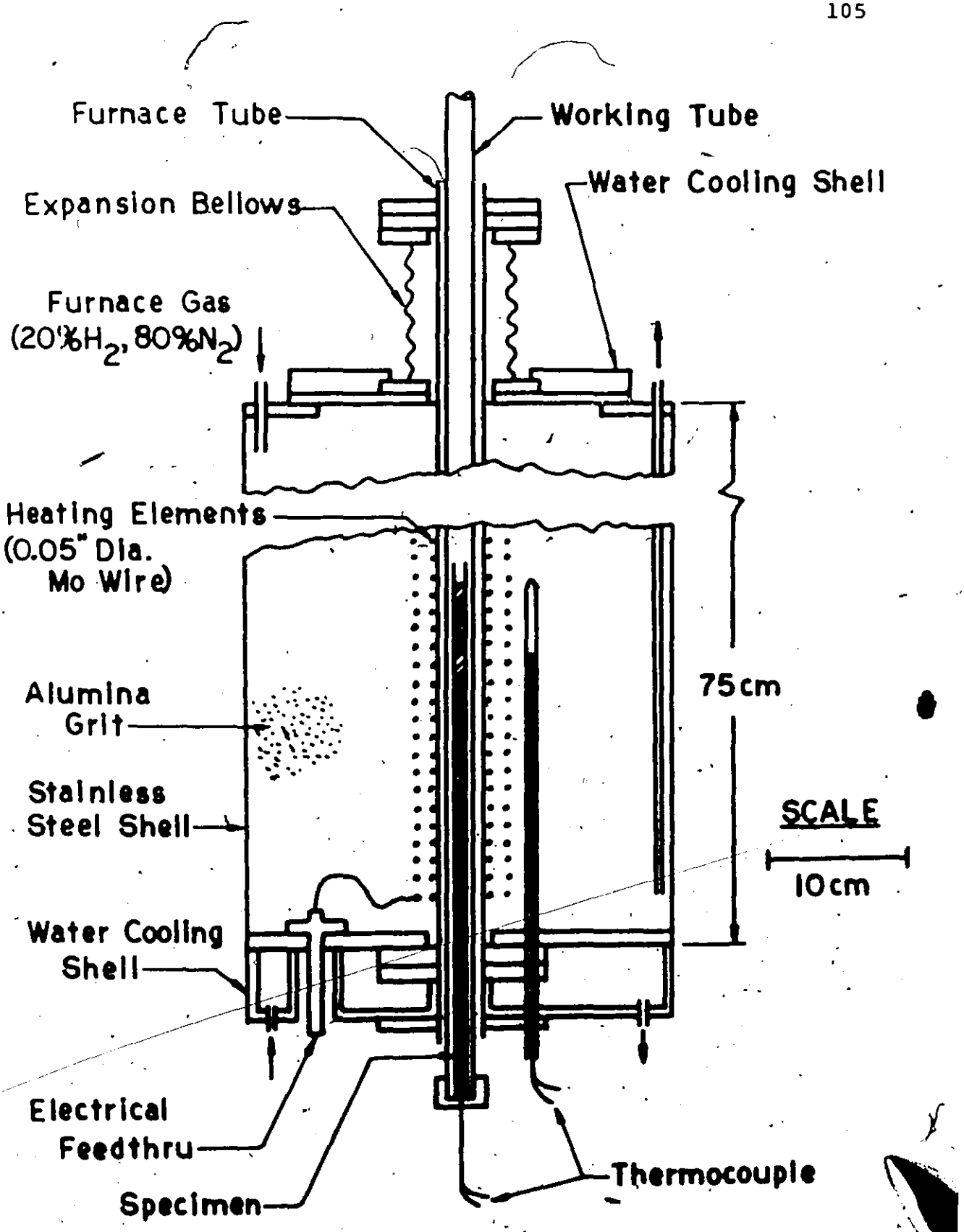

Fig. 14 Sectional view of the furnace.

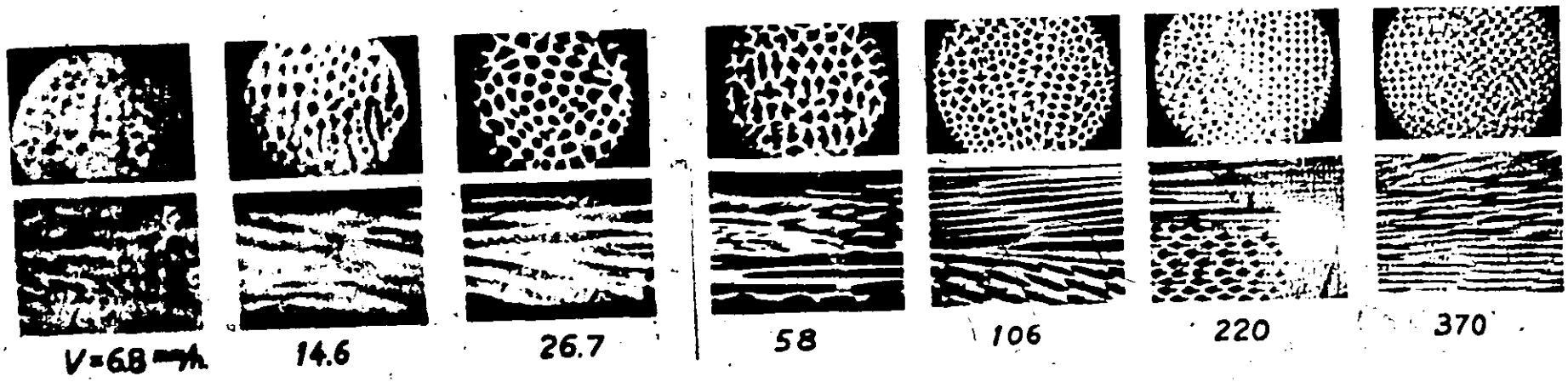

Fig. 15 Variation of solidification structures of Fe-8 wt.% Ni alloy as a function of growth velocity with a constant G($31^{\circ}C/cm$), x 22, reduced 74% for reproduction.

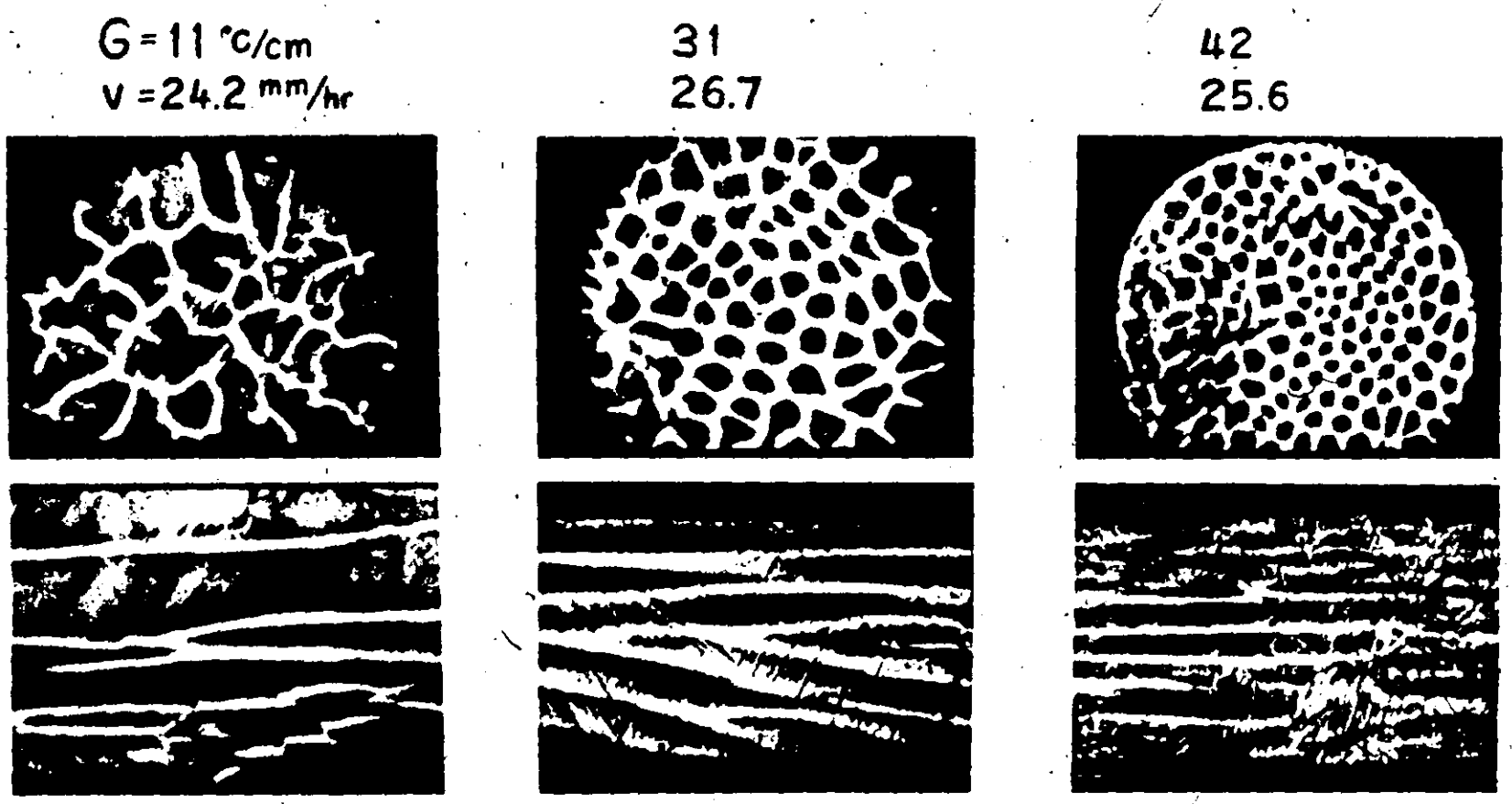

Fig. 16 Variation of solidification structure of Fe-8 wt.% Ni alloy as a function of temperature gradient for approximately the same v, x 22, reduced 47% for reproduction.

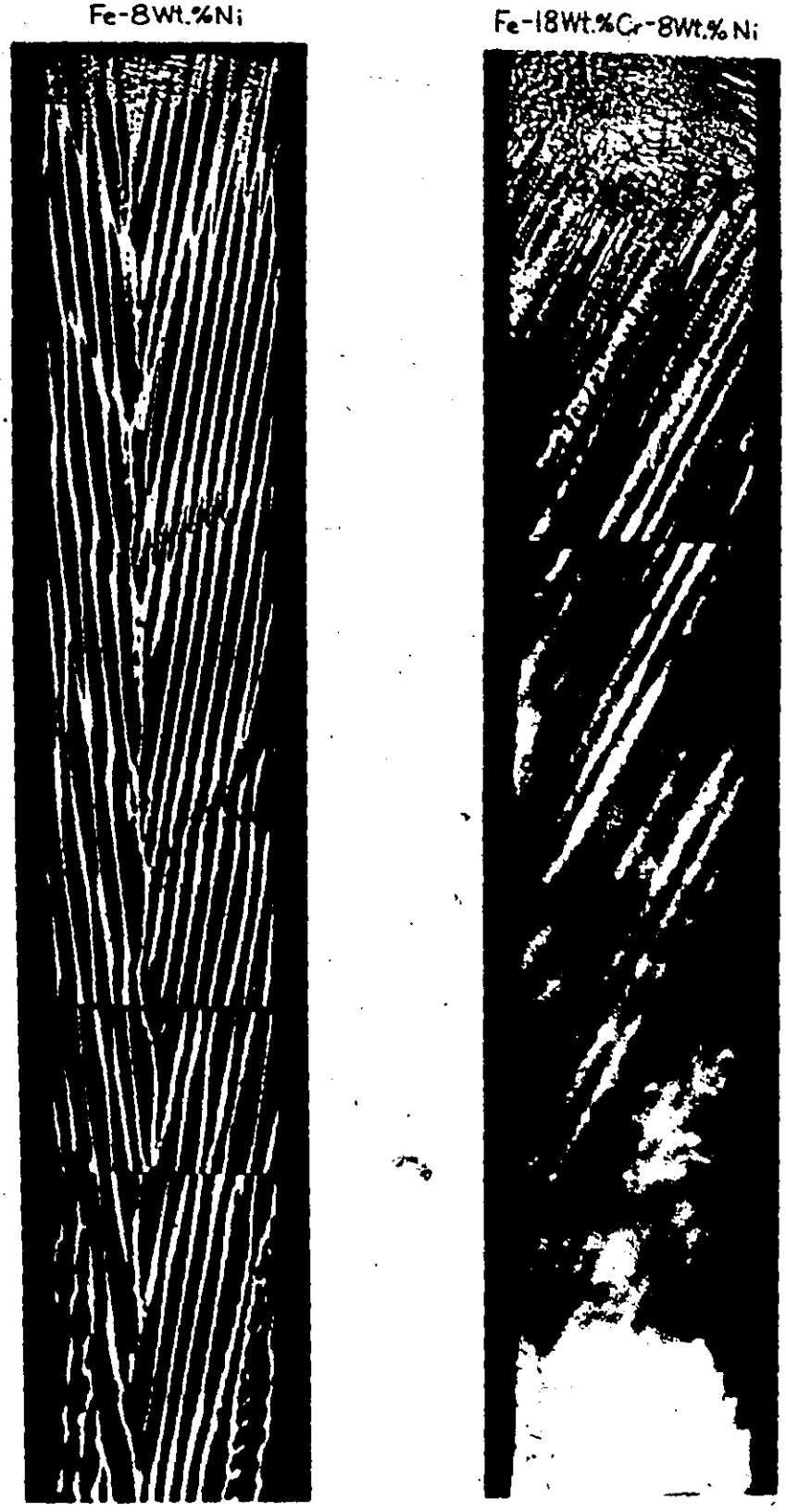

Fig. 17 Longitudinal sections of directionally solidified Fe-8 wt.% Ni (G = 31°C/cm, v = 107.5 mm/hr) and Fe-18 wt.% Cr-8 wt.% Ni (G = 31°C/cm, v = 106 mm/hr) alloys, x 22, reduced 61% for reproduction.

Fe-18Wt.%Cr-8Wt.%Ni-0.35Wt.%C

Fig. 18 Longitudinal section of a directionally solidified Fe-18 wt.% Cr-8 wt.% Ni-0.35 wt.% C alloy specimen (G = 31°C/cm, v = 105 mm/hr), x 22, reduced 63% for reproduction.

Etching Reagents \ Samples	(a) Segregation Intensity: 0.4 wt.% Ni	(b) 0.9 wt.% Ni	(c) 2.6 wt.% Ni
(1) Saturated Solution with H_2S Gas			
(2) Oberhoffer's Reagent			
(3) Improved Reagent	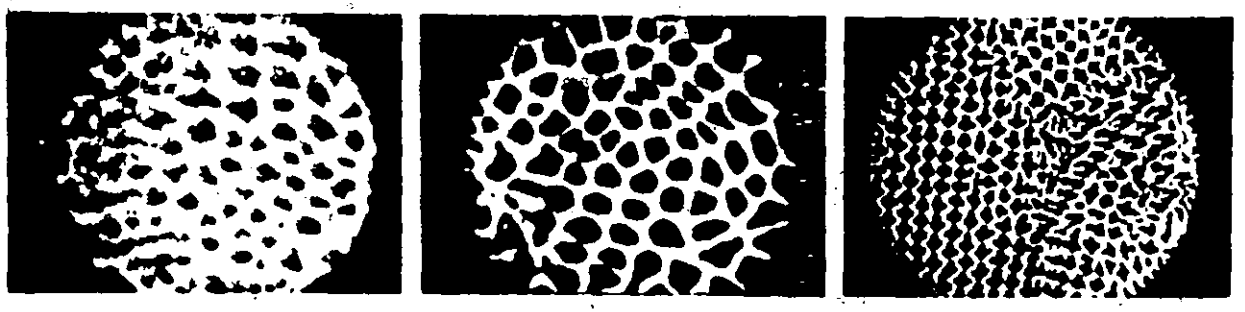		

Fig. 19. Effectiveness of the improved etching reagent for Fe-Ni alloys, x 22, reduced 56% for reproduction.

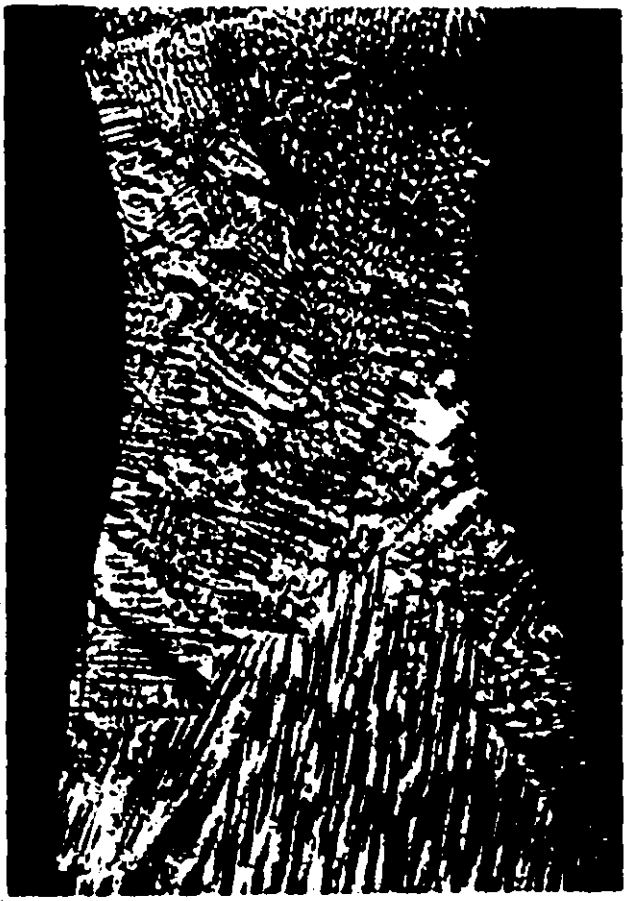

Fig. 20 Effectiveness of the improved etching reagent for Fe-18 wt.% Cr-8 wt.% Ni alloy. Micro-segregation of a quenched floating zone, x 22

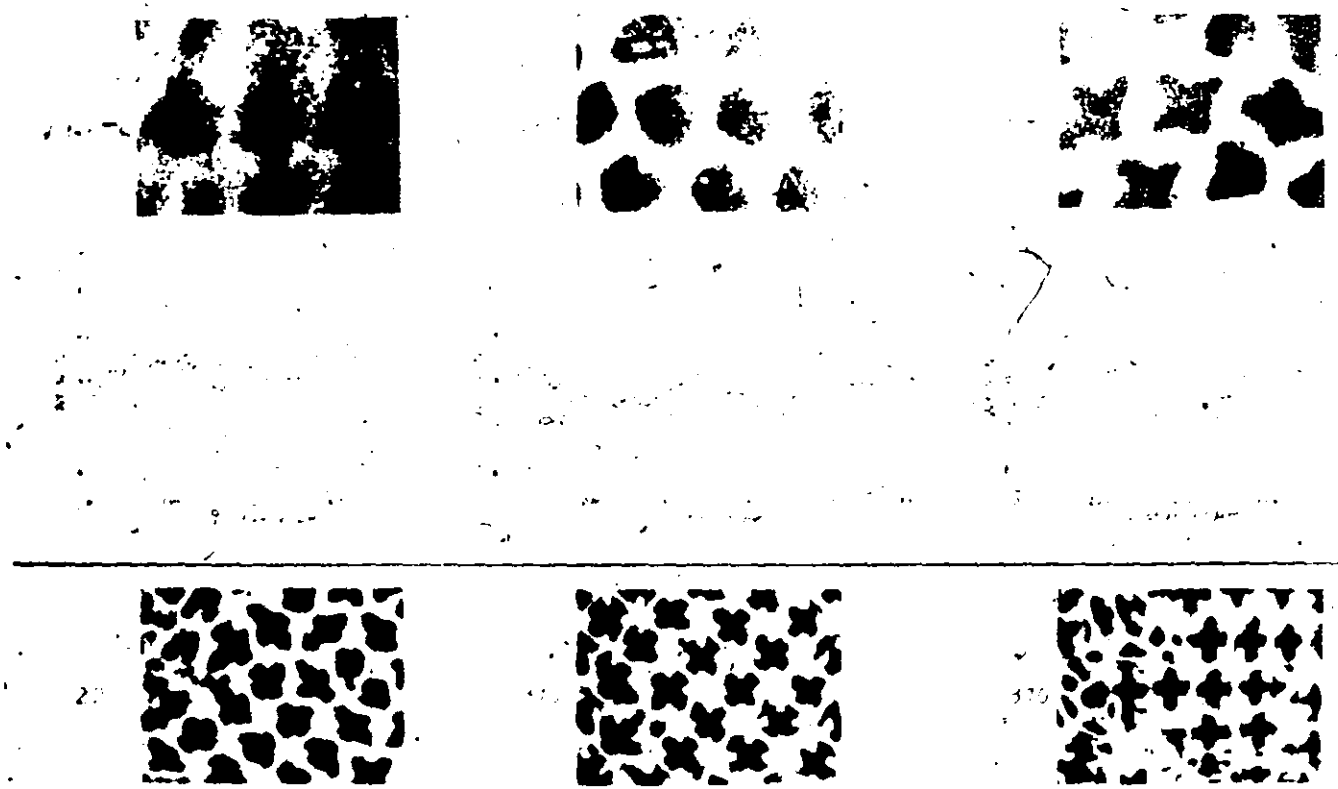

Fig. 21 Electron probe microanalysis of directionally solidified Fe-8 wt.% Ni specimens; the variation of segregation profile as a function of v with a constant G(31°C/cm).

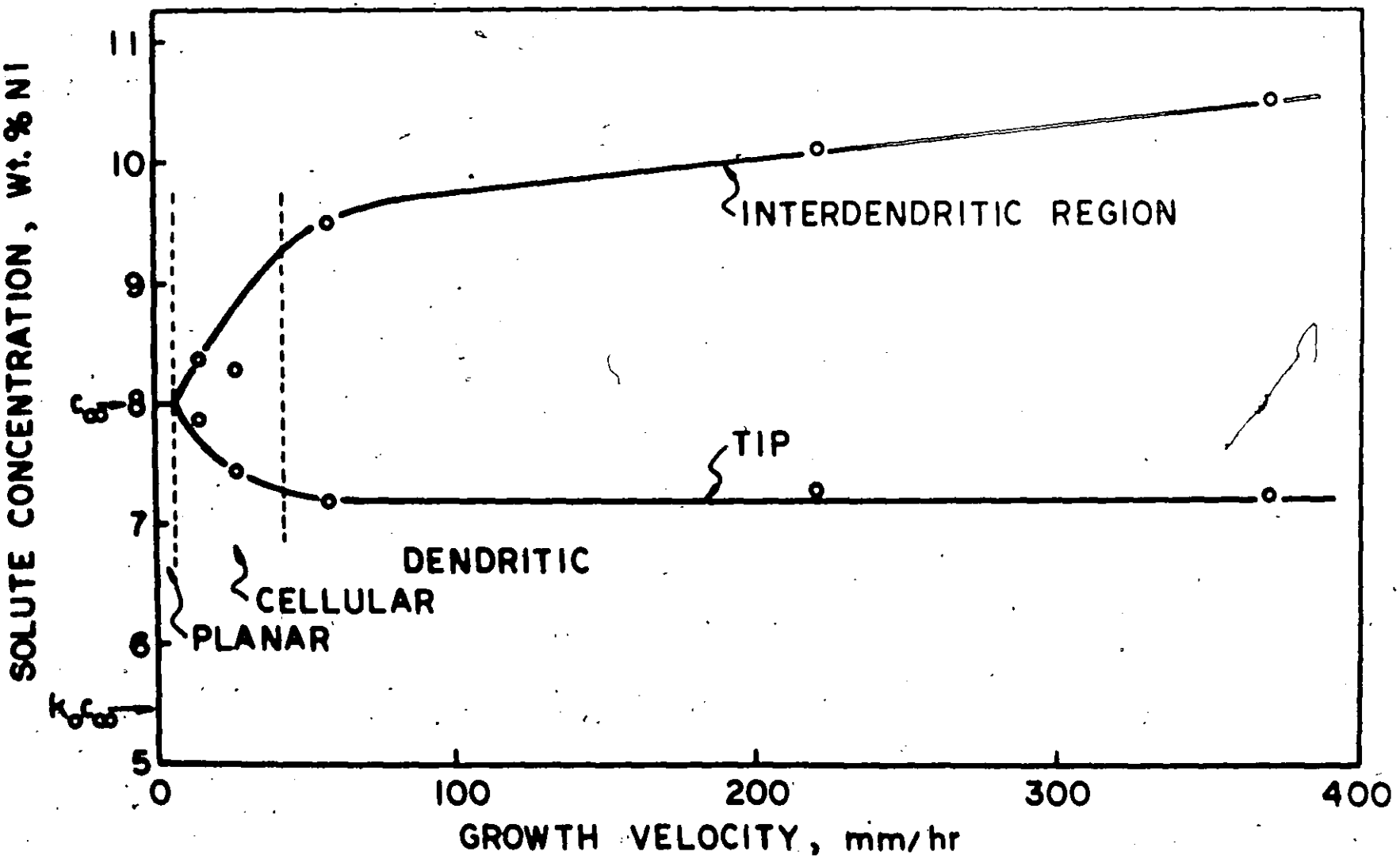

Fig. 22 Experimentally determined solute concentration of the tip and interdendritic region as a function of v with a constant G (Fe-8 wt.% Ni, G = 31°C/cm).

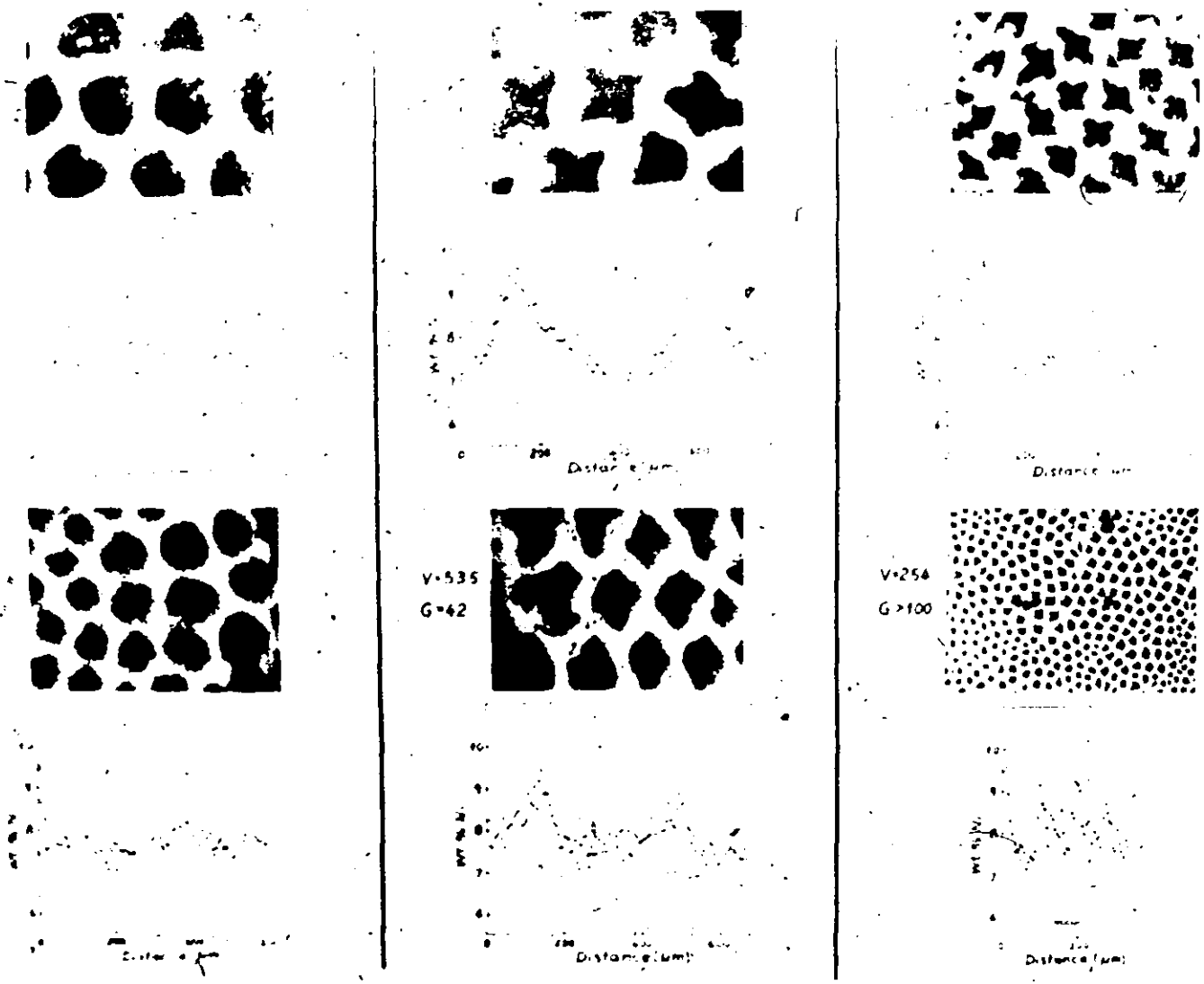

Fig. 23 Electron probe microanalysis of the segregation profile of directionally solidified Fe-8 wt.% Ni specimens (The effect of temperature gradient is demonstrated).

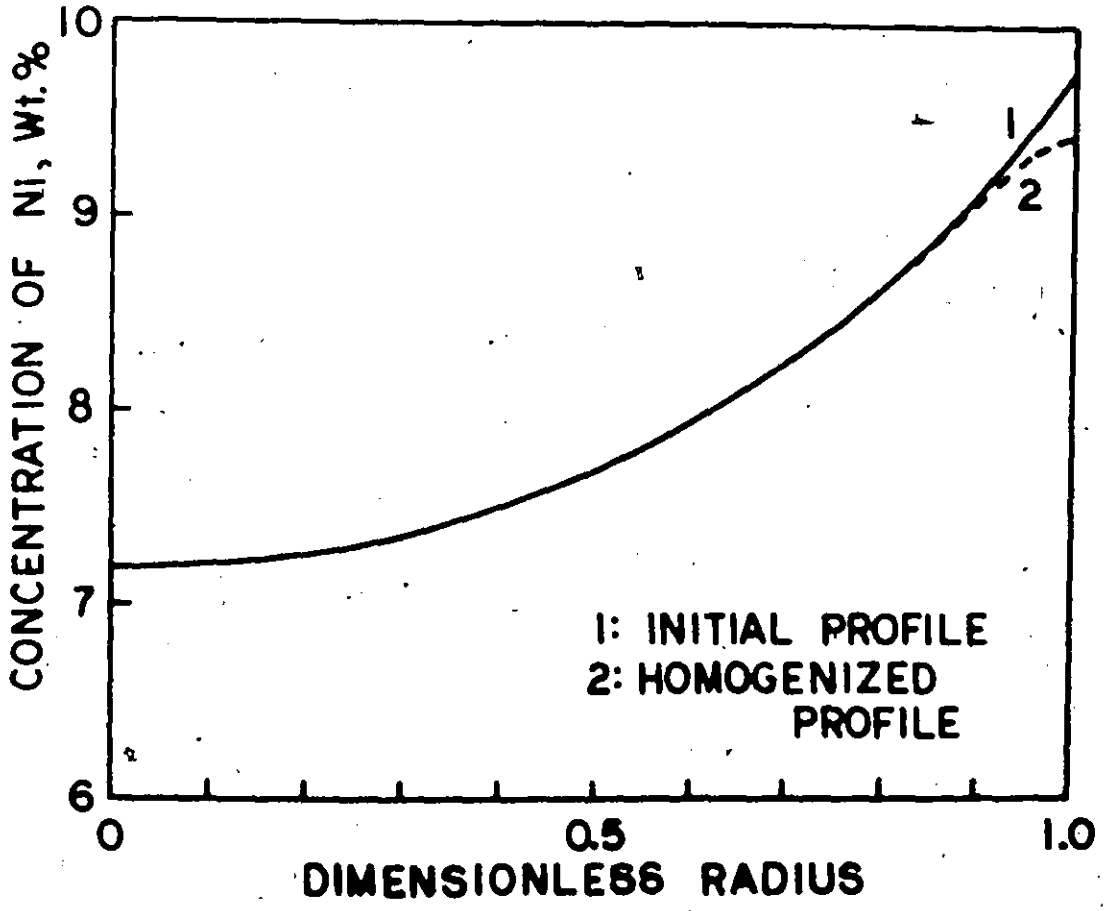

Fig. 24 Homogenization of cylindrical segregation during 8 mm travel after solidification (Fe-8 wt.% Ni, G = 31°C/cm, v = 370 mm/hr).

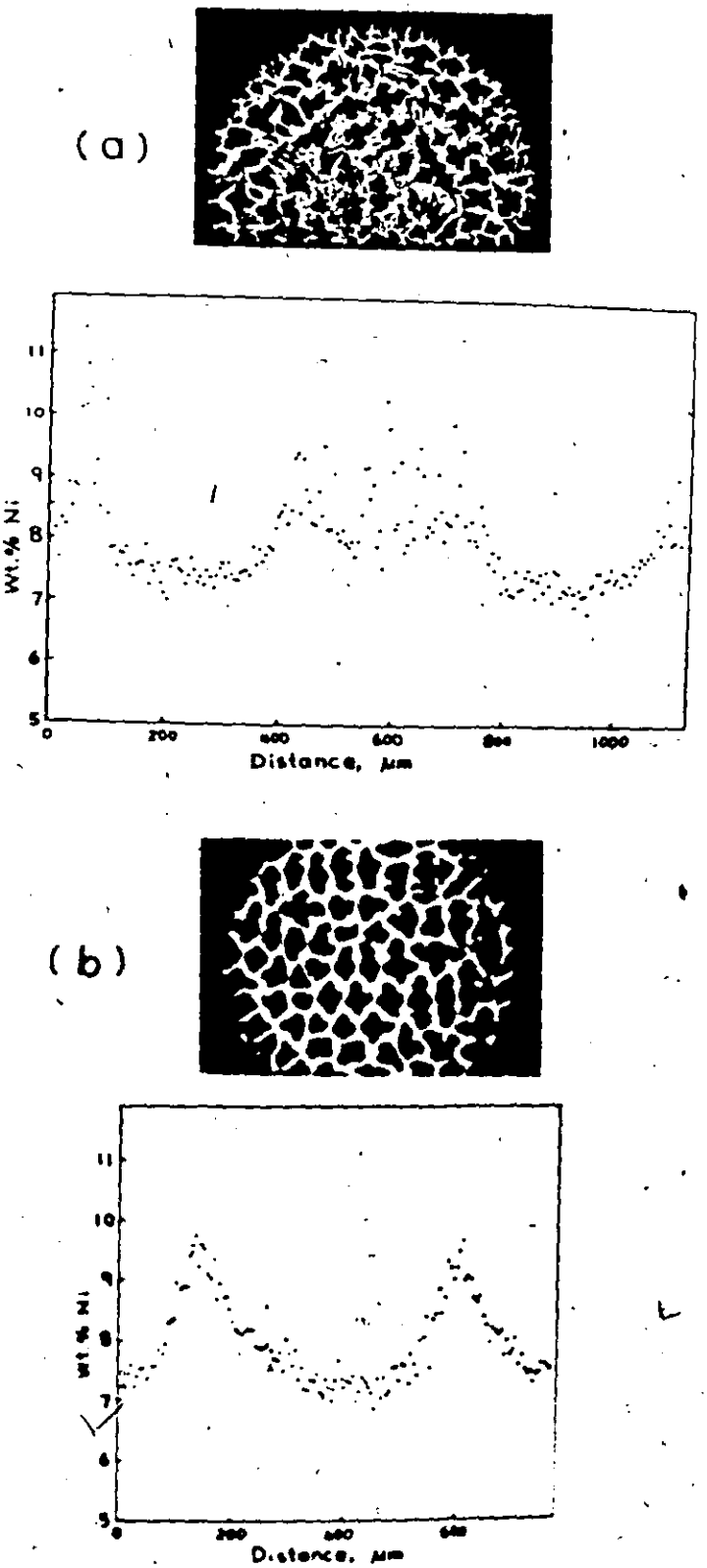

Fig. 25 Electron probe microanalysis of two transverse sections (Fe-8 wt.% Ni, G = 31°C/cm), (a) 0.3 mm below tip (v = 51 mm/hr), finer dendritic structure shows quenched liquid, (b) 8 mm below tip (v = 58 mm/hr).

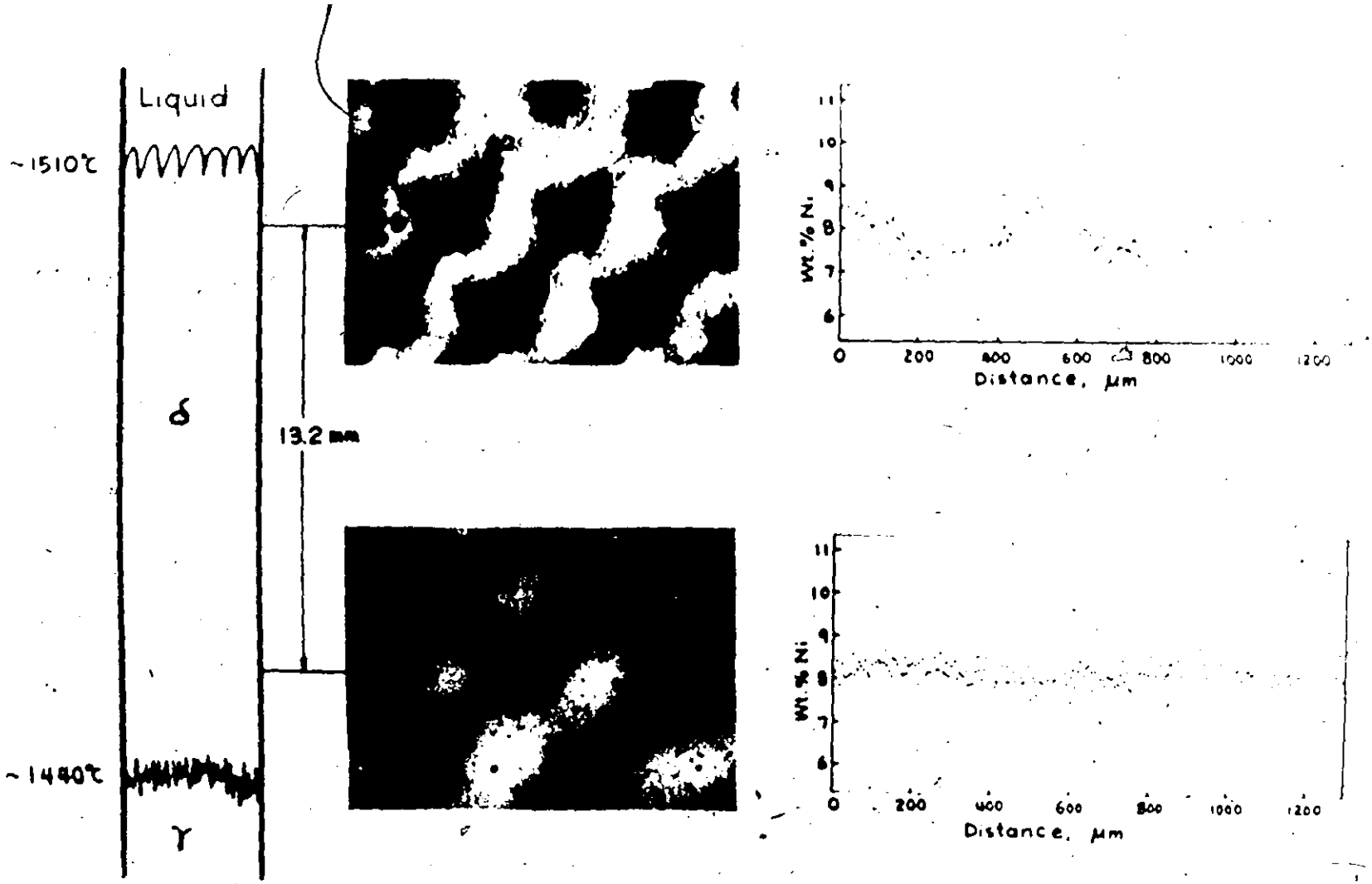

Fig. 26 Quantitative study of homogenization kinetics of the microsegregation of an Fe-18 wt.% Cr-8 wt.% Ni alloy specimen in δ-phase (G = 31°C/cm, v = 55 mm/hr).

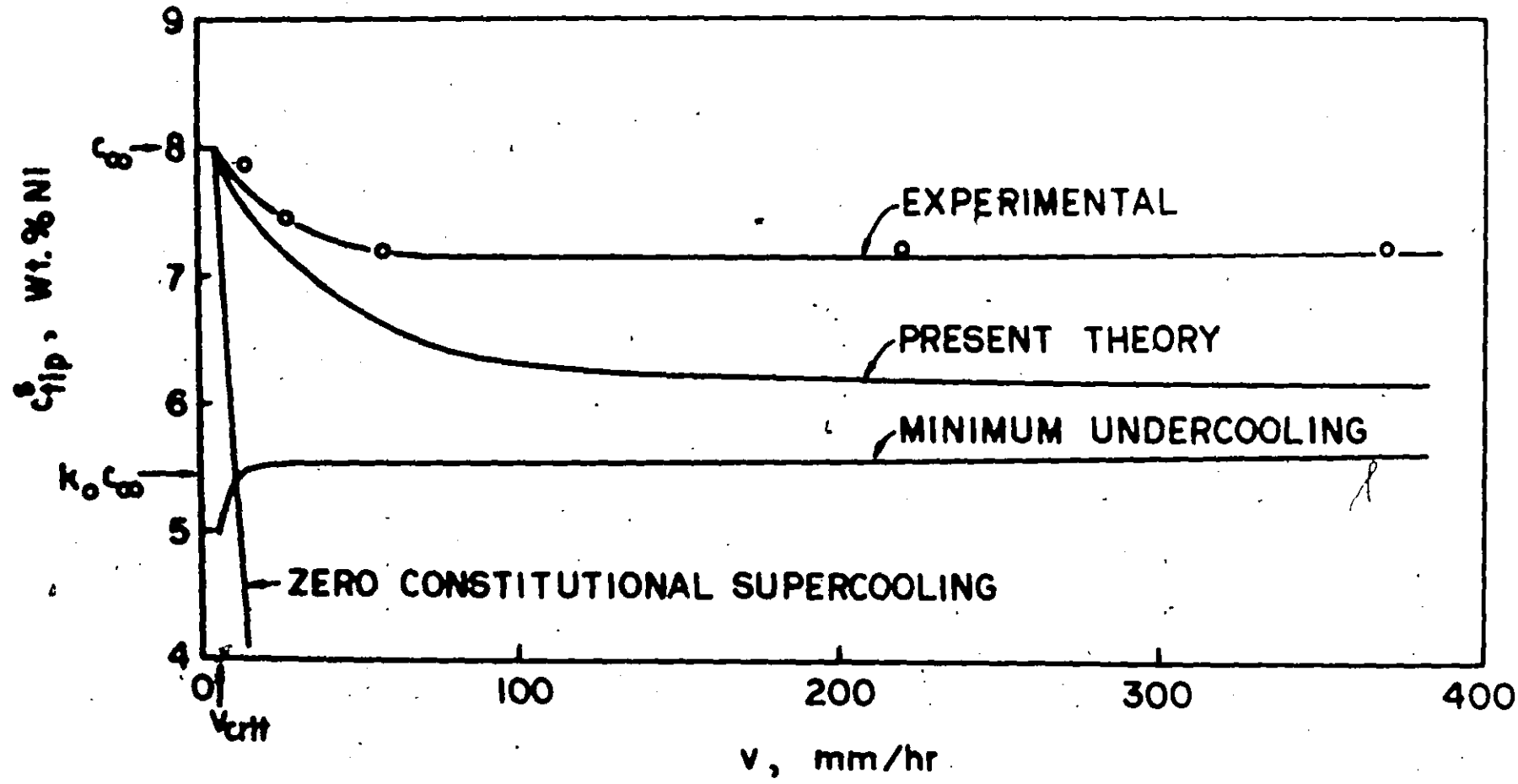

Fig. 27 Comparison of experimentally determined tip concentration with various theoretically predicted values (Fe-8 wt.% Ni, G = 31°C/cm).

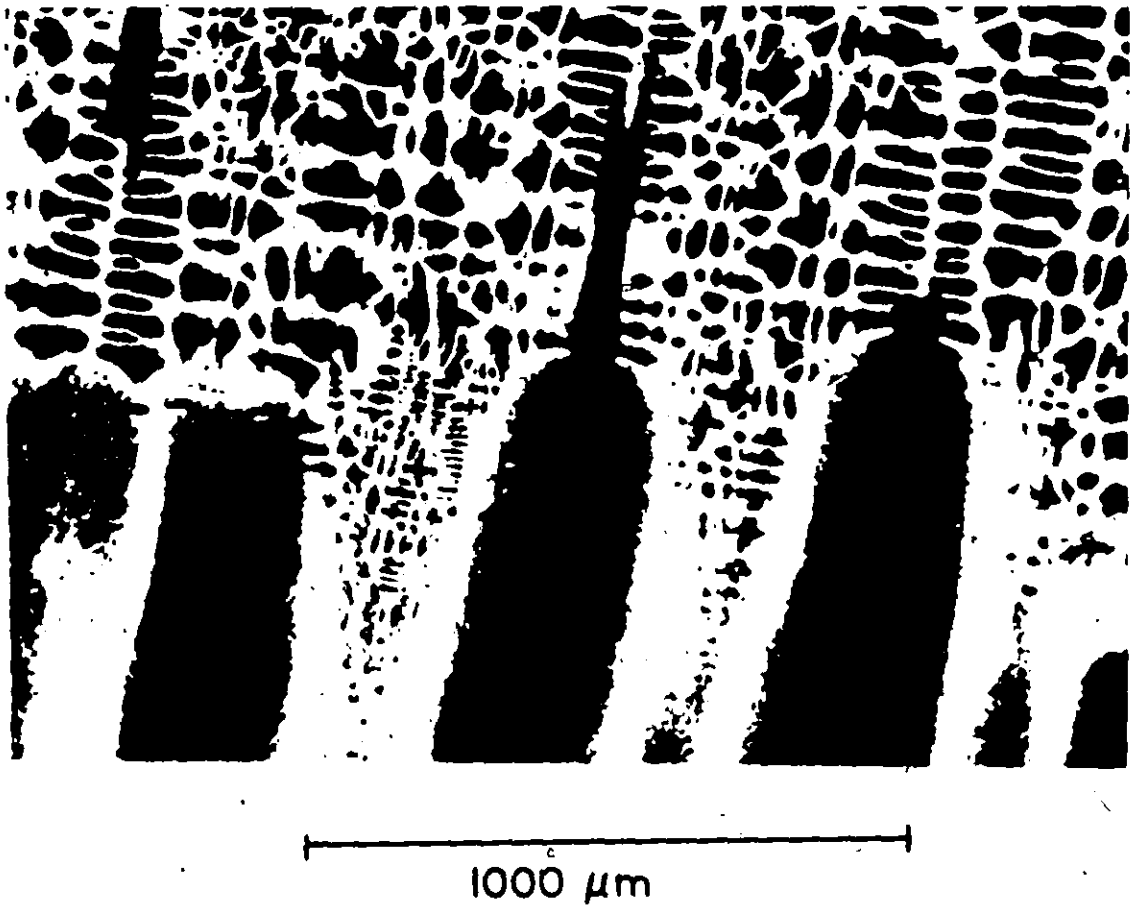

Fig. 28 Quenched growth front during steady state solidification (Fe-8 wt.% Ni, G = 31°C/cm, v = 51 mm/hr), x 80.

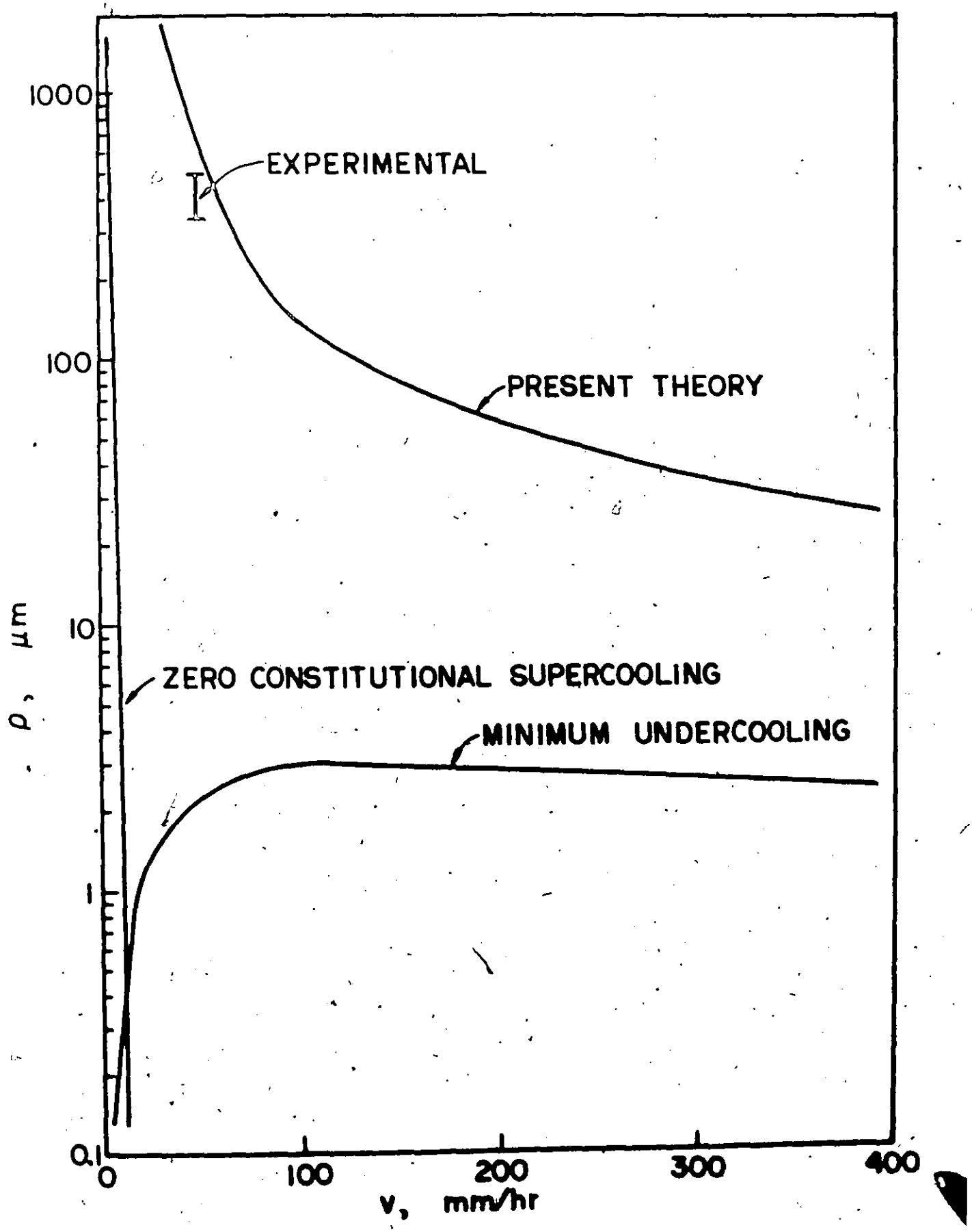

Fig. 29 Comparison of an experimentally observed tip radius with various predicted values (Fe-8 wt.% Ni, G = 31°C/cm).

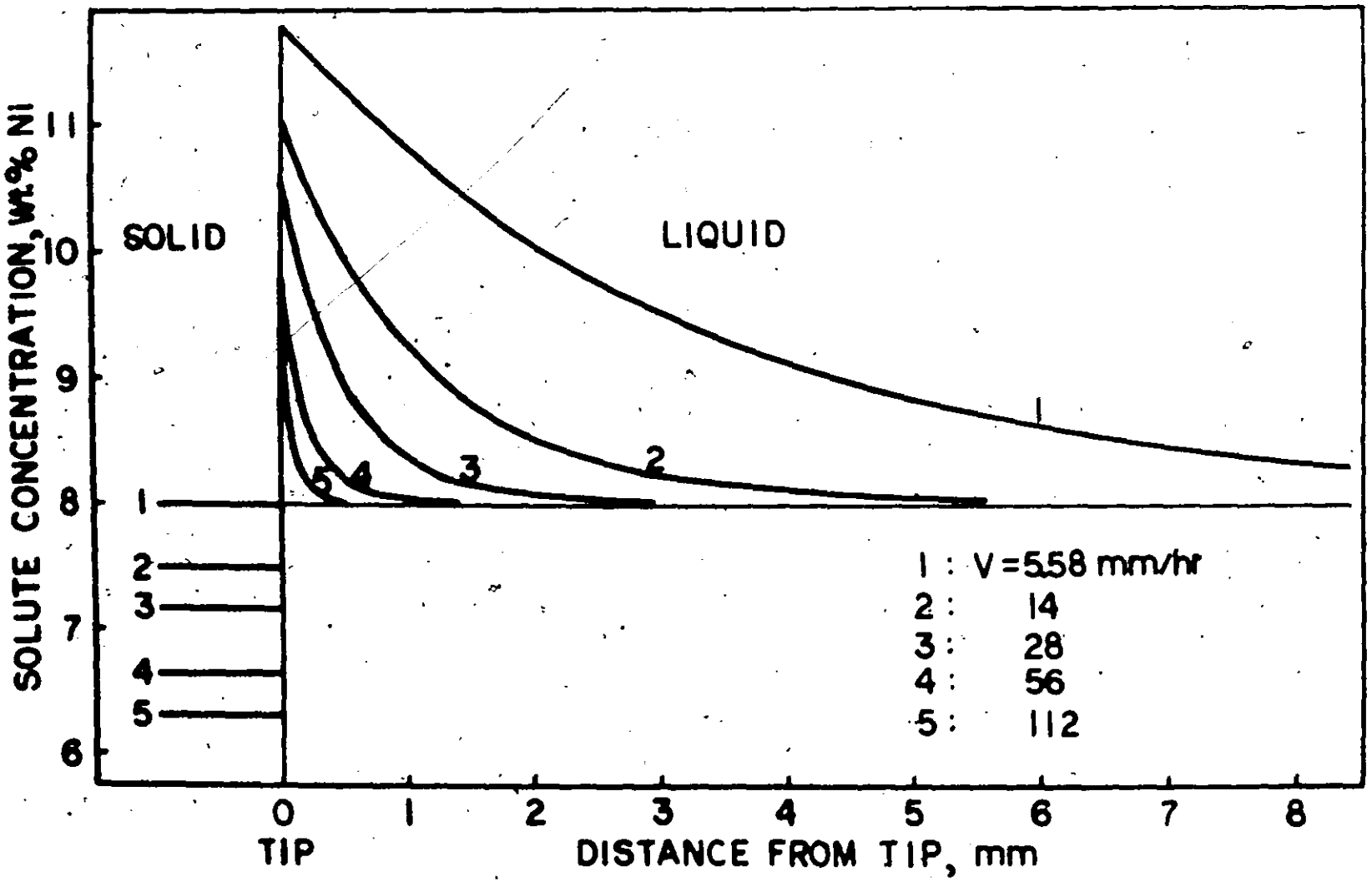

Fig. 30 Solute diffusion profiles ahead of growing dendrite tips as a function of v (Fe-8 wt.% Ni, G = 31°C/cm).

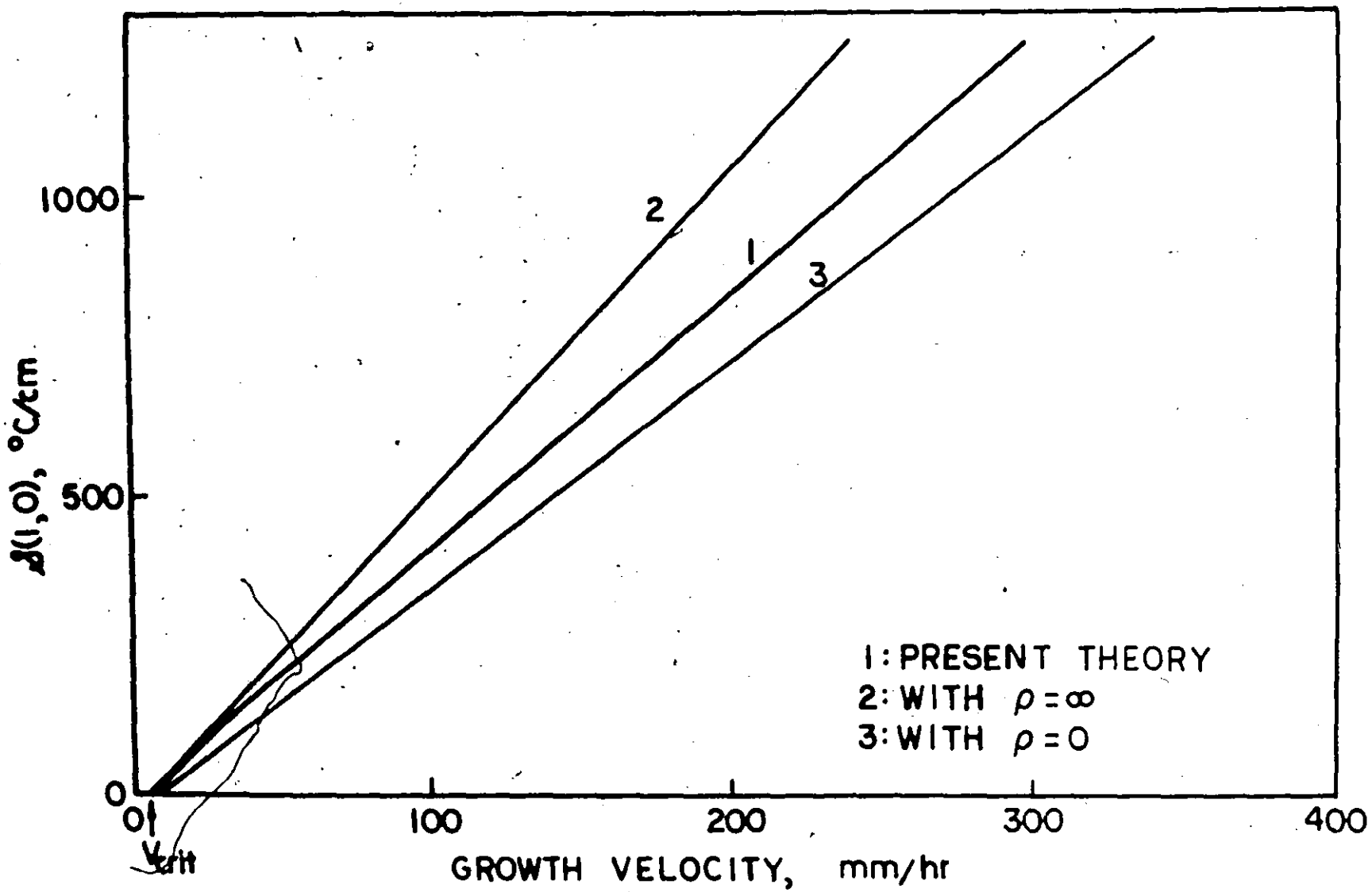

Fig. 31 Constitutional supercooling at the tip, $\Delta(1,0)$, as a function of growth velocity (Fe-8 wt.% Ni, G = 31°C/cm, Gibbs-Thomson and kinetic effects are neglected).

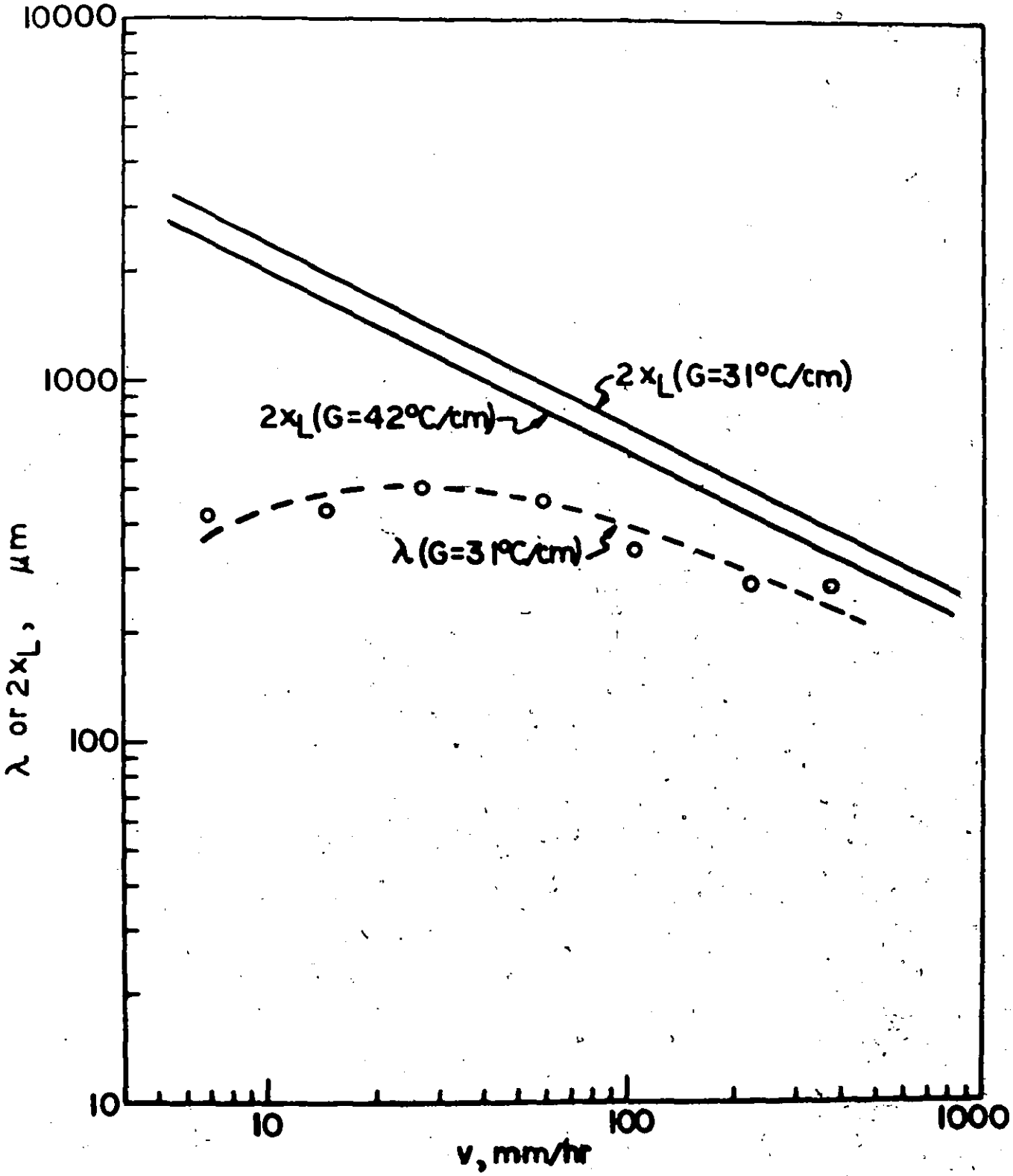

Fig. 32 Comparison of true spacing, λ, with the virtual spacing, $2x_L$, of hypothetical paraboloidal dendrites (Fe-8 wt.% Ni).